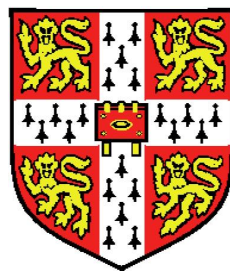


Alloy Design for a Fusion Power Plant



Richard Kemp

Gonville and Caius College

University of Cambridge

A thesis submitted for the degree of

Doctor of Philosophy

May 2006

Preface

This dissertation is submitted for the degree of Doctor of Philosophy at the University of Cambridge. The research described herein was conducted under the supervision of Professor H. K. D. H. Bhadeshia in the Department of Materials Science and Metallurgy, University of Cambridge, between October 2002 and April 2006.

Except where acknowledgement and reference are made to previous work, the work is, to the best of my knowledge, original. This dissertation is the result of my own work and includes nothing which is the outcome of work done in collaboration except where specifically indicated in the text.

Neither this, nor any substantially similar dissertation, has been or is being submitted for any other degree, diploma, or other qualification at any other university. This dissertation does not exceed 60,000 words in length.

Some of the work described herein has been published in the *Journal of Nuclear Materials*, or has been submitted for publication in the proceedings of the 12th International Conference on Fusion Reactor Materials and *Energy Materials*.

Richard Kemp

August 8, 2006

Acknowledgements

I would like to thank Harry Bhadeshia for his supervision and enthusiasm and also all the members of the PT group for encouragement, coffee and assistance with occasional computer problems. This thesis would also have been impossible without the help, support, and inspiration of Geoff Cottrell and his colleagues at Culham Science Centre.

I would also like to express my gratitude to EURATOM/UKAEA and the EPSRC for their financial support, and to the Ironmongers' Company for their generous bursary enabling me to study for a month at UCSB, making contacts and friends.

I am indebted to Bob Odette and Takuya Yamamoto for their provision of data, and work organising ICFRM-12. A further thanks must go to the other members of their group for their warm welcome in Santa Barbara.

Finally, I would like to thank my parents, friends, and long-suffering girlfriend for all their support over the last three years.

“I have said it thrice:

What I tell you three times is true.”

Lewis Carroll, *The Hunting Of The Snark*

Abstract

Fusion power is generated when hot deuterium and tritium nuclei react, producing alpha particles and 14 MeV neutrons. These neutrons escape the reaction plasma and are absorbed by the surrounding material structure of the plant, transferring the heat of the reaction to an external cooling circuit. In such high-energy neutron irradiation environments, extensive atomic displacement damage and transmutation production of helium affect the mechanical properties of materials.

Among these effects are irradiation hardening, embrittlement, and macroscopic swelling due to the formation of voids within the material. To aid understanding of these effects, Bayesian neural networks were used to model irradiation hardening and embrittlement of a set of candidate alloys, reduced-activation ferritic-martensitic steels. The models have been compared to other methods, and it is demonstrated that a neural network approach to modelling the properties of irradiated steels provides a useful tool in the future engineering of fusion materials, and for the first time, predictions are made on irradiated property changes based on the full range of available experimental parameters rather than a simplified model. In addition, the models are used to calculate optimised compositions for potential fusion alloys. Recommendations on the most fruitful ways of designing future experiments have also been made.

In addition, a classical nucleation theory approach was taken to modelling the incubation and nucleation of irradiation-induced voids in these steels, with a view to minimising this undesirable phenomenon in candidate materials.

Using these models, recommendations are made with regards to the engineering of future reduced-activation steels for fusion applications, and further research opportunities presented by the work are reviewed.

Contents

Abstract	iv
Abbreviations	ix
Nomenclature	x
1 Introduction	1
2 First-wall materials in fusion power plants	3
2.1 Introduction	3
2.2 The first-wall environment	4
2.2.1 Activation of irradiated materials	6
2.2.2 Displacement damage	8
2.3 Candidate first-wall structural materials	10
2.3.1 Vanadium alloys	11
2.3.2 Ferritic/martensitic steels	12
2.3.3 Oxide dispersion strengthened alloys	13
2.3.4 SiC _f /SiC composites	13
2.4 The International Fusion Materials Irradiation Facility	14
3 Modelling complex properties	16
3.1 Artificial neural networks	17
3.1.1 Two approaches to probability	17
3.1.2 Bayesian neural networks	18
3.2 Dimensionality of the data	24

4	Neural network modelling of irradiated steels	29
4.1	Intelligent design of a neural network model	29
4.2	Optimisation and genetic algorithms	31
5	Irradiation hardening	35
5.1	Hardening mechanisms	35
5.2	Previous models	38
5.3	Neural network model of irradiation hardening	38
5.3.1	Yield stress database	39
5.3.2	Model training	44
5.3.3	Model predictions	47
5.3.3.1	Predictions for existing steels	47
5.3.3.2	Conclusions	53
5.3.4	Optimisation of steel composition	55
5.3.4.1	Predictions for optimised steel	57
5.4	The need for more data	58
6	Irradiation embrittlement	59
6.1	Mechanisms of irradiation embrittlement	60
6.2	Previous models	62
6.3	Neural network models of Charpy fracture properties	63
6.3.1	Fracture database	63
6.3.2	Model training	69
6.3.2.1	Δ DBTT model	69
6.3.2.2	Δ USE model	69
6.3.3	Model predictions	71
6.3.3.1	Predictions for existing steels	71
6.3.4	Optimisation of steel composition	85
6.3.4.1	Predictions for optimised steel	86
6.3.5	The need for more data	87

7	Void nucleation in irradiated materials	89
7.1	The origin of cavities	89
7.2	Description of dissolved helium	91
7.2.1	The quasi-chemical model	91
7.2.1.1	Gas potential in a void	91
7.2.1.2	Gas potential in solution	92
7.2.1.3	Steady-state helium concentration under irradiation	94
7.2.2	Discussion	94
7.3	Void nucleation model	96
7.3.1	Properties of the void nucleation model	99
7.3.2	High pressure gas law models	102
7.4	Creating swelling-resistant steels	102
8	Designing optimised experiments for IFMIF	104
8.1	Introduction	104
8.2	Model predictions at low dose	105
8.3	Model predictions for the fusion regime	108
8.4	Summary and conclusions	108
9	Summary	111
9.1	Neural network models and radiation damage	111
9.2	Optimisation of steel compositions	112
9.3	Alloy design for a fusion power plant	112
9.4	Database issues	113
9.5	Further work	113
A	Probability of a coin toss	115
B	Sammon mapping code for <i>Mathematica</i>	117
C	Yield stress model database references	122
References		128

Abbreviations

Term	Meaning
ANN	Artificial neural network
appm	Atomic parts per million
BCC	Body centred cubic
CW	Cold work
DBTT	Ductile to brittle transition temperature
DEMO	Demonstration fusion power plant design
dpa	Atomic displacements per atom
EASY	European Activation System
FCC	Face-centred cubic
FE	Finite-element
FIM	Field ion microscope
GA	Genetic algorithm
IFMIF	International Fusion Materials Irradiation Facility
ITER	International Thermonuclear Experimental Reactor
LPE	Log predictive error
MC	Master curve
MD	Molecular dynamics
ODS	Oxide dispersion strengthened [steel]
PFM	Plasma facing material
RAFM	Reduced activation ferritic/martensitic [steel]
SIA	Self interstitial atom
SiC_f/SiC	Silicon carbide fibre/silicon carbide [composite]
SS	Stainless steel
USE	Upper shelf energy
wppm	Weight parts per million

Nomenclature

Term Meaning

Chapter 2

D	Deuterium
T	Tritium
α	Alpha particle
n	Neutron
C	Total concentration of alloying elements
C_i	Concentration of alloy element i
$C_{i,\max}$	Maximum permitted concentration of i

Chapter 3

$P(x y)$	Probability of x, given y
σ_y	Modelling uncertainty
$\{c_i\}$	Chemical composition
c_{He}	Helium concentration
K	Irradiation damage rate
T_{irr}	Irradiation temperature
T_{test}	Tensile test temperature
t	Radiation time
h_i	Neuron activation function
W_{ij}	Neuron weight
ω_i	Neuron bias term
x_j	Neuron input
y	Neuron output function
$M(w)$	Network training objective function

Term Meaning

E_w	Network training regulariser
E_D	Network training error
$t^{(k)}$	Set of network targets
α	Objective function control parameter
β	Objective function control parameter
ω_w	Network determined significance of input
E	Sammon mapping error
d_{ij}	Distance between points i and j in d -space
d_{ij}^*	Distance between points i and j in L -space

Chapter 4

X_i	Genetic algorithm chromosome
x_{ij}	Genetic algorithm gene of chromosome X_i
F_i	Fitness factor of chromosome X_i
σ_i	Standard deviation error for chromosome X_i
$\sigma_{y,i}^{(l)}$	Modelling uncertainty of committee member l for chromosome X_i
t	Genetic algorithm target value
f_i	Committee prediction for chromosome X_i

Chapter 5

σ_y	Yield stress
$\Delta\sigma_y$	Change in yield stress
α	Fitting parameter
M	Taylor parameter
μ	Shear modulus
b	Burgers vector
N	Number density of obstacles
d	Average diameter of obstacles
K	Radiation damage rate
t	Radiation time

Term	Meaning
T_{irr}	Irradiation temperature
T_{test}	Tensile test temperature
Q	Activation energy for an Arrhenius process
k	Boltzmann's constant

Chapter 6

n	Strain hardening exponent
T_0	Master curve reference temperature
T_{norm}	Normalising temperature
T_{temp}	Tempering temperature
t_{norm}	Normalising time
t_{temp}	Tempering time
C	Degree of cold working
σ_w	ANN perceived significance of input

Chapter 7

(n, α)	Alpha decay of neutron-activated atoms
P	Pressure
γ	Surface energy
r	Cavity radius
k^2	Sink strength
C	Cavity number density
T	Temperature
μ_g	Chemical potential per atom of a gas
μ^0	Chemical potential in standard state
f	Gas fugacity
R	Molar gas constant
$B_{i,n}$	Virial coefficients of a gas
μ_s	Chemical potential per atom of an interstitial solid solution
\bar{E}_u	Partial energy of solute atoms in dilute solution

Term	Meaning
\bar{S}_u^v	Partial excess (non-configurational) entropy of a solution
θ	Atom fraction of solute species
β	Number of interstitial sites per solvent atom
z	Nearest-neighbour coordination number for interstitial sites
ω	Pairwise interaction energy of nearest-neighbour solute atoms
μ^∞	Chemical potential of infinitely dilute interstitial solution
P_e	Equilibrium pressure between a gas and a solid solution of gas atoms
C_{He}^T	Atom fraction of He in non-vacancy traps
C_{He}^V	Atom fraction of He trapped at vacancies
C_{He}	Atom fraction of He in solution
C_{He}^0	Total atom fraction of He in material
b	radiation re-solution rate for trapped gas atoms
ν	Vibrational frequency of a trapped He atom
E_d	Detrapping energy for an He atom in a vacancy
D_{He}	Diffusion coefficient for He
k_{He}^2	Microstructural sink strength for He
C_v	Vacancy concentration
n	Number of vacancies in a cavity
x	Number of gas atoms in a cavity
\dot{n}	$\frac{\partial n}{\partial t}$ – rate of change of n with time
\dot{x}	$\frac{\partial x}{\partial t}$ – rate of change of x with time
n^*	Critical number of vacancies for a bubble to become a void
x^*	Critical number of gas atoms for a bubble to become a void
S_e	Effective vacancy supersaturation
S_v	Vacancy supersaturation
C_v^e	Thermal equilibrium vacancy concentration
Ω	Atomic volume
$\beta_{i,v,x}^0$	Arrival rates of self-interstitials, vacancies and gas atoms at a hypothetical void of one vacancy
K_x^C	Probability of radiation re-solution, per gas atom

Term Meaning

a Material lattice spacing; unit cell length

Chapter 1

Introduction

The aim of this work is to provide some guidance towards the development of a structural material for use in future fusion power plants. The first wall of such a power plant is the structure surrounding the reaction plasma, and is exposed to high temperatures and stresses, and the constant impact of high energy particles emitted from the plasma. There is currently no experimental facility for simulating such conditions, and so the data available on these effects are limited in both number and direct relevance.

The approach used here is the application of an established materials modelling technique, using artificial neural networks (ANNs), to an area where it has not been used before. The effects of radiation on various material properties in a group of candidate first-wall materials, reduced-activation martensitic steels, have been modelled and approach to improving the resistance of these steels to radiation damage is evaluated. A classical thermodynamic approach to modelling another longstanding problem – the nucleation of voids in irradiated steels – is also examined.

An overview of the materials problems associated with fusion power generation is provided in Chapter 2.

Chapter 3 reviews some of the problems of modelling complex properties, and the Bayesian neural network modelling method used in this work.

Chapter 4 details the practicalities of creating a Bayesian neural network, and describes the use of genetic algorithms to optimise the materials properties modelled by such a network.

Chapter 5 describes the ANN model for yield stress and the dataset used in its creation, and the use of this model to aid the optimisation of the composition of reduced-

activation martensitic steels for use in fusion reactors.

Chapter 6 describes the construction and exploration of a neural network model for radiation embrittlement.

The further use of these models to suggest the most informative experiments to be carried out in future experimental facilities is described in Chapter 8.

Chapter 7 explores methods of minimising void swelling in irradiated steels.

Chapter 9 reviews the conclusions reached from the previous chapters and explores further research avenues suggested by this work.

Chapter 2

First-wall materials in fusion power plants

2.1 Introduction

At a time when global energy demands are steadily growing, the need for energy sources that do not rely on fossil fuels is becoming increasingly obvious. Alternative sources of energy are required, to mitigate the effects of global warming in the short term, and to sustainably and cleanly continue to provide energy in the long term. Fusion power, generated by the combining of atomic nuclei at extremely high temperatures, has the potential to contribute greatly towards these demands (Lako et al., 1998). Presuming it is commercially and technically feasible, it is a CO₂ free and virtually inexhaustible energy source. There are, however, formidable engineering challenges still to be overcome in the design of such a power plant. Among these is the need to identify materials which will remain structurally reliable under exposure to the ferocious radiation emitted by the reaction plasma. The performance of these materials will, to a large extent, determine the commercial success (or failure) of a fusion power plant, by affecting the plant reliability, refuelling and replacement downtime, and waste production; the thermal efficiency of the plant is also determined by the maximum allowable temperature in the first-wall structure. The problems faced by such a material are outlined below.

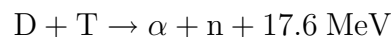
The current international “fast track to fusion” programme calls for a reactor to test control systems and plant engineering (the to-be-built International Thermonuclear

Experimental Reactor, ITER) to run concurrently with a fusion-spectrum material irradiation facility (the International Fusion Materials Irradiation Facility, IFMIF, still to be agreed) (Konishi, 2004). These will be followed, around the 2040s according to current plans, by power-generating fusion plants – the set of present designs of the first (demonstration model) of which are collectively referred to as DEMO (Bloom et al., 2004).

Steady advances in the science and technology of fusion energy – both in materials issues and plasma control – have increased the possibility of demonstrating practical fusion power generation within the next fifty years. However, if these advances are not consolidated, the prospect for fusion to markedly contribute to stabilisation and control of global CO₂ emissions may be missed.

2.2 The first-wall environment

In ITER and future commercial magnetic confinement fusion power plants (such as the DEMO designs), the source of energy is the reaction between hot deuterium (symbol D) and tritium (symbol T) nuclei in a plasma chamber. To overcome the repulsion between atomic nuclei, the plasma is accelerated to energies equivalent to a temperature of around 100 million degrees Celsius. The reaction is



The products of this reaction are alpha particles – helium ions, which are contained by the magnetic field – and neutrons – which are not. These neutrons, which have a characteristic energy peak around 14 MeV (with the remainder of the reaction energy given to the α particle), are absorbed in the surrounding material structure of the plant, transferring the heat of the reaction to an external cooling circuit and, ultimately, into electricity.

This relentless bombardment of the first wall causes a number of problems for the material designer. Firstly, the temperature of the material is raised (the design operating temperature for a commercial reactor, based on the DEMO design, is in the region of 500 - 550°C (Toschi et al., 2001)); secondly, as neutrons are not deflected by electrical fields, they can impact the atomic nuclei of the material, causing *activation*

2.2 The first-wall environment

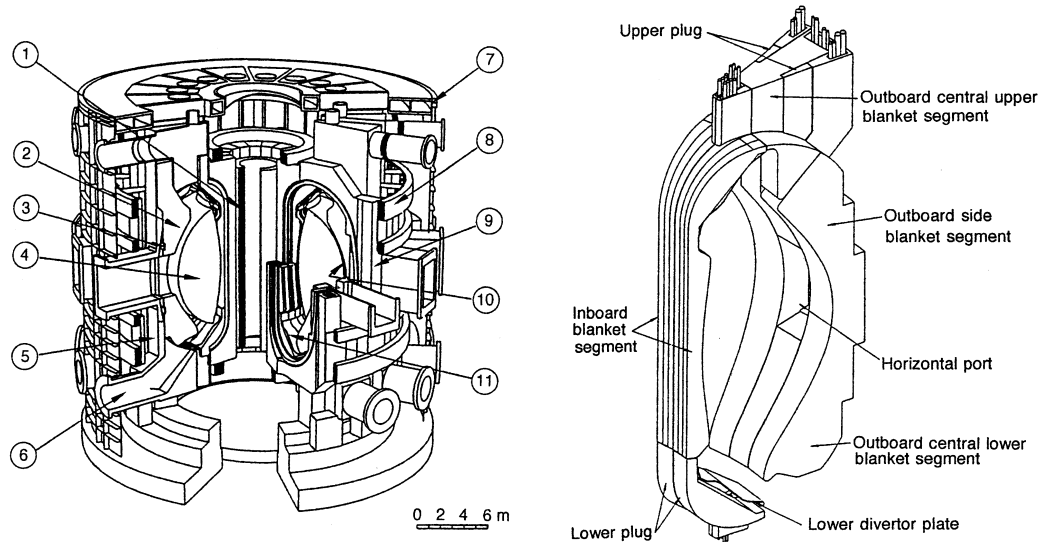


Figure 2.1: Left: Schematic diagram of a tokamak fusion reactor. 1: central solenoid; 2: shield/blanket; 3: active coil; 4: plasma chamber; 5: vacuum vessel shield; 6: plasma exhaust; 7: cryostat; 8: poloidal field coils; 9: toroidal field coils; 10: first wall; 11: divertor plates. Right: Schematic diagram of a first-wall/blanket segment around the plasma chamber of a tokamak reactor (Smith et al., 1994).

– that is, the material becomes radioactive, resulting in production of *in situ* helium (highly insoluble in steels, and a cause of embrittlement and void formation), and must be treated as radioactive waste once removed from service; and thirdly, atoms are knocked out of position throughout the material as the neutrons decelerate. The last of these forms of damage severely disrupts the structure of the material, generating excess concentrations of vacancies and self-interstitials and increasing the dislocation density. These changes have strong effects on the mechanical properties of the material, and also on the diffusion rates of alloying species. It is calculated that, in the five-year design lifetime of a typical first-wall component, the material will experience *displacement damage* of up to 200 atomic lattice displacements per atom¹ (dpa) and will contain transmutation helium gas at levels of up to 2000 atomic parts per million (appm) (Ehrlich et al., 2000). There have been attempts to incorporate radiation effects into the structural design criteria for ITER, based on results from fission reactors and

¹That is, each atom will, on average, be displaced from its lattice position 200 times during service. Details of how this figure is calculated can be found in Mansur (1987a), starting on page 399.

2.2 The first-wall environment

	ITER	DEMO-like reactor
Component replacements	None	5 year cycle
Average neutron fluence (MW yr m ⁻²)	0.3	10
Displacement damage (dpa)	3 (SS)	120 (RAFM)
Helium production (appm)	30	1200
<i>Normal operation</i>		
Number of cycles	30000	<1000
Peak particle flux (10 ²³ m ⁻² s ⁻¹)	0.01	0.02
Surface heat flux (MW m ⁻²)	<0.5	<1
PFM operating temperature (°C)	Be: 200 - 300	W: 550 - 700

Table 2.1: Operating conditions for the first-wall components of ITER and a DEMO-like reactor. As ITER will be an experimental reactor, the projected number of cycles will be very much higher than any commercial power plant reactor (Bolt et al., 2002). PFM = Plasma facing material, SS = stainless steel, RAFM = reduced activation ferritic/martensitic steel, dpa = displacements per atom, appm = atomic parts per million. MW yr = megawatt years – 1 MW yr \approx 31.5 TJ.

other current experimental data (Majumdar and Smith, 1998). Table 2.1 summarises the operating conditions for ITER and a DEMO-like reactor, and Table 2.2 summarises the functions and requirements of the blanket structure.

Many of these effects have been observed in accelerated-particle experiments and in fission reactor materials. However, there is currently no suitable source of fusion-spectrum neutrons to carry out the experiments required to test and validate predictions which have been extrapolated from the current low-flux, low-neutron-energy database. It is hoped that construction of IFMIF (see section 2.4, below), as well as experiments carried out in the to-be-constructed ITER, can remedy this lack (Barabash, 2004).

2.2.1 Activation of irradiated materials

As neutrons are uncharged particles, there are no significant repulsive forces between them and an atomic nucleus. Therefore, the chances of an atomic nucleus being directly hit by a neutron under irradiation can be high. On impact, the neutron may be absorbed by the nucleus, creating an unstable, radioactive atom. The energy of the impact can also knock other particles out of the nucleus with similar effect. The

Primary functions of the blanket

- Convert energy into sensible heat
- Breed tritium for the fuel cycle

Primary requirements of the blanket

- Adequate tritium production
 - Acceptable tritium recovery
 - Efficient heat recovery
 - Acceptable reliability and operating lifetime
 - Ease of assembly, maintenance, and repair
 - Acceptable post-irradiation environmental impact
 - Acceptable economics
-

Table 2.2: Functions and requirements of a fusion power-plant blanket structure. Tritium breeding occurs through the use of coatings such as lithium, which produce tritium under neutron bombardment (Smith et al., 1994).

process of an initially stable material becoming radioactive in this manner is termed activation, and is an issue for any material that will be used in high-energy irradiation environments.

The half-lives of resultant radionuclides can be thousands of years – once the useful life of the material is over, it must be handled as radioactive waste. The design code for fusion power plant structural steels calls for them to satisfy (at least) US Department of Energy Class C waste conditions – that is, the radioactivity should decay to an acceptable maximum level within 100 to 500 years (Abe et al., 1994). The class of steels known as reduced activation ferritic/martensitic (RAFM) steels generally meets this criterion, as solvent Fe meets the class C limit. However, some typical steel alloying elements such as Mo, Nb, Ni, and N must be significantly reduced in concentration in these alloys as they form long-lived radionuclides. In general, the total concentrations for such undesirable elements, C , must be such that

$$C = \sum_i \frac{c_i}{c_{i,max}} \leq 1$$

in which c_i and $c_{i,max}$ are, respectively, the concentration of an alloying element and its maximum permitted concentration. These are tight constraints, at the limits of both detection and readily obtainable purity for some elements. Niobium, for example, has

2.2 The first-wall environment

Element	Waste disposal limit	Recycle limit	Recycle limit (300 yr)
Ni	15 - 38%	87 - 470	1.6 - 4.3%
Mo	31 - 37	3.6 - 20	4.1 - 23
Ag	1.2 - 2.7	0.012 - 0.026	0.017 - 0.036
Co	19% - no limit	2.3 - 14	0.53 - 18%
Nb	2.4 - 3.5	0.055 - 0.08	0.055 - 0.08
Al	660 - 3900	13 - 79	13 - 79
Cu	73% - no limit	160 - no limit	20% - no limit

Table 2.3: Limits for various impurity elements for shallow land burial and hands-on materials recycling, assuming 100 yr (or 300 yr) cooling time after a 20 MW yr m⁻² exposure. The lower limit is for the first wall alone; the higher limit is for the blanket average. Concentrations are in wt% (units given) or wppm (no units given) (Klueh et al., 2000).

a c_{max} of <3 weight parts per million (wppm) (Butterworth and Giancarli, 1988).

Principal alloying elements in RAFM steels are Cr, W, V and Ta, which have no (or very high) c_{max} (Table 2.3). The activation of these elements, and hence the material as a whole, can be calculated using activation cross-section and decay codes such as the European Activation System (EASY) code (Forrest, 2001). In general, the properties of these steels are similar to those of their commercial counterparts for appropriate alloying-element substitutions and heat treatments (Bloom, 1998). However, as the data available for these steels are more limited in scope than for commercial steels, less work has been done to find optimum compositions and heat treatments for particular applications. An approach to optimisation of the properties of RAFM steels is described in Chapter 4, and applied in Chapters 5 and 6.

2.2.2 Displacement damage

A neutron slows down within a first wall material through impacts with atoms in the material. These impacts produce a *collision cascade* as the atoms recoil, passing their energy onto other atoms, which recoil in turn. This results in a central core of the cascade which has a high density of vacancies, surrounded by a cloud of self-interstitial atoms (SIAs) (Figure 2.2). The majority of these point defects rapidly annihilate with one another, but many remain to migrate into the bulk or form extended structures such as interstitial loops or clusters.

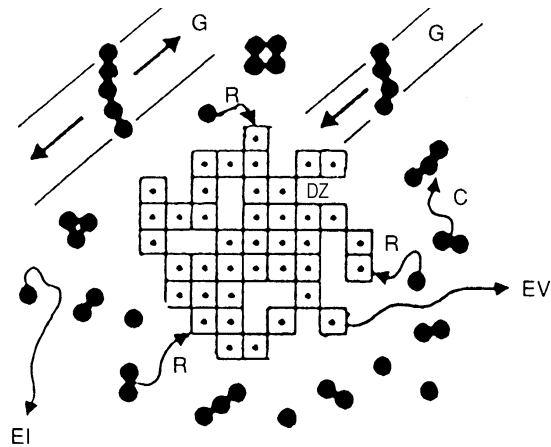


Figure 2.2: Schematic representation of the defect arrangement in a displacement cluster showing the vacancy-rich core (the denuded zone, DZ) and the interstitial shell containing mono-, di-, tri-, *etc.*, SIAs up to small loops. Vacancies are represented as the hollow squares, interstitials as black circles. The possible effects of thermal defect mobilities are intracascade recombination reactions (R), clustering reactions (C), and glide of small interstitial loops (G). EI and EV denote escaping interstitials and vacancies (Ullmaier and Trinkaus, 1996).

Such cascades and the immediate structures formed have been modelled through molecular dynamics (MD) (Bacon et al. (2000); Caturla et al. (2000) and Figure 2.3) and observed experimentally in metals such as tungsten and platinum using a field ion microscope (FIM) (Seidman et al. (1981); Wei et al. (1981) and Figure 2.4).

The result of this constant production of point defects is a range of microstructural evolution effects, which affect the macroscopic properties of the material. The formation of additional dislocation loops, raising the dislocation density, causes hardening of the material. In the presence of transmutation helium, vacancy clusters can be stabilised long enough to grow into voids, causing the material to swell by up to tens of percent, as well as adversely affecting the material properties (Mansur, 1987a, 1994). This effect is examined in more detail in Chapter 7. The increased vacancy concentrations also allow heightened rates of diffusion of alloying species, which can result in the composition of the alloy being drastically altered without triggering phase transformation, especially in the vicinity of microstructural sinks such as grain boundaries, cavities, and precipitates. This is termed radiation-induced segregation (RIS), and in

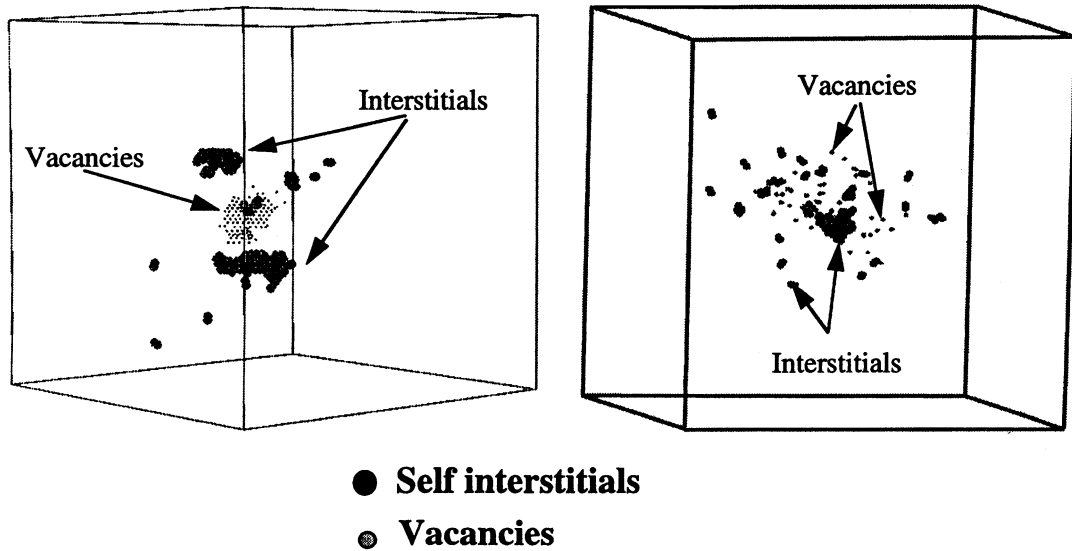


Figure 2.3: Distribution of vacancies (small dots) and interstitials (large dots) for cascades in Cu, caused by a 20 keV Cu ion (left) and Fe, caused by a 20 keV Fe ion (right) after 10 ps of an MD simulation (Caturla et al., 2000).

cases where it eventually results in a phase change or precipitation, radiation-induced precipitation (RIP).

2.3 Candidate first-wall structural materials

Several materials that are being considered as candidate first-wall materials are reviewed below. For near-future applications, 8-12 wt% Cr martensitic alloys show the most promise and are the main subject of the research presented in this work. In the longer term, it seems likely that silicon carbide fibre/silicon carbide matrix (SiC_f/SiC) composites may be adopted if they live up to early promises.

The major issues for these materials, as well as their resistance to radiation damage, are: ease and economy of manufacture; joining of the material during the building of complex structures while preserving the radiation and structural properties of the material; and compatibility with other materials in the blanket, such as tritium-breeding materials.

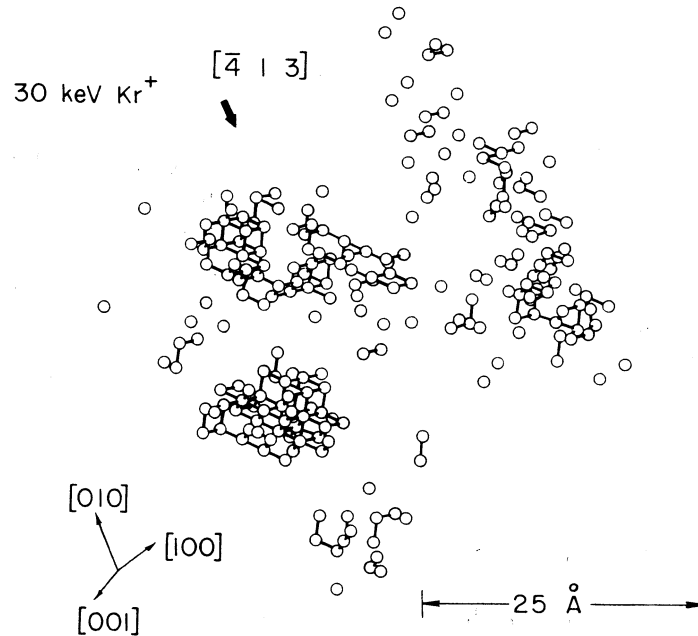


Figure 2.4: A visualisation of an FIM observed vacancy structure of a cascade in tungsten created by a single 30 keV Kr^+ projectile ion. The rods connecting vacancies represent the first-nearest-neighbour distance and hence indicate clustering (Wei et al., 1981).

2.3.1 Vanadium alloys

Vanadium alloys are attractive candidate first wall materials. They have low activation characteristics and promise desirable high-temperature strength, good resistance to radiation damage, and useable fabrication properties. The majority of development work for fusion applications has been carried out on the V-Cr-Ti system, with the principal reference composition 4 wt% Cr-4 wt% Ti. Thermal creep data suggest, though, that this alloy will be limited to a maximum operating temperature of around 700°C. Altering the Cr content can improve the high-temperature properties, but makes the alloy markedly more susceptible to embrittlement caused by radiation damage. Moreover, little experimental work has been carried out to higher damage levels (data exist extending up to 4 dpa), and the irradiation creep database is very sparse. There is also a lack of data on the irradiation characteristics of weld metals (Bloom et al., 2004; Chen et al., 2004; Kurtz et al., 2004).

2.3 Candidate first-wall structural materials

There is increasing experimental and modelling work on alternative-composition and multiphase-microstructure vanadium alloys, which may demonstrate sufficient future performance to meet the structural design criteria for components of a commercial fusion power system.

2.3.2 Ferritic/martensitic steels

The current leading candidate first-wall structural material for near-future fusion systems is reduced activation ferritic/martensitic (RAFM) steels. These are generally 8-12 wt%Cr steels, in which the usual commercial alloying elements have been replaced with low-activation equivalents as described in Section 2.2.1. Ferritic steels are preferred to the stainless/FCC steels often used in fission reactors due to the markedly lower swelling observed in the ferritic steels under irradiation (Garner et al., 2000). The development and experimental database of these materials are also considerably more advanced than competing first-wall materials.

RAFM steels exhibit hardening and embrittlement under irradiation. Increasing quantities of data exist and significant progress is being made on modelling these changes in properties (Chapters 5 and 6). One major additional limitation is high-temperature creep resistance, which limits the use of these steels to around 550°C or below.

The production of RAFM steels with low impurity levels has been demonstrated (although not sufficiently low to reduce post-irradiation activity to hands-on levels), and various welding methods have been demonstrated to produce satisfactory (at least mechanically) welds. However, the performance of weld metals under irradiation still needs to be properly evaluated, although careful engineering design could protect joints from the most severe radiation damage (van der Schaaf et al., 2000).

Current key unresolved issues related to RAFM steels include incomplete understanding of radiation effects on fracture properties; details of the role of helium in swelling, and also its effect on fracture properties; and potential adverse effects on plasma control arising from the ferromagnetism of the steel.

It is currently planned to incorporate a test blanket module using the RAFM 8 wt%-Cr steel F82H into ITER – an important milestone in the engineering of a commercially viable power plant (Shiba et al., 2004) – and the 9 wt%-Cr Eurofer has been suggested

for the DEMO blanket (Boccaccini et al., 2004). Future developments include dispersing fine ceramic oxide particles throughout a RAFM matrix, leading to improved high-temperature properties and described in more detail below (Jitsukawa et al., 2004).

2.3.3 Oxide dispersion strengthened alloys

Oxide dispersion strengthened (ODS) alloys for use in fusion applications generally consist of an ultrafine (~ 2 nm diameter) dispersion of Ti-, Y-, and O-enriched particles in a Fe-Cr ferritic or martensitic matrix. This microstructure is generally produced through mechanical alloying. They offer the benefits of RAFM steels, and additionally, increased creep resistance and potentially greater high-temperature strength (and hence, higher operating temperatures), and higher resistance to swelling due to a high density of microstructural traps for helium (see Chapter 7). The mechanical properties of ODS alloys are very sensitive to microstructure, and it might be inferred that the large lattice misfit of Ti and Y atoms would cause them to diffuse slowly in an iron lattice. However, the high concentration of vacancies in the lattice produced by radiation may allow significantly faster diffusion of these species and so, instability of the microstructure at high damage levels (Monnet et al., 2004). The microstructure also makes joining of ODS steels difficult whilst preserving the benefits of the dispersed particles. Current experimental results, though – up to displacement damage levels of 6 dpa – are very promising (Alamo et al., 2004; Cho et al., 2004; Miller et al., 2004).

2.3.4 SiC_f/SiC composites

Silicon carbide fibre reinforced-silicon carbide matrix ceramics have been shown to have an exceptional blend of qualities that makes them potentially suitable as a first-wall fusion material. These include high corrosion resistance, low activation characteristics, limited void swelling, and the retention of strength and fracture properties to temperatures in excess of 1000°C. However, there are some fundamental issues which have to be overcome: high production of transmutation gas; radiation effects on mechanical properties; and engineering issues such as joining and hermeticity (which may require the use of coatings).

Despite these issues, there exist several blanket designs which have been studied to exploit the potential of SiC_f/SiC composites, and there is some confidence that a

reliable first-wall material may eventually be obtained (Bloom et al., 2004; Riccardi et al., 2004).

2.4 The International Fusion Materials Irradiation Facility

One major outstanding issue in the modelling of irradiation effects, as mentioned above, is the extrapolation of models from the lower-energy and fission-relevant regime – where there is a goodly range of data – to the high-dose, high-energy fusion-relevant regime, where past experience suggests that there is a good chance of encountering surprises not predicted by existing theories. Experiments in ITER will provide much valuable information, but will be limited in terms of maximum damage and helium levels achieved (up to 5 dpa and 70 appm respectively), as well as suffering from operational constraints such as variable irradiation temperatures (Barabash, 2004). IFMIF, if and when built, will provide suitable experimental facilities for testing the predictions of mechanistic models on candidate power plant materials by simulating a stable, sustained fusion irradiation spectrum (Möslang et al., 1998). The design for IFMIF consists of two 40 MeV deuteron linear accelerators, focused on a molten lithium target, producing high-energy neutrons (Jameson et al., 2004). IFMIF is intended to carry out materials experiments concurrently with the operation of ITER, providing a high-quality database to assist the engineering of a commercial fusion power reactor.

However, the available experimental volume in the high-flux region in IFMIF is ~ 0.5 litres, and the highest-damage (≥ 150 dpa) experiments will last 5 years or more, meaning that experiments must be carefully chosen to make best use of this space. Considerable progress has been made in developing sub-size experimental specimens for this purpose, and the reliability of small specimens for evaluating the properties of RAFM steels has been established (Möslang, 2005). This is, however, a mixed blessing as in some cases (for example, Charpy ductile to brittle transition temperature measurements) the specimen size has a significant effect on experimental results and hence these results cannot easily be compared with existing full-size data.

The choice of candidate experimental materials and irradiation regimes must be optimised to maximise the useful information gained from IFMIF experiments. The

2.4 The International Fusion Materials Irradiation Facility

use of artificial neural network (ANN) models to help design optimally informative experiments is discussed in Chapter 8.

Chapter 3

Modelling complex properties

A reliable fusion power-plant design should ideally be based on a comprehensive, multivariate materials database well-populated with the measured mechanical properties of potential materials, fully covering the ranges of physical conditions expected. Such a database would take many years and be very expensive to assemble. At present, few data exist on candidate alloys at high dpa and there are no high-dose data at fusion-relevant He/dpa ratios.

There are many properties in materials science that can be modelled simply and analytically, such as crystallisation kinetics or the tensile properties of carbon fibre composite materials. However, in some cases the property arises from many interacting effects, not all of which are well understood, and simplification of the problem is unacceptable from an engineering point of view. For example, the yield stress of a metal cannot be calculated from first principles, although it is known to depend on variables such as grain size, dislocation density, *etc.*

In cases like these, and in the absence of a comprehensive experimental database, properties can be estimated based on models that have been fitted to the available empirical data. It is important therefore to establish techniques that make the best use of existing complex, multi-dimensional data that are sparse, not uniformly distributed in the variable space, or both. The purpose of the data-fitting is to assess the contribution of each input parameter to the output, and to make quantitative, rather than merely qualitative, predictions. In this section, some techniques of data analysis (which will be used later) are presented.

3.1 Artificial neural networks

3.1.1 Two approaches to probability

There are two ways to approach probability. Perhaps the most common, in everyday life at least, is to use a probability to describe the frequency of occurrence of an event, all other things being equal. For example, an unbiased coin toss can be said to have a probability of coming up heads of $p_H = 0.5$, because over a large number of previous tosses it has come up heads roughly half the time and we assume it will continue to do so in the future. However, this approach requires large numbers of previous events to obtain a useful value for the probability.

What happens if we have no prior assumptions and only a few occurrences to draw from? For example, if we find a coin and toss it ten times, and it comes up heads three of those times, what can we say about the probability that it will come up heads on the eleventh toss? A *frequentist* approach would say that the probability of the $(N + 1)$ th toss being heads is $\frac{H}{N}$, where H is the number of heads in N previous tosses - *i.e.* $p_H = 0.3$. This assumes that the past few throws absolutely represent the most plausible hypothesis, and makes the prediction based on that hypothesis.

However, if we fully apply the rules of probability theory¹ then we obtain

$$P((N + 1)\text{th toss is heads} | N, H) = \frac{H + 1}{N + 2} = 0.333$$

(for our example)². This prediction takes uncertainty into account by *marginalising* over all possible values of p_H – that is, the final prediction takes into account all possible ways in which three heads could be achieved from ten coin tosses (a highly biased

¹These rules are the *product rule*

$$P(x, y | \mathcal{H}) = P(x | y, \mathcal{H})P(y | \mathcal{H}) = P(y | x, \mathcal{H})P(x | \mathcal{H})$$

and the *sum rule*

$$\begin{aligned} P(x | \mathcal{H}) &= \sum_y P(x, y | \mathcal{H}) \\ &= \sum_y P(x | y, \mathcal{H})P(y | \mathcal{H}) \end{aligned}$$

where \mathcal{H} represents the assumptions on which the probabilities are based.

²This result is derived in Appendix A.

coin, a slightly less biased coin, and so on), and the probability of our observation having been achieved each of those ways. This leads to less extreme predictions than the frequentist model. It should be noted, also, that as N increases, the correct prediction and incorrect prediction tend towards one another – as we would expect, as an infinite number of tosses should provide us with the full distribution function.

The product rule can be rearranged into *Baye's theorem*:

$$P(y|x, \mathcal{H}) = \frac{P(x|y, \mathcal{H})P(y|\mathcal{H})}{P(x|\mathcal{H})} \quad (3.1)$$

That is, the probability of a model (y) given the data (x) and the assumptions (\mathcal{H}), is equal to the probability of the data given the model (and assumptions) multiplied by the probability of the model, *regularised* by the probability of the data over all models. Applying this allows us to assess how well a model performs in describing data, and hence provide a quantitative measure of the *believability* of that model. This believability is the inverse of the *modelling uncertainty*.

Also, the probability calculated using this approach is dependent on the assumptions made - it is therefore known as the *subjective* (or *Bayesian*) interpretation of probability. Supporters of this approach to data analysis view this subjectivity as an asset rather than a defect, as it makes the assumptions explicit and one “cannot do inference without making assumptions” (MacKay, 2003).

3.1.2 Bayesian neural networks

An artificial neural network (ANN) is basically a method for fitting a curve to a number of points in data space (Bhadeshia, 1999). More technically, it is a parameterised non-linear model which can be used to perform regression, in which a flexible, non-linear function is fitted to experimental data. The term “artificial” is used to indicate that these networks are computer programs, rather than “real” neural networks such as the human brain. The details of the operation and construction of neural networks have been reviewed elsewhere (Bishop, 1995; MacKay, 2003), but it is useful to summarise the main features here.

We assume that the material property of interest, for example the yield stress σ_y , can be expressed as a non-linear function, f , of a number of experimental variables in

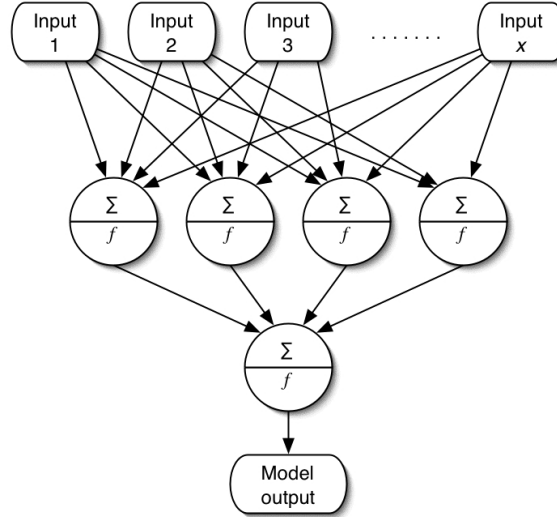


Figure 3.1: A schematic diagram of a three-layer feed-forward network. The model’s complexity is controlled by the number of neurons in the second layer, known as hidden units.

the database.

$$\sigma_y = f(\{c_i\}, c_{He}, CW, K, t, T_{irr}, T_{test}, \dots) \quad (3.2)$$

where $\{c_i\}$ is the chemical composition of the alloy, c_{He} the concentration of any transmutation helium produced, CW a parameter to describe any cold-working treatment prior to irradiation, K the irradiation damage rate (in dpa s^{-1}), t the duration of the irradiation, T_{irr} and T_{test} the irradiation and tensile test temperature, and \dots representing any other parameters which might be thought to influence the yield stress.

The aim of neural network training is to make as few assumptions as possible about the form of this function, whilst attempting to infer and thus mimic its shape. In fact, the only assumptions we make of this form are that it is continuous and differentiable. It has been shown that a sufficiently complex three-layer network of the form described below can imitate any such function (MacKay, 2003). The network is thus able to respond flexibly to the demands made by the data, capturing any non-linear interactions between the parameters.

Such a three-layer feed-forward network, of the type commonly used for material property applications, is shown in Figure 3.1. The first layer consists of the inputs to

3.1 Artificial neural networks

the network. The second layer consists of a number of *neurons* – non-linear operators whose arguments are provided by the first layer in the network. The activation function for these neurons, h_i , can be any non-linear, continuous and differentiable function – tanh has been used in this work (Equation 3.3). The overall output function, y , can again be any function, and is commonly linear. The neuron activation function for a neuron i is given by

$$h_i = \tanh \left(\sum_j w_{ij}^{(1)} x_j + \theta_i^{(1)} \right) \quad (3.3)$$

and the output weighting function is

$$y = \sum_i w_i^{(2)} h_i + \theta^{(2)} \quad (3.4)$$

The x_j are the inputs, and w the weights which define the network. ⁽¹⁾ and ⁽²⁾ denote weights and biases in the hidden layer and in the output layer, respectively. The aim of training a network is to find the optimum set of values for w . The parameters θ are known as *biases*, and are treated internally as weights associated with a constant input set to unity.

In order to simplify the weightings, inputs are normalised within a range of ± 0.5 . The normalisation function is

$$x_j = \frac{x - x_{\min}}{x_{\max} - x_{\min}} \quad (3.5)$$

where x is the un-normalised input, x_{\min} and x_{\max} are the minimum and maximum values in the database for that input, and x_j is the normalised value. The network is therefore not constrained to a particular range of outputs (for example, positive outputs only) and so the target must be chosen with care to avoid unphysical model outputs. For example, for a property which cannot be less than zero such as the yield stress σ_y , $\ln(\sigma_y)$ could be used instead as the network training target.

The complexity of such network models scales with the number of “hidden” units. Despite the terminology and the common view of a neural network as a “black box”, the weightings can in fact be examined although they are difficult to interpret directly, being complex nested tanh functions. The easiest way to identify the interactions in

a model is to use it to make predictions and see the behaviour which emerges from various combinations of inputs.

Because of the inherent flexibility of an ANN, there is the possibility of *overfitting* the model. Training a network therefore involves finding a set of weights and biases which minimise an *objective function*, which balances complexity and accuracy, typically

$$M(w) = \alpha E_w + \beta E_D \quad (3.6)$$

in which E_w is a *regulariser*; its function is to force the network to use small weights and limit the number of hidden units and is given by

$$E_w = \frac{1}{2} \sum_{ij} w_{ij}^2 \quad (3.7)$$

and E_D is the overall error between target output values and network output values, given by

$$E_D = \frac{1}{2} \sum_k (t^{(k)} - y^{(k)})^2 \quad (3.8)$$

where $t^{(k)}$ is the set of targets for the set of inputs $x^{(k)}$, while $y^{(k)}$ is the set of corresponding network outputs. α and β are control parameters which influence the balance between a simple but inaccurate model, and an overcomplex, also inaccurate model (Figure 3.2). MacKay's algorithm allows the inference of these parameters from the data, permitting automatic control of the model complexity (MacKay, 2003).

To accomplish the training, the data are randomly split into two sets, a *training set* and a *test set*. The model is trained on the training set, and then its ability to generalise is compared against the test set of data. Figure 3.3 shows how increasing complexity continuously lowers the training error (the mismatch between model predictions and the training dataset), while the test error (the mismatch between model predictions and the test dataset) has a minimum. At greater complexities, overfitting causes the test error to increase with increasing numbers of hidden units. The ultimate purpose of training a model is to minimise this error, both against the input dataset and against unseen data from future experiments.

For these models, the fitting method is based on a Bayesian approach and treats training as an inference problem, allowing estimates to be made of the uncertainty

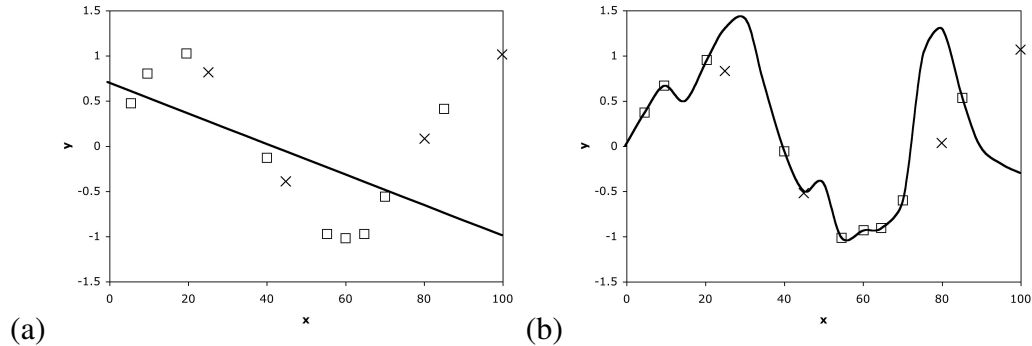


Figure 3.2: Under- and over-fitting. A set of noisy data points (hollow boxes) has been fitted by (a) linear regression and (b) an overly complex function. In the first case the fit clearly does not represent the data, and in the second case the fit overlies the training data perfectly but generalises poorly to new points (crosses).

of the model fit (Figure 3.4). Rather than trying to identify one best set of weights, the algorithm infers a probability distribution for the weights from the data presented. In this context, the performances of different models are best evaluated using the *log predictive error* (LPE) rather than the test error. This error penalises wild predictions to a lesser extent when they are accompanied by appropriately large error bars and is defined by

$$\text{LPE} = \frac{1}{2} \sum_k \left[\frac{(t^{(k)} - y^{(k)})^2}{(\sigma_y^{(k)})^2} + \log \left(2\pi (\sigma_y^{(k)})^2 \right) \right] \quad (3.9)$$

where t and y are as defined above, and $\sigma_y^{(k)}$ is related to the uncertainty of fitting for the set of inputs $x^{(k)}$. It should be pointed out that, for computational purposes, the training software (BigBack5¹) actually uses an inverse version of this function that increases with increasing accuracy.

Of course, models with different number of hidden units and different initial guesses for the distribution of the weights – the *prior* – will give different predictions. Optimum predictions can often be made by using more than one network. This is referred to as a *committee*. The prediction \bar{y} of a committee of networks is the mean prediction

¹This software was written by David MacKay, and can be downloaded from <http://www.inference.phy.cam.ac.uk/mackay/SourceC.html>

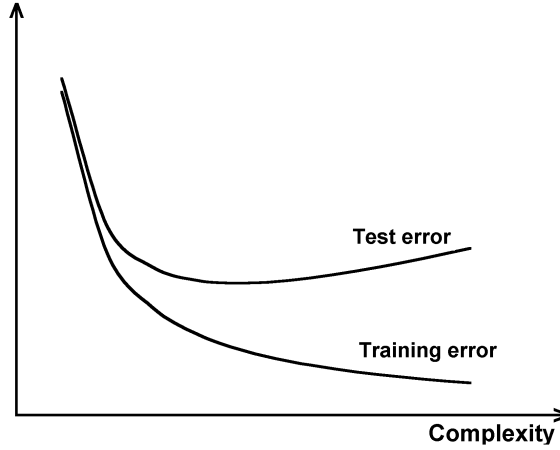


Figure 3.3: Comparison of error on training and testing sets as a function of network complexity, illustrating the problem of overcomplex models as in Figure 3.2.

of its members, and the associated uncertainty is

$$\sigma^2 = \frac{1}{L} \sum_l \sigma_y^{(l)2} + \frac{1}{L} \sum_l (y^{(l)} - \bar{y})^2 \quad (3.10)$$

where L is the number of networks in the committee and the exponent (l) refers to the model used to give the corresponding prediction $y^{(l)}$. During training, it is usual to compare the performances of increasingly large committees on the testing set of data. Usually, the error is minimised by using more than one model in the committee. The selected models are then retrained on the entire database.

A further output from the training software is an indicator of the network-perceived significance of each input. The measure provided by BigBack5 is a function of the values of the regularisation constants for the weights associated with an input, σ_w . This measure is similar to a partial correlation coefficient in that it represents the amount of variation in the output that can be attributed by any particular input.

To determine the sensitivity of the model to individual input parameters, on the other hand, predictions must be made varying one parameter only whilst keeping all the others constant. In some cases where an input is a function of one or more other inputs (for example, both temperature T and an Arrhenius function $\exp(\frac{1}{T})$ could be inputs to the network) varying only one of these parameters may not be physically

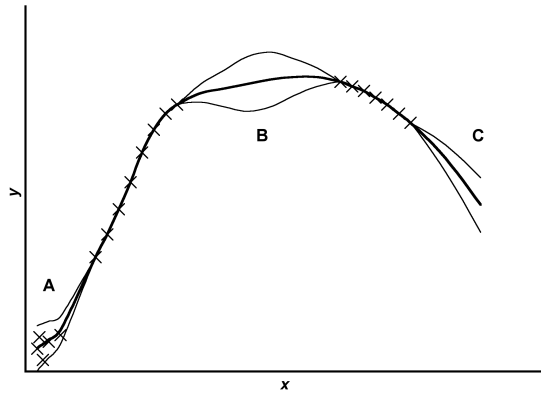


Figure 3.4: Schematic illustration of the uncertainty in defining a fitting function in regions where data are sparse (B) or noisy (A). The thinner lines represent error bounds due to uncertainties in determining the weights. Note that, outside the range of data, the extrapolation is increasingly uncertain (C). Areas of high uncertainty will provide the most informative new experiments.

meaningful.

The nature of the ANN structure (and these outputs) allows the “testing” of various physical models – input parameters based on those models can be included in the training data, and those parameters which are not useful in explaining the output will have much lower significances than those which *are* useful (Figure 3.5).

3.2 Dimensionality of the data

In modelling complex properties, we frequently encounter the “curse of dimensionality”. A materials database may have upwards of 40 input parameters, all possibly affecting the output. Handling this many inputs requires additional computing power, and potentially renders a problem intractably complex or any predictions uncertain¹.

It can be useful to gain an understanding of the *effective dimensionality* of a dataset – for example, in a dataset consisting of a number of points of 40 parameters per point, how randomly are those parameters distributed within their range? Is there any

¹A measure of this uncertainty is an automatic output from the Bayesian neural networks described earlier.

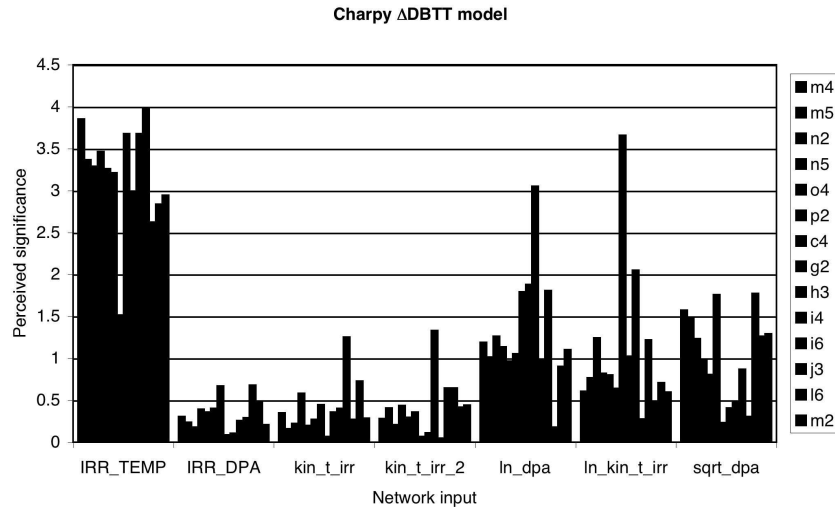


Figure 3.5: An example of a selected set of σ_w values from a committee model. In this case, the committee had 14 members (listed down the right), and the bars represent the σ_w for each member. It is notable that functions of the displacement damage such as $\sqrt{\text{dpa}}$ are given greater significances than the displacement damage (IRR_DPA) alone. This provides support for certain physical models for the effects of radiation damage (Chapter 6).

clustering? Can parameters be removed without removing significant information from the dataset (*dimensionality reduction*)? In practice, there are two reasons why extra dimensionality need not imply extra data. Firstly, there may be correlations between input variables. Adding extra inputs which are functions or combinations of extant inputs does not generate new information and therefore will not significantly increase the effective dimensionality of the dataset. Secondly (and the point which makes neural network modelling possible), the output variable is assumed to vary smoothly with the input variables and is itself a function of those variables (Bishop, 1994).

There are a number of methods of assessing the effective dimensionality of a dataset (Carreira-Perpiñán, 2002). Essentially, these involve projecting the dataset onto a space of lower dimensions, and assessing the *reconstruction error*. This metric is some measure of the error produced (and hence, the information lost) when the dataset is projected onto a space of a lower number of dimensions, and then projected back into its original data-space.

3.2 Dimensionality of the data

The method for assessing the dimensionality of a dataset described below is due to Sammon (1969), and is useful for identifying potential structures in that dataset. The original data (in L -dimensional L -space) are mapped onto a lower dimensional d -space. The distances between all points are then calculated to see how well the lower-dimensional representation has “captured” the higher-dimensional data. The error, E , is given by

$$E = \frac{1}{\sum_{i < j} [d_{ij}^*]} \sum_{i < j}^N \frac{[d_{ij}^* - d_{ij}]^2}{d_{ij}^*} \quad (3.11)$$

in which N is the number of data points, d_{ij}^* is the distance between two points i and j in L -space, and d_{ij} is the distance between the same two points after projection onto d -space (Figure 3.6).

This mapping was applied to the Charpy ductile to brittle transition temperature shift (Δ DBTT) data described in Chapter 6. This was a 32-dimensional dataset of 411 data points, the first 31 (“input”) dimensions being given by the heat treatment, chemical composition, and radiation parameters and the final (“output”) dimension being the Δ DBTT resulting from those conditions¹. Input dimensions were progressively added, and for each resulting d -space, the lowest Sammon error was calculated. It was found that if a set of dimensions $\{a, b, c, \dots, x\}$ gave the lowest Sammon error for a particular d -space, then $(d + 1)$ -space would use that same set of dimensions plus one other for *its* lowest Sammon error. This allowed the development of a more efficient algorithm, as instead of recalculating for all possible combinations of dimensions in $(d + 1)$ -space, only a small number of combinations had to be calculated.

This calculation was carried out using *Mathematica*, and the code used can be found in Appendix B. It should be noted that this approach differs from the method described in Sammon’s original paper, in which the dimensionality of d -space is decided first, and then the optimum projection (which may involve axes that are not orthogonal to the data L -space axes) is found. It was felt that the full calculation would not only be time-consuming, but also potentially frustrate the identification of important inputs.

¹“Input” and “output” are used here to maintain consistency with the previous section on neural networks, and to emphasise that the Δ DBTT parameter – which we wished to model – was always used in the mapping calculations.

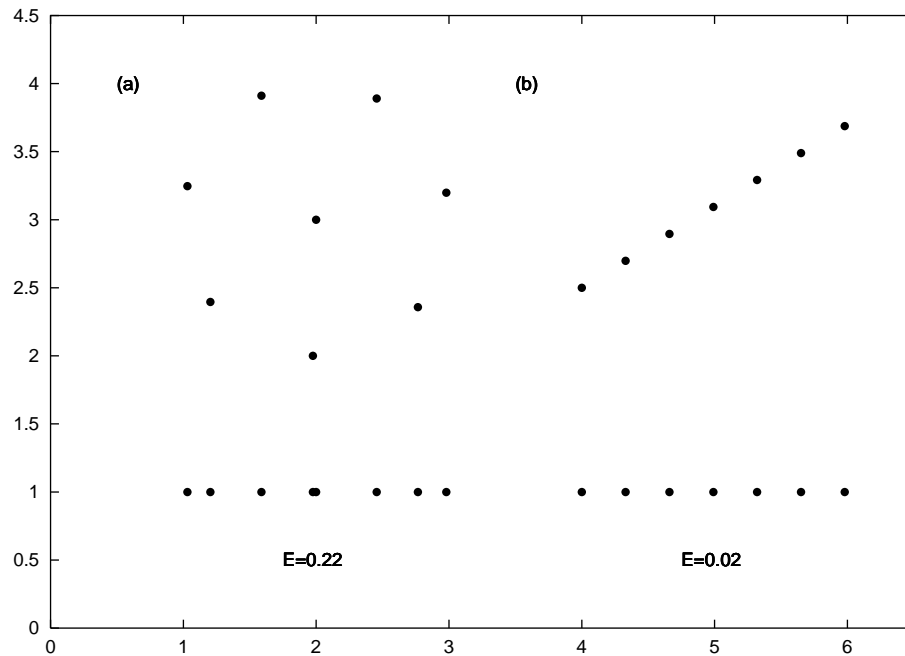


Figure 3.6: Two 2-D datasets, projected onto a 1-D line. (a) Seven points arranged in a circle with another at the centre and (b) seven points in a diagonal line. The 1-D mappings are below, with a calculation of the Sammon mapping error, E . The considerably higher error for the “circle” compared to the “line” reflects that more information is lost during projection.

The mapping error as a function of number of dimensions is shown in Figure 3.7. It is clear that although the error is large when using few dimensions (as would be expected), it rapidly falls as more dimensions are added. However, for up to 20 dimensions the error shows no sign of levelling off. The error at this point is around 0.01, which is relatively high for such a dataset (although, as previously mentioned, the axes of these dimensions are not optimised).

However, the usefulness of this technique to assess the importance of inputs is questionable. For example, the five inputs which give the lowest mapping error turn out to be W, Si, Cu, Nb, and P contents, in that order, contradicting the neural network

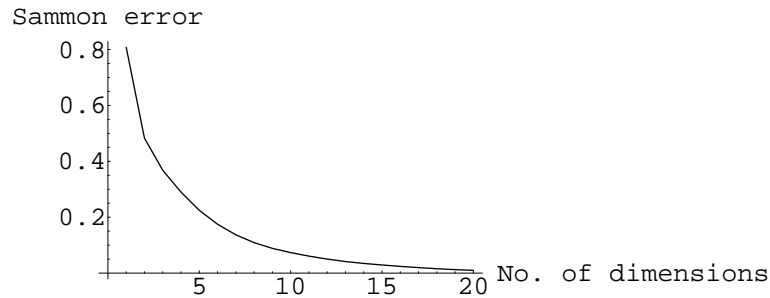


Figure 3.7: Graph of Sammon mapping error against number of included dimensions for Charpy Δ DBTT data. The output dimension was always included.

analysis (Chapter 6) which finds the irradiation conditions to have much higher significance than these elements. Closer examination of the data, though, finds that the Sammon mapping actually detects clustering in the data – the majority of the data fall into three different concentrations for W, for example, and two for Cu¹. In contrast, the data for irradiation temperature and damage are spread throughout their ranges, with little obvious clustering.

This suggests that the mapping could be used to detect deficiencies in databases by identifying parameters which lack breadth, and hence determine where experiments could be useful. However, it is a computationally intensive means to do so. In this case, it remains to be seen whether or not it is a useful tool for analysing material properties data.

¹The data distributions for each input are presented in Section 6.3.1

Chapter 4

Neural network modelling of irradiated steels

This chapter is a brief overview of the practicalities of creating the artificial neural network (ANN) models described in Chapters 5 and 6, and the use of a genetic algorithm (GA) method to find optimal sets of inputs to that model for a desired output.

4.1 Intelligent design of a neural network model

To create an ANN model of the structure described in Chapter 3 (as used in the present work), first, a database must be assembled containing the desired output property, and all input values which are perceived to be relevant in influencing that output. Ideally, this database should be well-populated over the domain of interest. Missing input variables will manifest as additional noise in the final model.

A decision must therefore be made about tolerable levels of noise in the model. Excluding some input variables can often provide a larger training database, but this may incur a penalty in that the correlation with the output is reduced.

It is important to distinguish between *noise* – the variation in experimental data-points due to uncontrolled variables – and *modelling uncertainty* – the uncertainty in a prediction due to the range of functions which will fit the data. A sparse data set may have very low noise, for example, but may be represented by a wide range of different potential functions, whose behaviour away from the data vary markedly. In those regions, this model would have large modelling uncertainty.

4.1 Intelligent design of a neural network model

Known physics can be included by incorporating functions of the input variables as additional inputs, such as the inclusion of Arrhenius terms as well as temperatures. This can also be done to better distribute the input over data space – for example, when modelling heat treatments it is usual to include $\log(\text{time})$ (Yescas-González, 2001). If these functional forms are not useful in explaining the data, they will be effectively ignored by the network, through association with near-zero weights.

Once the training database has been created, model training can commence. A series of neural networks is generated with increasing numbers of hidden units. The initial distribution of weights for each hidden unit is randomly generated – the *seed* for a network is the value which is fed to the pseudorandom number-generating algorithm at the start of this process. Keeping a record of this number allows reproducibility of the training routine, and a variety of seeds is used for each given network structure.

The training database is randomly split into two equally-sized groups – the *training* and *test* sets. Each network is exposed to the training set and the training algorithm attempts to infer the optimum distributions of weights that will allow that network to “predict” the target from the input variables. Sometimes these distributions do not converge on a finite set of values. This usually occurs because the training algorithm has been told to assume a low level of noise in data which does not justify such an assumption. In this case, the network must be retrained assuming a greater noise level, or discarded.

Additionally, during training a network can develop *symmetries* – two or more hidden units carrying out the same calculations by possessing the same weights – or *dead units* – where the weights associated with a hidden unit go to zero. In both cases the Bayesian calculations are adversely affected, and a simpler network can be found with exactly the same properties. These networks are also discarded.

Once all networks have been trained (or discarded if appropriate), their performance must be assessed. This is accomplished using the log predictive error (LPE) described in Chapter 3 for the test data set. A combination of the best-performing networks can frequently have a lower collective error than any single network. This is referred to as a *committee*. Once identified, by combining increasing numbers of networks and looking for the lowest collective error, each network in the committee is retrained by exposure to the *complete* set of data, both training and test sets. This

is done without changing the structure of each network, and in general the weights should not change dramatically.

During the retraining process, the training errors mentioned above (non-convergence of weights, symmetries, and dead units) can occur in networks which had not exhibited them before. The networks must therefore be rechecked and, if one of these errors has occurred, the relevant network must be excluded from the final committee.

Once the whole training process is complete, the final model performance must be assessed. Examination of the weights themselves, while possible, usually does not provide ready insight into how the model will behave in a given situation. The most appropriate way of assessing a model is therefore by using it to make predictions and to study trends. For example, in modelling irradiation hardening it is expected from the evolution of microstructure that there will be a rapid initial increase in yield stress followed by a levelling off at higher damage levels – this is what the model in Chapter 5 predicts.

If the model is not satisfactory at this stage, the options are to expand the database by finding more information (additional datapoints or additional input variables) or to identify better model physics – more appropriate functions of the existing input variables.

If the model *is* satisfactory, on the other hand, it can now be used to make predictions.

The procedure for creating an ANN model is summarised in Figure 4.1.

4.2 Optimisation and genetic algorithms

Once a neural network model has been trained, it is frequently desirable to use the model backwards and identify sets of input variables resulting in a desired output value. The large numbers of variables and non-linear nature of the model makes finding the optimal set of input variables difficult.

Here, we can use a *genetic algorithm* (GA) to try and solve the problem. This randomly generates sets of inputs called *chromosomes*. Each chromosome X_i is composed of a set of *genes* $[x_{i1}, x_{i2}, x_{i3}, x_{i4}, \dots]$. This set of genes, when given to the ANN model as inputs, will give the output f_i . The chromosomes are then ranked according

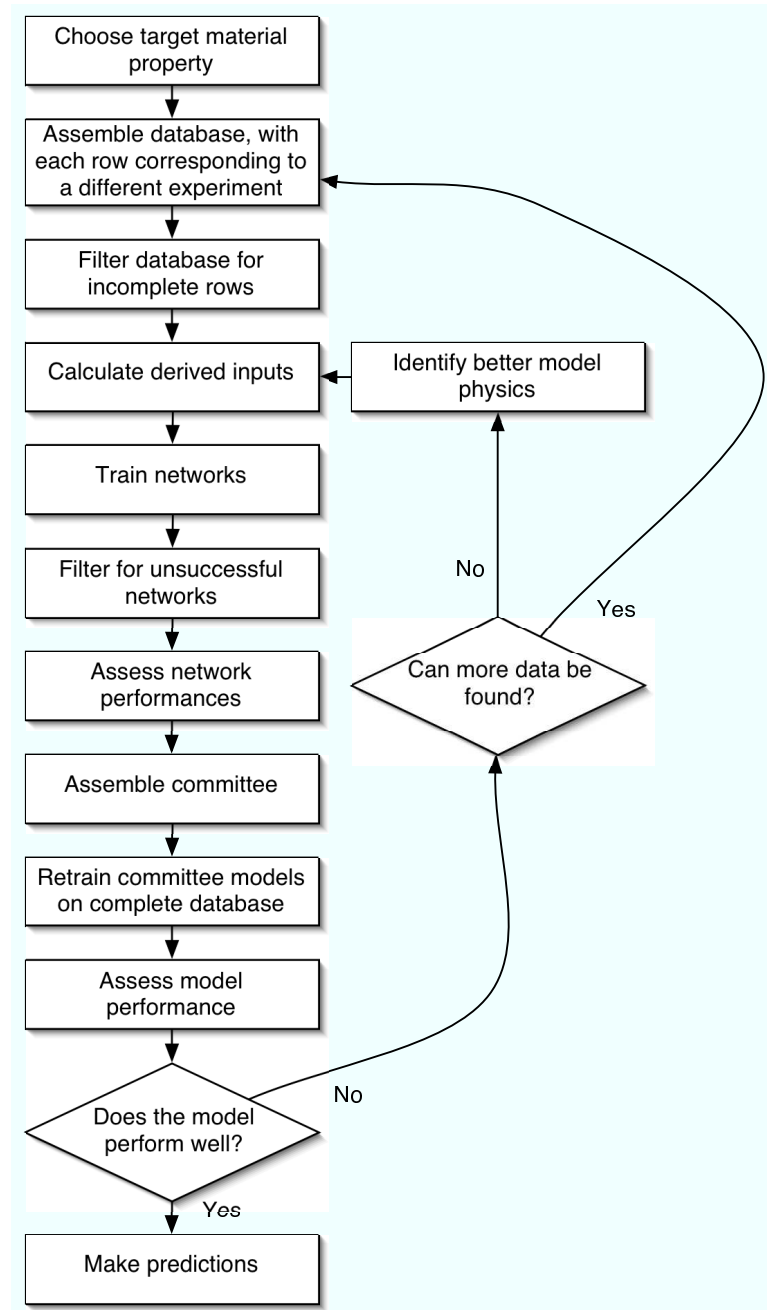


Figure 4.1: Flow diagram showing the steps in creating an ANN model.

4.2 Optimisation and genetic algorithms

to a *fitness factor*, F_i , describing how well they perform relative to expectation. In our case, this is the inverse of the standard deviation error, σ_i .

$$F_i = \frac{1}{\sigma_i} \quad (4.1)$$

where

$$\sigma_i^2 = \frac{1}{L} \sum_l \sigma_{y,i}^{(l)2} + (t - f_i)^2 \quad (4.2)$$

where L is the number of models in the predicting committee, $\sigma_y^{(l)}$ is the uncertainty associated with each committee member's prediction, t is the target value for the model output, and f_i is the committee prediction.

The “fittest” chromosomes are then allowed to “breed” – copies of them are made – and “mutate” – the genes of the copies are randomly altered by small amounts – and the process is repeated. In this way, the optimal domain of inputs (for a desired output) may be found (Goldberg, 1989). The procedure is summarised in Figure 4.2.

The GA program used for the work presented here is available from the Materials Algorithm Project (MAP) website, at <http://www.msm.cam.ac.uk/map/mapmain.html>, where a report on its creation and implementation is also available (Delorme, 2003).

In line with the recommendations in Delorme (2003), for the work presented here three different populations of chromosomes were used, with twenty chromosomes in each population. There was a crossover rate of 90% (that is, 90% of the population was varied between each generation, with the “fittest” chromosome surviving unchanged and the “weakest” replaced with a wholly new chromosome) and cross-population breeding was allowed every 200 generations. In each case, the algorithm was run for 3000 generations in total.

The genetic algorithm inputs are a target value and a permitted uncertainty. This prevents the location of “ideal” materials which have large uncertainties.

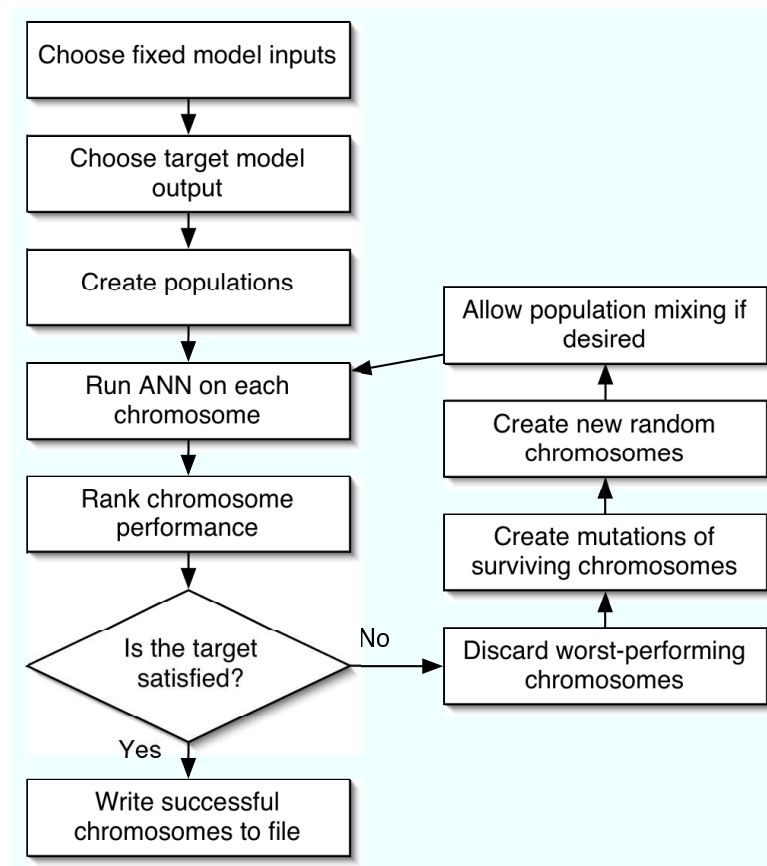


Figure 4.2: Flow diagram showing the steps in using a genetic algorithm to optimise a set of ANN inputs for a desired output.

Chapter 5

Irradiation hardening

5.1 Hardening mechanisms

Under irradiation, cascades produce point defects that form dislocation loops. These can coalesce with the existing dislocation network, resulting in an overall increase in dislocation density, causing the material to harden in a similar fashion to work-hardening. In addition, voids and precipitates may form, further impeding dislocation movement (Chaouadi and Gérard, 2005; Scattergood and Bacon, 1982) (Figure 5.1).

This behaviour can be generally described by *dispersed barrier hardening* (Bement, 1970; Hirth and Lothe, 1982). In this model the hardening effect, $\Delta\sigma_y$, of a distribution of obstacles is given by

$$\Delta\sigma_{y,\text{obstacles}} = \frac{\alpha M \mu b}{(Nd)^{-\frac{1}{2}}} \quad (5.1)$$

in which M is the Taylor factor – a parameter which describes the amount of slip required to accommodate a strain, μ is the shear modulus of the material, b is the Burgers vector and α is an additional parameter which controls the strength of the effect. Bement has provided theoretical limits on the magnitude of this parameter for different obstacles. $(Nd)^{-\frac{1}{2}}$ is the mean discrete-obstacle spacing with N being the number density of obstacles per unit volume and d their diameter (Corti et al., 1974; Martin, 1980; Taylor, 1938).

For close-spaced obstacles of similar strengths, a geometric mean can then be used

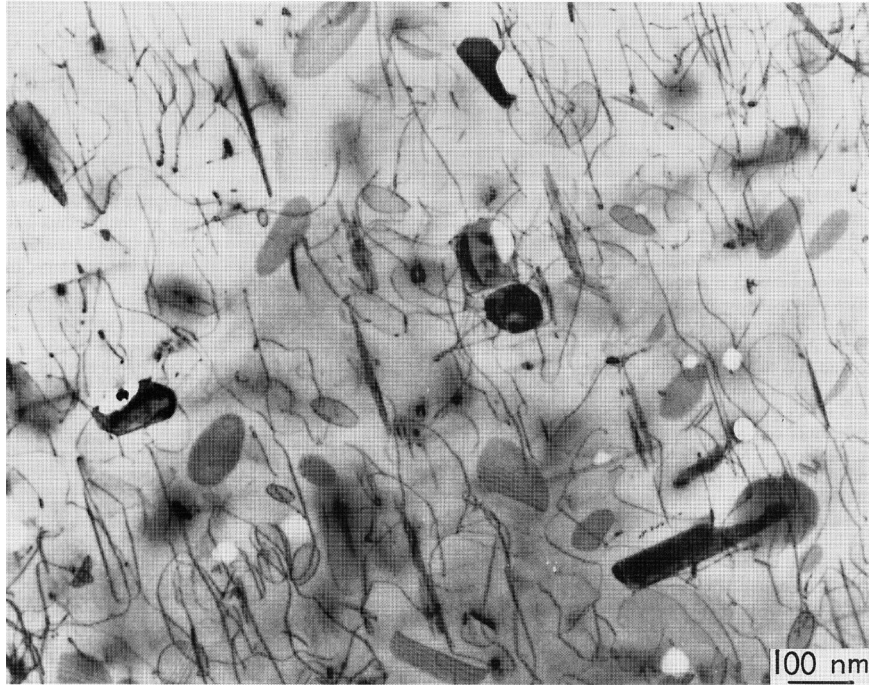


Figure 5.1: Transmission electron micrograph of a 300 series stainless steel irradiated at 500°C to a dose of 10 dpa. Dislocation loops and voids are clearly visible (Mansur, 1994).

to calculate their superposed effects (Bement, 1970).

$$\Delta\sigma_{y,\text{total}}^2 = \Delta\sigma_{y,\text{loops}}^2 + \Delta\sigma_{y,\text{bubbles}}^2 + \dots \quad (5.2)$$

A number of models exist for tracking microstructural evolution under irradiation, based on rate theory (Bullough and Quigley, 1981), Fokker-Planck equations (Semenov and Woo, 2003), master equations (Semenov and Woo, 1999), or combinations of these (Ghoniem, 1991). While these models are phenomenologically successful – that is, they generally reproduce the microstructures seen in irradiated materials – they frequently rely on assumed values for vital parameters such as void number density. The calculated microstructures then vary markedly depending on the values chosen for these parameters. Although the parameters can sometimes be deduced for a particular material (by varying them until calculated microstructures closely resemble real ones), they do not generalise well to other materials, and so estimates of changes in yield

5.1 Hardening mechanisms

stress from microstructural models are usually regarded as qualitative. There is currently no comprehensive model that can predict the hardening expected as a function of all the relevant inputs, although attempts have been made to marry dispersed barrier hardening theories to such microstructural models (Stoller (1992), for example).

Nevertheless, these models can lead to reliable qualitative relationships between radiation damage levels and changes in material properties. It can be shown, for example, that at elevated temperatures the microstructural changes can achieve a steady state – they saturate – as the rate at which defects are annealed becomes equal to the rate at which they are created (Makin and Minter, 1960). It can therefore be anticipated that the yield stress will also eventually saturate under irradiation at temperatures greater than 500 K (Murakami et al., 2000). Furthermore, in many cases little radiation hardening is observed at temperatures above 650 K. These observations suggest that a certain amount of radiation damage – excluding voids and stable precipitates – could potentially be annealed *in situ* in a manner similar to that used in fission reactors (Cottrell, 1981).

Similarly, it is expected that changes in yield stress do not depend linearly on the extent of radiation damage, but on functions of it such as \sqrt{Kt} , where K is the damage rate and t the irradiation time (Brailsford, 1979).

A further problem arises from the addition of elements such as Ni and B, which can be used to investigate the effects of helium on mechanical properties (in combination with displacement damage) (Klueh and Vitek, 1987; Mansur and Farrell, 1997). Helium is not produced in significant quantities in a RAFM steel under fast neutron bombardment in currently available facilities, but is produced by a two-step reaction of ^{58}Ni with thermal neutrons. Adding Ni at concentrations of about 2 wt%¹ allows helium to be produced under fast neutron irradiation at roughly the same helium:damage ratios that would be seen in the original, unmodified alloys in a tokamak-type fusion reactor first wall. However, the presence of such alloying elements may have additional direct effects on irradiation hardening which must be deconvoluted from the effects of any helium produced.

¹Precisely *because* nickel produces helium under neutron irradiation, the concentration of Ni is kept as low as possible in candidate fusion steels. Boron occurs as an impurity in RAFM steels (or is also deliberately added to investigate helium effects) and its concentration must be controlled.

5.2 Previous models

Diverse models exist for predicting radiation hardening in steels. These include purely curve-fitting with general saturation functions (Makin and Minter (1960); Yamamoto et al. (2003), for example) and fits using power-law functions (*e.g.* $\Delta\sigma_y = h(\text{dpa})^n$, Byun and Farrell (2004)), which make assumptions about functional relationships. As the fitting parameters vary according to material and irradiation conditions, this approach is only weakly predictive. Simple dispersed barrier models do not predict hardening saturation and more complex versions have fitting parameters which cannot be generalised (Pokor et al. (2004), for example). Some interesting work is being carried out on deformation mode mapping, which helps to explain the form of irradiation hardening curves, but these maps require experimental data across a wide range of temperatures and damage levels to build, and are not simply transferrable to different materials (Farrell et al., 2004).

As it stands, there are no previous models which flexibly estimate a range of observed behaviour and are quantitative. Bayesian neural network models are both flexible and quantitative, and also provide a measure of the modelling uncertainty, allowing calculations from far outside the knowledge base to be identified and approached with caution.

5.3 Neural network model of irradiation hardening

The Bayesian artificial neural network (ANN) used here was described in Chapter 3. Previous complicated materials problems where it has been successfully applied include the modelling and optimisation of the Charpy energy and strength of steel weld metals, the yield and ultimate tensile strength of nickel-base superalloys, the behaviour of high-temperature, creep-resistant steels, and properties of polymeric and inorganic compounds and ceramics. A review of these applications is given in Bhadeshia (1999). However, this modelling method has not previously been applied to the mechanical properties of neutron-irradiated steels, although non-Bayesian ANNs have recently been applied (with limited success) to the aging of reactor pressure vessels (Wang and Rao, 2002).

5.3.1 Yield stress database

A database of the tensile properties of a set of RAFM steels was compiled, initially primarily by Yamamoto and co-workers, from the published literature. The full list of references used in the compilation is given in Appendix C.

The database included leading candidate RAFM steels such as F82H (8Cr¹) and Eurofer 97 (9Cr) as well as conventional 9Cr steels such as T91 (9Cr–1Mo) and EM10 (9Cr–1Mo). A set of 2.5Cr bainitic steels was also included in the database. Overall, the compilation contained about 1800 experimental data, with displacement damage levels of 0-90 dpa, within a temperature range of 273-973 K. Figure 5.2 illustrates the range of many of these variables plotted against the model target – the yield stress, σ_y . These graphs are not intended to depict functional dependencies, but to demonstrate the distribution of the data. It is evident that the data are not uniformly distributed, and that further heterogeneities may exist when correlations between the input variables are considered². However, the Bayesian framework of the ANN allows it to highlight regions of the input space that lack information by associating larger modelling uncertainties with predictions made in such regions.

The input variables are listed in Table 5.1 and include most of the parameters thought to influence the strength of irradiated steel: chemical composition and degree of cold-working; irradiation temperature; test temperature; total irradiation displacement damage; and helium content. Because the algorithm is able to deduce the relevance of each individual input, it is appropriate to include all the available variables in the analysis, and those variables which are not found to greatly influence the strength are associated with minimal weights. In some cases, full compositional data were not available and in these instances the concentrations of deliberately added chemical elements were set to zero.

The data contained no information on the damage rate, K , or irradiation time, t , although these are known to be influential parameters (Carter and Soneda, 2002; Odette et al., 2005). Pre-irradiation heat-treatment was also missing for much of the data, and hence the decision was made to exclude it rather than proceed with a much reduced dataset. Heat treatments are similar, in any case, for many of the materials included,

¹This notation indicates that the steel contains 8 wt% Cr, and so on.

²The Sammon mapping procedure described in Chapter 3 should also identify these heterogeneities if sufficient computer processing time can be spared.

5.3 Neural network model of irradiation hardening

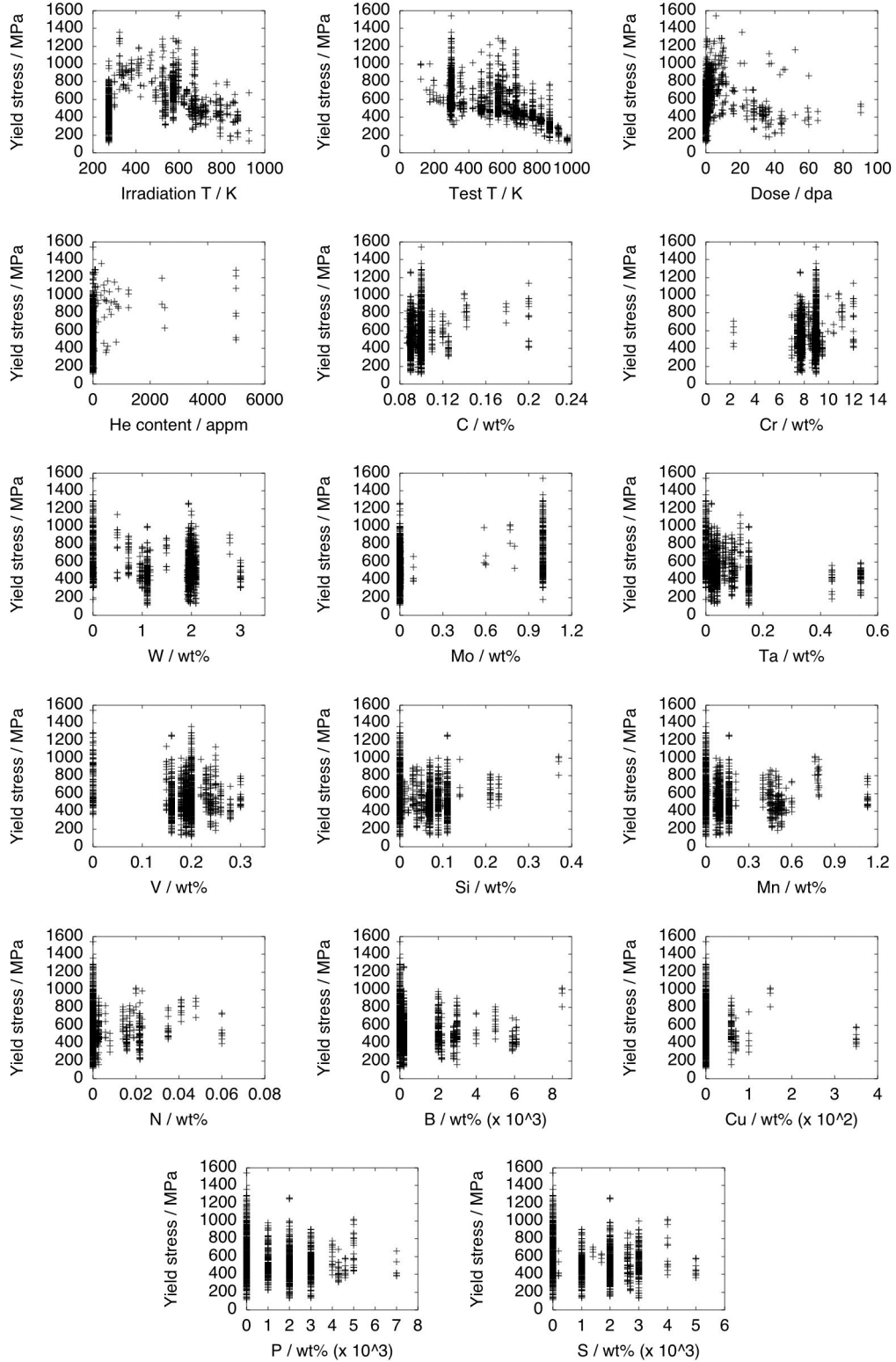


Figure 5.2: Distribution of inputs against σ_y , to illustrate the spread of data.

5.3 Neural network model of irradiation hardening

although this exclusion undoubtedly led to increased noise in the model outputs and, in the case of nickel, misleading predictions (Section 5.3.3.1). By highlighting these difficulties it is hoped that future experiments are better defined with a full reporting of variables known to be useful. Further work includes the addition of heat-treatment information to the database to refine the model.

The yield stress, σ_y was modelled directly, rather than the change caused by irradiation, $\Delta\sigma_y$. σ_y is well characterised in unirradiated materials and so provides a good baseline for the algorithm – $\Delta\sigma_y$ can then be calculated from the model outputs.

As the principles of hardening mechanisms are understood, as described in Section 5.1, an attempt can be made to include aspects of these known physics into the model by using appropriate combinations of input variables. If these functional forms are not useful in explaining the data, they will be effectively ignored by the network. Therefore, in addition to the raw inputs (Table 5.1) the following terms were included:

1. Two Arrhenius-type relations for the temperatures T_{irr} and T_{test} , to take account of any thermally activated processes. Although the processes cannot be simply described by Arrhenius rate expressions, including this term may help the model to capture interactions that involve it. These have the standard form $\exp\left(\frac{-Q}{kT}\right)$, in which Q is an activation energy.
2. The He concentration-to-dpa ratio, to complement the He concentration input, c_{He} , and allow for possible interactions between gas and displacement damage.
3. A term defining saturation in the hardening as the microstructure reaches a steady-state in terms of defect formation and annihilation as is thought to occur under some irradiation conditions. This term has the form $\left(1 - \exp\left(-\frac{Kt}{\alpha}\right)\right)$.

In the saturation term, α is a fitting parameter dependent on the material and irradiation conditions – particularly T_{irr} .

To avoid biasing the model towards any particular combination of parameters such as those described above, the individual variables making up these inputs were also included, so that their direct influence, if any, could also be detected.

Owing to the functional form of the saturation term, it is not possible to define the problem in such a way that α can be inferred by the neural network – an unfortunate limitation of the method. Therefore, multiple values of α were included as separate

5.3 Neural network model of irradiation hardening

Input variable	Min.	Max.	Mean	Standard deviation
Irradiation temperature, T_{irr} , K	273.	925.	401.2	179.3
Test temperature, T_{test} , K	123.	973.	549.5	209.4
Dose, dpa	0.	90.	3.47	10.04
He content, appm	0.	5000.	38.4	359.8
Cold working, %	0.	10.	0.09	0.94
Composition, wt%				
C	0.087	0.2	0.097	0.013
Cr	2.25	12.	8.325	1.027
W	0.	3.	1.485	0.778
Mo	0.	1.	0.16	0.363
Ta	0.	0.54	0.064	0.102
V	0.	0.3	0.182	0.054
Si	0.	0.37	0.055	0.052
Mn	0.	1.13	0.145	0.204
N	0.	0.06	0.0025	0.081
Al	0.	0.054	0.0008	0.037
As	0.	0.005	0.0001	0.0003
B	0.	0.0085	0.0007	0.0013
Bi	0.	0.005	0.0001	0.0003
Ce	0.	0.036	0.0001	0.0022
Co	0.	0.01	0.0002	0.0009
Cu	0.	0.035	0.0006	0.0032
Ge	0.	1.2	0.0139	0.128
Mg	0.	0.01	0.0001	0.0006
Nb	0.	0.16	0.0017	0.011
Ni	0.	2.	0.0576	0.31
O	0.	0.009	0.0002	0.0011
P	0.	0.007	0.0013	0.0014
Pb	0.	0.005	0.0001	0.0003
S	0.	0.005	0.0012	0.0011
Sb	0.	0.003	0.0001	0.0002
Se	0.	0.003	0.0001	0.0002
Sn	0.	0.003	0.0001	0.0002
Te	0.	0.005	0.0001	0.0003
Ti	0.	0.25	0.0099	0.046
Zn	0.	0.005	0.0001	0.0003
Zr	0.	0.059	0.0003	0.0036

Table 5.1: Various inputs in the data set, their ranges, means and standard deviations.

5.3 Neural network model of irradiation hardening

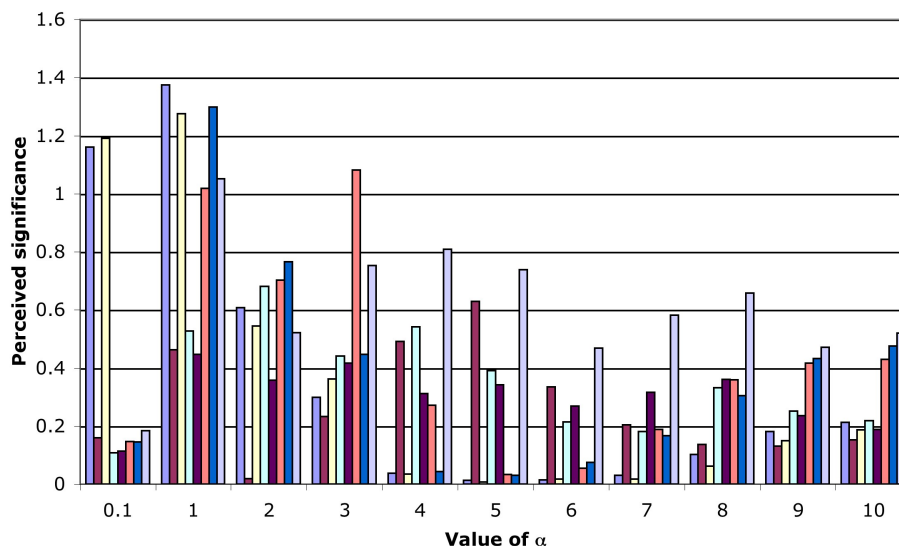


Figure 5.3: Perceived significances for inputs with different values of α . Each bar represents a different model in the committee – there were eight models in the committee in total.

inputs leaving the network to adopt the most suitable value(s). In this case, a set of initial models were trained for 11 values of α between 0.1 and 10 dpa. The significances (equivalent to partial correlation coefficients) inferred by the network for each of these values were then examined (Figure 5.3). The significance is maximum when an input is able to explain a large amount of the variation in the output.

It is striking that low values ($\alpha \sim 1-4$) are generally preferred. This is consistent with there being a strong low-dose/short time-scale influence, and such values are in agreement with those observed by Yamamoto et al. (2003). Although all values could have been included in the final model, it was decided to set $\alpha = 1$ for final model training. It would have been desirable to also incorporate at least one higher value, but models trained with multiple values of α were more complex (more hidden units) and suffered an accompanying increase in uncertainty. This frequently occurs when there are a number of similar inputs and limited data to allow them to be distinguished.

The model target was the natural logarithm of the yield stress, rather than the yield stress itself. This prevented the model from producing non-physical negative estimates of σ_y , and allowed the simplification of some derived inputs – for example, the Ar-

5.3 Neural network model of irradiation hardening

Arrhenius relations could be included as inputs of the form $-\frac{1}{T}$ rather than the exponent (with the $\frac{Q}{k}$ multiplier inferred by the network). This also allowed the model to capture any potential power law dependencies such as the aforementioned \sqrt{Kt} . Modelling $\ln(\sigma_y)$ results in a slight decrease of sensitivity over modelling σ_y directly, but the benefits described more than compensate.

5.3.2 Model training

The data were randomly divided into two equal groups designated the training and test databases, and normalised, as described in Chapter 3.

A total of 120 networks were trained with from 1 to 20 hidden units, and from six different seeds. As the networks became more complex (and hence more flexible) the perceived noise on the training data decreased as expected (Figure 5.4(a)).

However, as shown in Figure 5.4(b) the ability of the models to generalise to the test data does not decrease monotonically and is minimum in the range of ~ 4 hidden units. Figure 5.4(c) shows that the log predictive error (LPE) also peaks at about 4-6 hidden units. Also, as anticipated, more accurate results were obtained by building a committee. In this case, the optimum committee was found to have five members (Figure 5.4(d)). The committee members ranged from 4 to 6 hidden units. The committee average perceived noise in the dataset was 0.049, with a standard deviation of 0.002.

The network perceived significances, σ_w , for each input are shown for each sub-model in the committee in Figure 5.5(a) (for composition) and Figure 5.5(b) (for irradiation and test parameters).

Figure 5.5(a) shows that most of the compositional variables were found to be insignificant. However, this is not particularly surprising, even for alloying elements that are known to potentially influence σ_y but that in the database either: (a) have a narrow range (*e.g.* C and V); (b) have only one or a few values, some of which may be associated with potentially confounding variables such as different heat treatments (*e.g.* Cr, Si, Mn, B, Mo, W, Ni, P and Nb); or (c) are alloying or trace impurity elements with missing values set to zero. The same can be said for cold work. However, as discussed below, the various alloys did have different predicted σ_y as well as $\Delta\sigma_y$ dependencies on both dpa and T_{irr} .

5.3 Neural network model of irradiation hardening

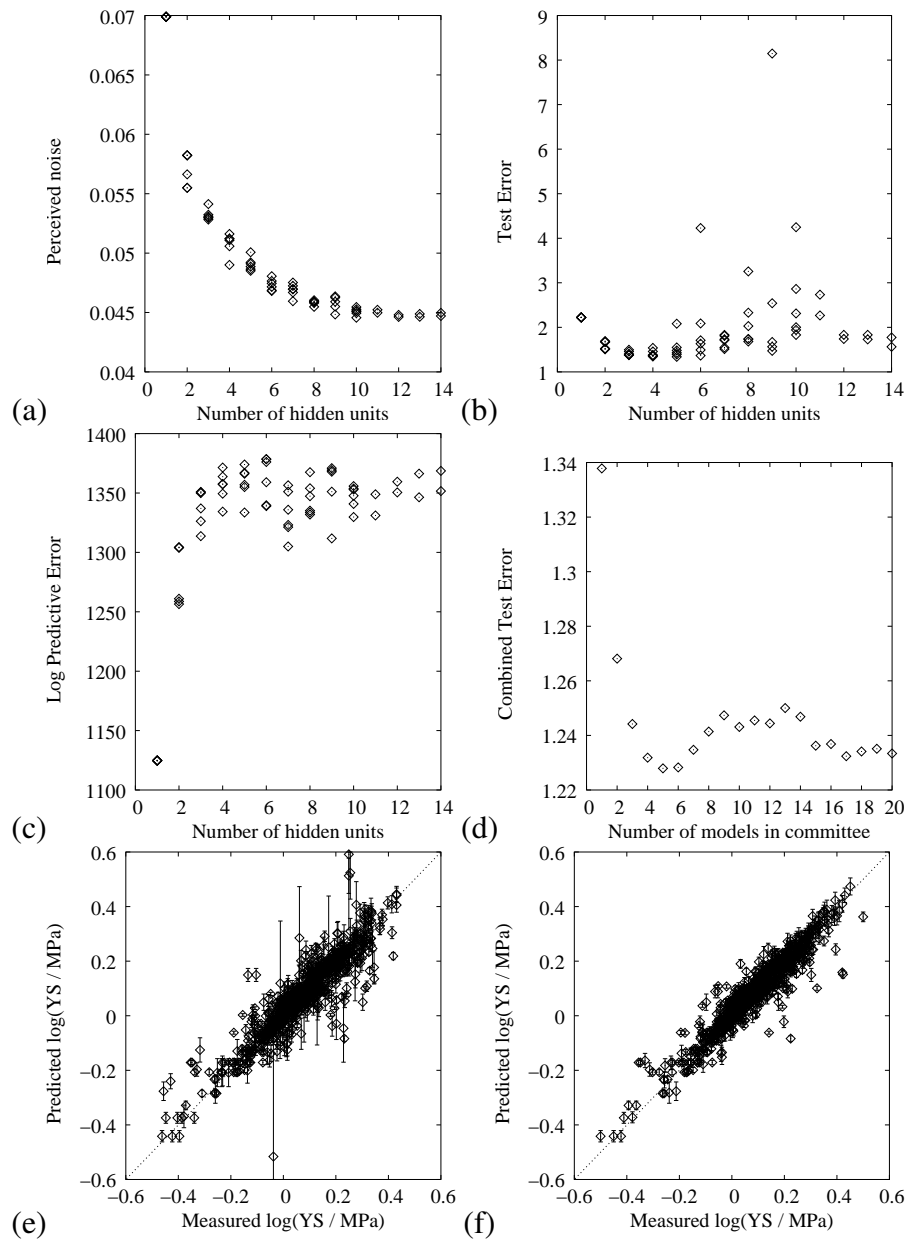


Figure 5.4: Model training reports: (a) perceived level of noise for the training data, (b) the error between the models and the test data, (c) log predictive error for increasing model complexity, (d) combined test error for different sizes of committee, (e) best single model performance on training data and (f) test data – in this case, the data are normalised.

5.3 Neural network model of irradiation hardening

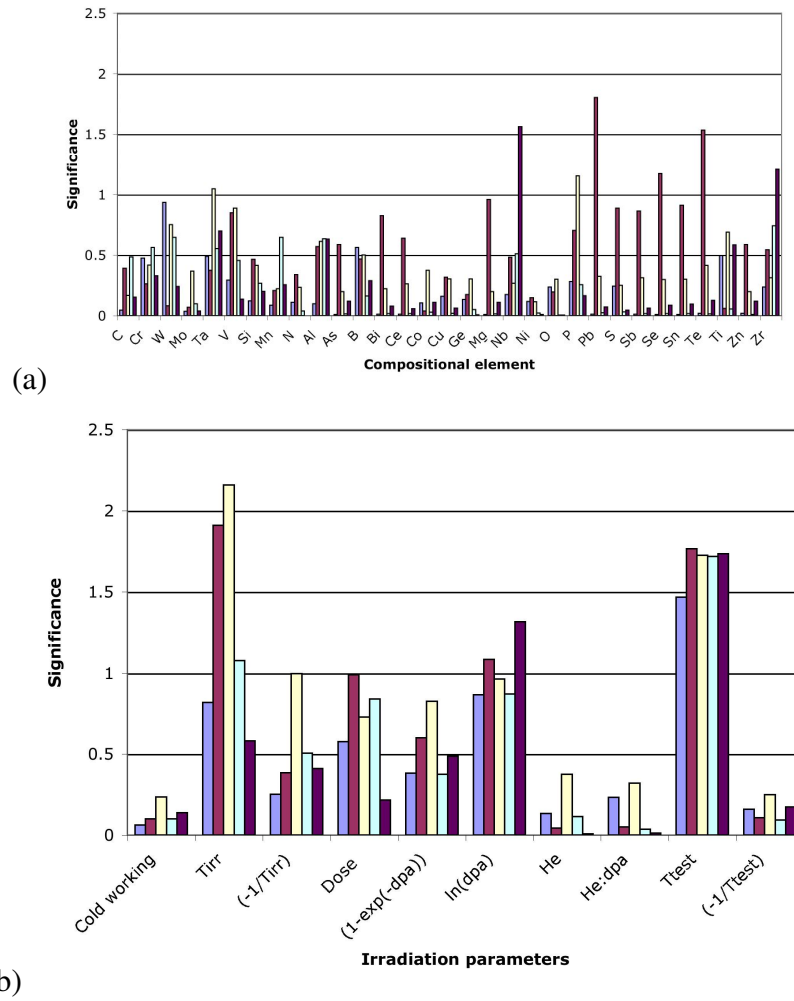


Figure 5.5: Perceived significances σ_w for the committee members of the model for (a) alloying elements and (b) irradiation and tensile test parameters.

5.3 Neural network model of irradiation hardening

T_{irr} , T_{test} and the three dose-related variables were significant, particularly in combination. It is well known that test temperature has a strong effect on tensile tests, and it is to be expected that irradiation temperature will also have a powerful effect as a heat treatment in its own right – this is why the time elapsed during irradiation is potentially an important parameter. Notably, in this dataset, neither He nor He/dpa were found to play a significant role in determining σ_y . This may be because there were only a small number of high-He data, and any effect was below the noise level, or it may be that any He effect is directly related to the displacement damage level, and therefore is incorporated into the dpa input.

Predictions of the final trained committee model on the input dataset are shown in Figure 5.6. Given the sparseness of the dataset and the assumptions made for the inputs, there are relatively few poorly estimated points, and those are generally accompanied by a large uncertainty. There is a clear improvement over the best single model, shown in Figure 5.4(e) and (f). For the final committee model, the standard deviation of the predicted versus measured σ_y was 95 MPa. There were a total of 42 estimated points more than three standard deviations away from their measured values (from 1811 data points).

5.3.3 Model predictions

5.3.3.1 Predictions for existing steels

Due to the complexities of a neural-network model, the best way to assess its properties is through “virtual experiments” – using it to make predictions across a wide range of input conditions – rather than by examination of the weights or structure. As an example, Figure 5.7 shows that the model describes well the non-linear $\sigma_y(T_{\text{test}})$ of Eurofer97.

The input compositions for all the predictions made below are shown in Table 5.2. Predictions were not made for all alloys in the database.

Test and irradiation temperature

The dashed line in Figure 5.8 shows that the model predicts a peak in the T_{irr} ($= T_{\text{test}}$) dependence of $\Delta\sigma_y$ for Eurofer97. The corresponding predictions based on direct

5.3 Neural network model of irradiation hardening

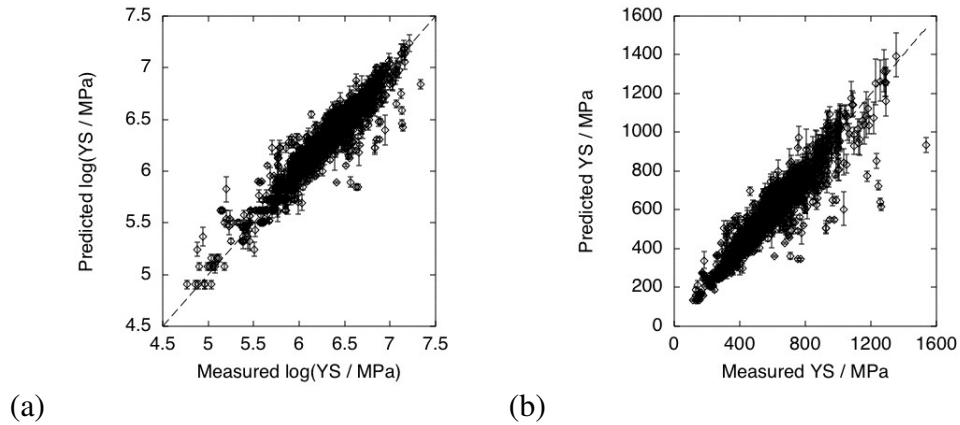


Figure 5.6: Performances of the final committee model on the whole database. (a) The direct output $\ln(\sigma_y)$ and (b) converted to σ_y .

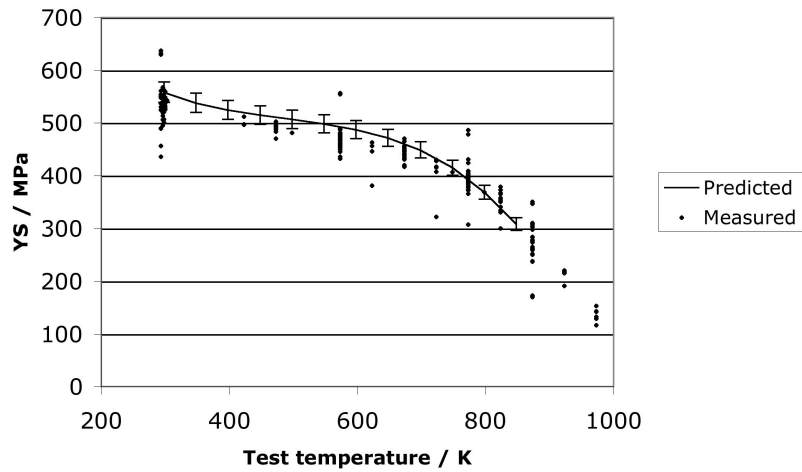


Figure 5.7: Model predictions for the tensile test behaviour of unirradiated Eurofer97 at different test temperatures, plotted with measured data. The bars represent $\pm 1\sigma$ modelling uncertainty.

5.3 Neural network model of irradiation hardening

Element	Alloy					
	F82H	Eurofer97	T91	9Cr-1WVTa	9Cr-1MoVNB-2W	2.5Cr-1.4WV
C	0.009	0.1	0.01	0.01	0.01	0.01
Cr	7.7	9.	9.	9.	9.	2.5
W	1.94	1.1	0.	1.	0.	1.4
Mo	0.	0.	1.	0.	1.	0.
Ta	0.02	0.15	0.	0.1	0.	0.2
V	0.16	0.2	0.2	0.2	0.2	0.2
Si	0.11	0.	0.	0.	0.	0.
Mn	0.16	0.	0.	0.	0.	0.
N	0.	0.	0.	0.	0.	0.
Al	0.	0.	0.	0.	0.	0.
As	0.	0.	0.	0.	0.	0.
B	0.0002	0.	0.	0.	0.	0.
Bi	0.	0.	0.	0.	0.	0.
Ce	0.	0.	0.	0.	0.	0.
Co	0.	0.	0.	0.	0.	0.
Cu	0.	0.	0.	0.	0.	0.
Ge	0.	0.	0.	0.	0.	0.
Mg	0.	0.	0.	0.	0.	0.
Nb	0.	0.	0.005	0.	0.006	0.
Ni	0.	0.	0.	0.	0.	0.
O	0.	0.	0.	0.	0.	0.
P	0.002	0.	0.	0.	0.	0.
Pb	0.	0.	0.	0.	0.	0.
S	0.002	0.	0.	0.	0.	0.
Sb	0.	0.	0.	0.	0.	0.
Se	0.	0.	0.	0.	0.	0.
Sn	0.	0.	0.	0.	0.	0.
Te	0.	0.	0.	0.	0.	0.
Ti	0.	0.	0.	0.	0.	0.
Zn	0.	0.	0.	0.	0.	0.
Zr	0.	0.	0.	0.	0.	0.

Table 5.2: Chemical composition inputs (in wt%) for model predictions.

5.3 Neural network model of irradiation hardening

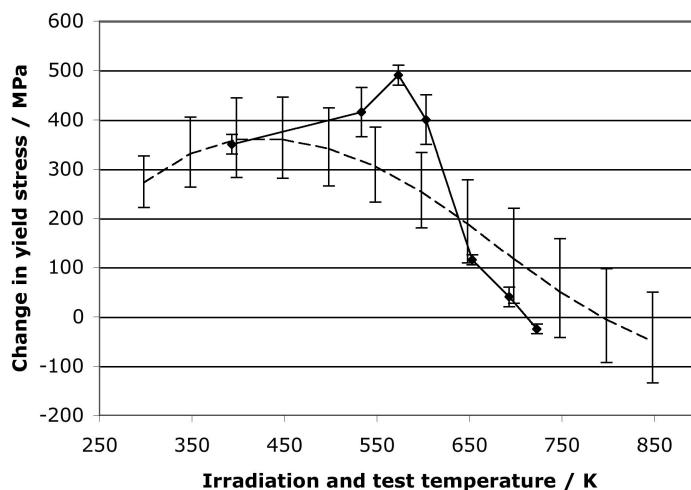


Figure 5.8: Model predictions (dashed line) for the yield stress of Eurofer97 irradiated to 3 dpa at various temperatures, compared with saturation hardening predictions from Yamamoto et al. (2003) (\blacklozenge and solid line). A damage level of 3 dpa was chosen for the predictions as it generally corresponds with the onset of hardening in Yamamoto's model.

data fits by Yamamoto et al. (2003) are shown by the solid line. The agreement is quite good below $\sim 350^\circ\text{C}$ but the neural network nominal prediction deviates from the direct data fits at higher T_{irr} , where negligible $\Delta\sigma_y$ is observed. However, the direct fit points generally fall within the estimated uncertainty limits of the neural network model. Note that while the direct data fit does not predict a peak in hardening at 3 dpa over the temperature range covered, it does predict one for the maximum $\Delta\sigma_y$ beyond a T_{irr} -dependent saturation dose. It can be postulated that such a hardening peak is physically consistent with the thermal mobility and recombination of defects. At low temperatures the radiation-induced defects are not mobile enough to form extended structures such as dislocation loops, and cascade overlap quickly leads to a saturated damage state. At higher temperatures, the extended structures tend to dissolve and the defects annihilate at fixed microstructural sinks. In the intermediate temperature regime, a hardening peak is therefore not unexpected.

Figure 5.9 shows σ_y versus $T_{\text{irr}} = T_{\text{test}}$ neural network predictions for F82H in the irradiated and unirradiated conditions, compared to experimental data. The predictions

5.3 Neural network model of irradiation hardening

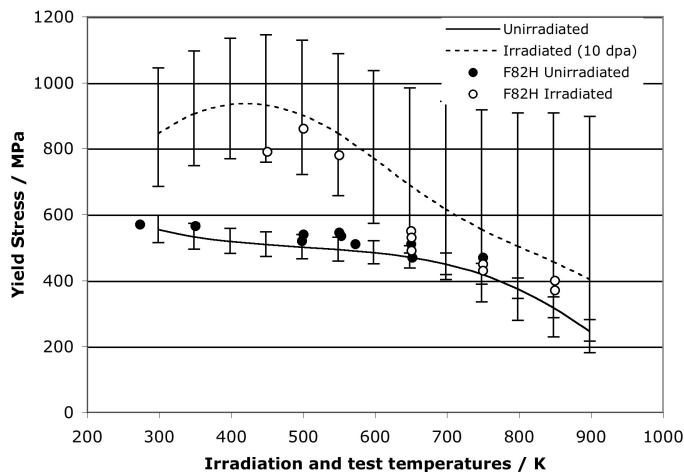


Figure 5.9: Model predictions for the behaviour of modified F82H, compared to measurements reported by Hishinuma et al. (1998). The model predictions are for 10 dpa, $T_{\text{irr}} = T_{\text{test}}$. The doses in Hishinuma vary from 3 to 34 dpa.

tend to fall only slightly below the unirradiated σ_y reported by Hishinuma et al. (1998) over the entire range of T_{test} , with relatively small uncertainties. The nominal predicted σ_y for irradiations to 10 dpa are somewhat higher than Hishinuma's corresponding data points, but within the uncertainty limits.

Irradiation dose

It is well known that irradiation causes rapid hardening of steels even at low doses, and this low-dose effect is reflected in the model. The degree to which hardening will saturate at high doses (as postulated by Makin and Minter (1960)) is unknown. Indeed, as observed in some cases, at higher T_{irr} the σ_y appears to reach a maximum and then decrease (Kohyama et al., 1996). The model shows a range of behaviours, depending on the alloy (Figure 5.10). Some alloys show a peak followed by a decrease of σ_y (F82H, for example) while others continue to increase at high dose (T91). However, it is not known if these differences are real or an artefact of the database distribution and uncertainties. On average, the ANN-predicted σ_y saturate at a substantial $\Delta\sigma_y$ that are higher than that predicted by the direct data fit. It is worth noting, though, that the irradiation parameters for these predictions lie significantly outside the training database

5.3 Neural network model of irradiation hardening

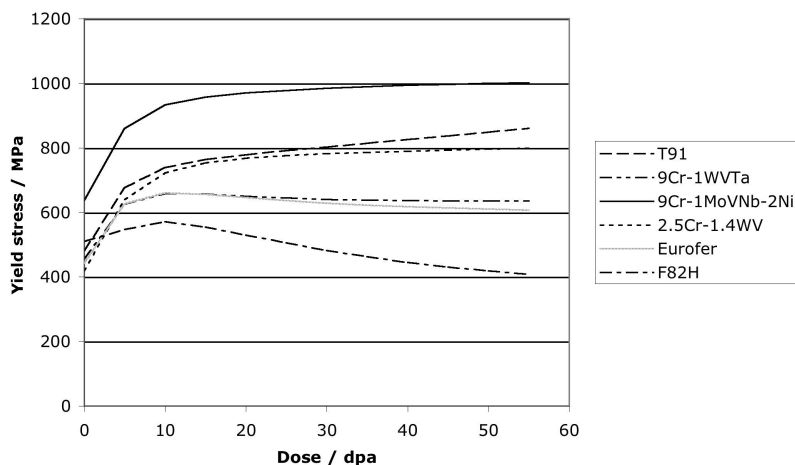


Figure 5.10: Comparison of irradiation hardening of various steels showing both saturation and high-dose recovery behaviour. In all cases $T_{\text{irr}} = T_{\text{test}} = 400^{\circ}\text{C}$. The uncertainty bars have been omitted for clarity.

and so are accompanied by large uncertainties (on the order of hundreds of MPa). The observed trends, however, are reasonable, but only high-dose data generated in future experiments will help validate and refine the model.

Chemical influence

The presence of nickel appears to increase the yield stress, both before and after irradiation (Figures 5.10 and 5.11). This influence was observed and described by Klueh and Vitek (1987). However, closer examination of the original data showed that these alloys were subjected to a different heat treatment than others in the dataset, and this is the most likely cause of this effect.

Into the fusion regime

Figure 5.12 shows the neural network predictions of σ_y and corresponding uncertainty estimates over a range of temperatures (300-900 K) and damage levels (0-200 dpa). The regions well outside the training database have uncertainties that are comparable to or larger than σ_y itself. These uncertainties provide an indication that predictions in

5.3 Neural network model of irradiation hardening

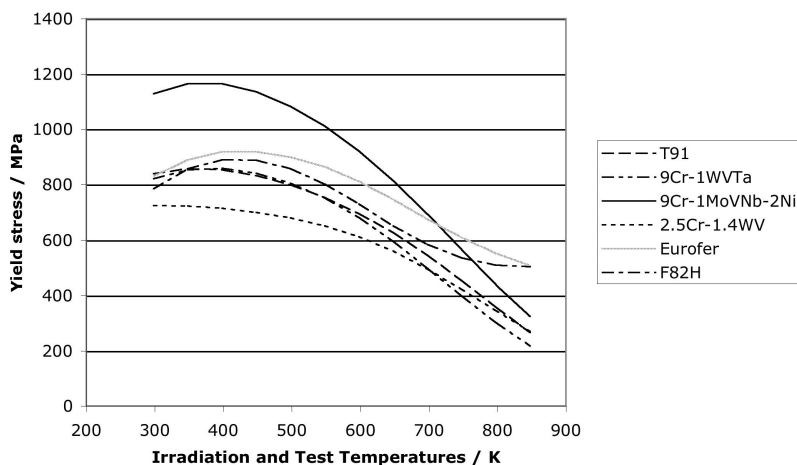


Figure 5.11: Comparison between different alloys irradiated to 2 dpa at different temperatures. In all cases $T_{\text{irr}} = T_{\text{test}}$. The uncertainty bars have been omitted for clarity.

these areas should be regarded sceptically, and that experiments in these areas would provide valuable information.

In particular, at the relevant temperatures (750-900 K), data are required for damage levels greater than 100 dpa to reduce the uncertainties for fusion-relevant predictions for these materials. Additionally, of course, fusion-spectrum irradiation experiments are required to validate this model for such irradiation energies. Further validation would come from experiments carried out on the optimised composition below, to compare the performance of this material with the performance of current candidate materials.

5.3.3.2 Conclusions

Ideally, and certainly in the long run, mechanical property predictions will be based on hierarchical models of microstructural evolution linked to structure property relations in a way that will incorporate the effects of all important variables and their interactions, as well as incorporating all known physics and underlying mechanisms. In the meantime, however, less rigorous techniques are required to produce meaningful quantitative predictions for engineering purposes.

5.3 Neural network model of irradiation hardening

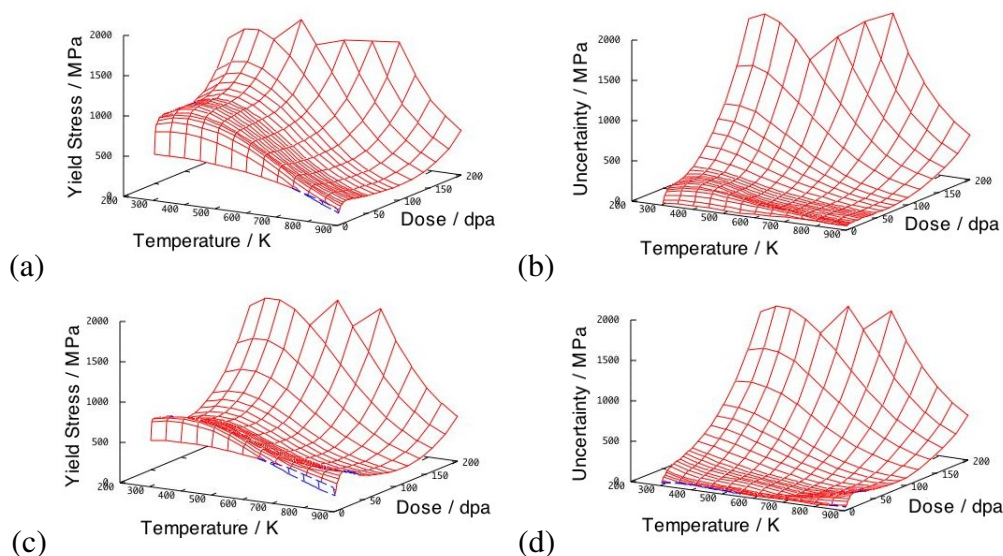


Figure 5.12: Hardening predictions (and modelling uncertainties) for Eurofer97 ((a) and (b)) and F82H ((c) and (d)), as a function of temperature ($T_{\text{irr}} = T_{\text{test}}$) and damage level.

Direct non-linear regression fits to the data using simple phenomenological, but physically motivated models are useful. For example, the fits by Yamamoto et al. (2003) provide a good representation of the existing database. However, such models often contain assumptions that are sometimes hidden or unrecognised. In Yamamoto's case, high-dose saturation is assumed and extrapolated from low-dose trends even in the absence of high-dose data.

While uncertainties in such extrapolations can be estimated, the effects of the various assumptions are not easy to quantify in a useful way. In principle, the neural network approach avoids the need for any assumptions about the form of the fitting equation, and provides error estimates of extrapolations. However, this approach has the corollary disadvantage that it frequently does not allow easy ways to include known physics.

It is clear, however, that the flexibility and power of the neural network modelling approach can be fruitfully applied to the analysis of irradiation damage in steels. It provides a means of making wide-ranging quantitative predictions and provides a warning of when those predictions may not be trustworthy.

5.3 Neural network model of irradiation hardening

For the near future, the use of complementary approaches will be needed, and perhaps their most important contribution will be to highlight the most significant gaps in our knowledge to help guide future experiments.

The model and data presented in this chapter and instructions for its use can be found through the Materials Algorithm Project (MAP) website, at <http://www.msm.cam.ac.uk/map/mapmain.html>.

5.3.4 Optimisation of steel composition

The genetic algorithm procedure described in Chapter 4 was carried out on the ANN model described above. The target was to identify steel compositions with similar properties, post-irradiation, to those of unirradiated candidate alloys. In this case, three irradiation temperatures (600, 700 and 800 K) and two damage levels (5 and 20 dpa) were explored. Tensile test temperatures were equal to irradiation temperatures. The concentrations of the major RAFM alloying elements (C, W, Mo, Ta, V, Si, and Mn) were allowed to vary. The concentrations of all other elements was fixed at zero, with the exception of Cr which was fixed at 9 wt%, as 9Cr alloys generally exhibit the greatest resistance to irradiation embrittlement (Chapter 6), and also good creep resistance (Abe, 1994). The decision was therefore made to try to optimise a 9Cr Eurofer97-type alloy. This requirement to artificially limit the scope of the algorithm to take account of other material properties is a weakness in the approach, and the intention is to rewrite the software to allow simultaneous optimisation of multiple properties.

The target post-irradiation yield stress values were 650 MPa at 600 K, 600 MPa at 700 K, and 350 MPa at 800 K. This corresponds to modest irradiation hardening at the lower two temperatures and none (or very little) at 800 K. By contrast, the unirradiated yield stresses for Eurofer97 are 480 MPa at 600 K, 450 MPa at 700 K, and 350 MPa at 800 K.

The conditions, targets, and results are summarised in Tables 5.3 and 5.4.

It is interesting that the optimised compositional values for Mo, Ta, V and Si are in the centre of the training database ranges – although this may not be true of the 9Cr subset of data. This may be due to these elements having only minor effects on the irradiation hardening – in this dataset – although the addition of small amounts of

5.3 Neural network model of irradiation hardening

Input	Eurofer97	Values		
Irradiation Temperature /K	--	600.	700.	800.
C	0.1	0.13	0.11	0.08
Cr	9.	9.0	9.0	9.0
W	1.1	2.9	2.2	2.0
Mo	0.	0.50	0.50	0.50
Ta	0.15	0.27	0.27	0.27
V	0.2	0.15	0.15	0.15
Si	0.	0.185	0.185	0.185
Mn	0.	0.48	0.25	0.25
Damage /dpa	--	5.	5.	5.
Target /MPa	--	650.	600.	350.
Prediction /MPa	--	691.	617.	401.
Uncertainty /MPa	--	163.	144.	164.

Table 5.3: Genetic algorithm best results for irradiation to 5 dpa under various conditions, compared to Eurofer97 (chemical compositions in wt%).

Input	Eurofer97	Values		
Irradiation Temperature /K	--	600.	700.	800.
C	0.1	0.14	0.14	0.07
Cr	9.	9.0	9.0	9.0
W	1.1	2.46	1.8	1.9
Mo	0.	0.50	0.50	0.50
Ta	0.15	0.27	0.27	0.27
V	0.2	0.15	0.15	0.15
Si	0.	0.185	0.185	0.185
Mn	0.	0.23	0.25	0.1
Damage /dpa	--	20.	20.	20.
Target /MPa	--	650.	600.	350.
Prediction /MPa	--	695.	607.	432.
Uncertainty /MPa	--	224.	198.	197.

Table 5.4: Genetic algorithm best results for irradiation to 20 dpa under various conditions, compared to Eurofer97 (chemical compositions in wt%).

5.3 Neural network model of irradiation hardening

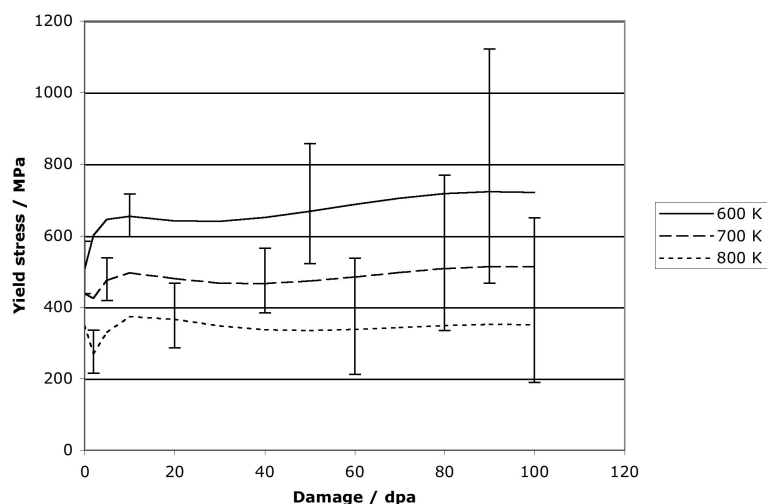


Figure 5.13: Hardening predictions (and modelling uncertainties) for the GA optimised steel composition for three different irradiation temperatures ($T_{\text{irr}} = T_{\text{test}}$).

Ta (0.07 wt%) to a 9Cr-2WV steel reduced the irradiation hardening slightly (Klueh, 1991). At any rate, Mo levels need to be kept very low to avoid the formation of long-lived waste (Butterworth and Giancarli, 1988), and Si should be avoided as it promotes the formation of Laves phase (Abe et al., 1994).

Increasing W content can cause embrittlement of the steel (again through the formation of Laves phase), but this is tempered by the inclusion of V and Ta (Abe, 1994).

5.3.4.1 Predictions for optimised steel

A steel with the composition 0.13C-9Cr-2W-0.1Ta-0.15V-0.25Mn is suggested by the results above. This is a similar composition to the high-W LA13Ta and JLF1 alloys described in Alamo et al. (1998), although the heat treatments of those two alloys differ and this is not accounted for in the model.

Figure 5.13 shows predictions for irradiation hardening of a steel of this composition at three irradiation (and test) temperatures. The predictions indicate a steel which undergoes only moderate irradiation hardening, which rapidly saturates. The modelling uncertainties are large at high doses, but this is because the composition represents a novel proposal, and because of limited high-dose experimental data.

Of course, when designing a steel there are other concerns than simply the value of one material property. As well as solutions not necessarily taking account of potential metallurgical pitfalls (such as the stabilisation of unwanted phases), the weakness in this optimisation method, as it currently stands, is that it does not permit model inputs to be optimised for multiple targets. That is, a steel can be identified for a given yield stress at a given temperature, but not one that is perhaps less good at a particular temperature but generally better across a range of temperatures. Additionally, it would be advantageous to optimise for a range of material parameters – combining this $\Delta\sigma_y$ model with the embrittlement model described in Chapter 6. However, it is clear that this modelling method has a lot to contribute towards the engineering of a future fusion power plant.

5.4 The need for more data

One of the primary conclusions from this work is that the current database is insufficient to provide the desired refinement of the model that would markedly reduce the uncertainty in predictions of irradiated yield stresses. The construction of an improved database would be helped by future experiments providing sufficient detail of potentially important variables, such as dose rate, irradiation energy spectrum, duration of irradiation, and so forth, and by providing estimates of error in key variables such as irradiation temperature.

Ongoing work includes the addition of heat-treatment information to the database and the retraining of the model to include this data. Further work includes an extension of the genetic algorithm code to include multiple selection criteria, so that this optimisation method can be applied to complex problems where the materials properties across a range of input conditions are of interest.

Chapter 6

Irradiation embrittlement

In a real structure, such as a fusion reactor, it must be assumed that sub-critical cracks are present and therefore defect-tolerant structural materials must be used. Embrittlement of structural materials, as a result of exposure to a corrosive environment, the presence of hydrogen, irradiation, *etc.* is therefore a major concern. This embrittlement is detected in Charpy V-notch tests as an increase in the ductile-to-brittle transition temperature (DBTT) and a decrease in the upper shelf energy (USE) (Figure 6.1) and, in tensile specimens, as a reduction in fracture strain.

At temperatures above the DBTT, failure occurs by ductile tearing and microvoid coalescence in the vicinity of the growing crack tip. Below the DBTT, fast fracture occurs due to unstable propagation of a crack by locally brittle cleavage. In some cases, intergranular fracture can also occur, but is rare in Charpy tests on RAFM steels (Odette et al., 2003).

When this effect occurs in response to radiation exposure, it is referred to as *irradiation embrittlement*. At temperatures below $\sim 400^\circ\text{C}$, the dominant mechanism is generally thought to be *hardening embrittlement*, described below. The persistence of embrittlement to higher temperatures than those at which hardening occurs demonstrates the presence of additional mechanisms (*non-hardening embrittlement*).

It should be noted that although Charpy impact data are a useful tool for exploring the effects of radiation on fracture behaviour, and serve as a method for rating the relative resistances of different steels to irradiation damage, they cannot be used directly for engineering design purposes as they do not measure the fracture toughness of a material, K_{Ic} . Currently, there are very limited fracture toughness data available for

6.1 Mechanisms of irradiation embrittlement

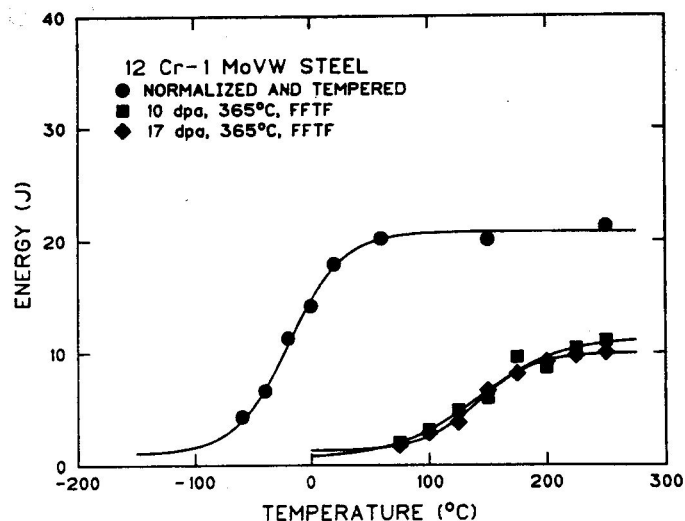


Figure 6.1: Charpy curves for half-size specimens of 12Cr-1MoVW steel before and after irradiation to 10 and 17 dpa at 365°C in the Fast Flux Test Facility (FFTF) (Klueh and Harris, 2001, p. 140).

RAFM steels. The Charpy test is easier to conduct and the specimens are simpler to miniaturise for use in irradiation experiments – a particular concern for IFMIF, with its limited irradiation volume (Spätig et al., 2005). This miniaturisation is not without its drawbacks, however, as the values obtained for USE and DBTT during such a test cannot easily be compared for different sizes of specimen (Abe and Kayano, 1996). The fusion materials community has generally settled on specimens that are one third the size of the usual Charpy specimens (*i.e.* they have a cross-section of 3.3 mm by 3.3 mm), but there is, as yet, no definitive agreed standard (Kurishita et al., 2004; Möslang, 2005), and concern has been expressed that sub-size specimens might underestimate the potential of martensitic steels to experience severe irradiation embrittlement (Yamamoto et al., 2003).

6.1 Mechanisms of irradiation embrittlement

Hardening embrittlement of a material under irradiation is related to the irradiation hardening described in Chapter 5. Hardening causes an increase in the flow stress of

6.1 Mechanisms of irradiation embrittlement

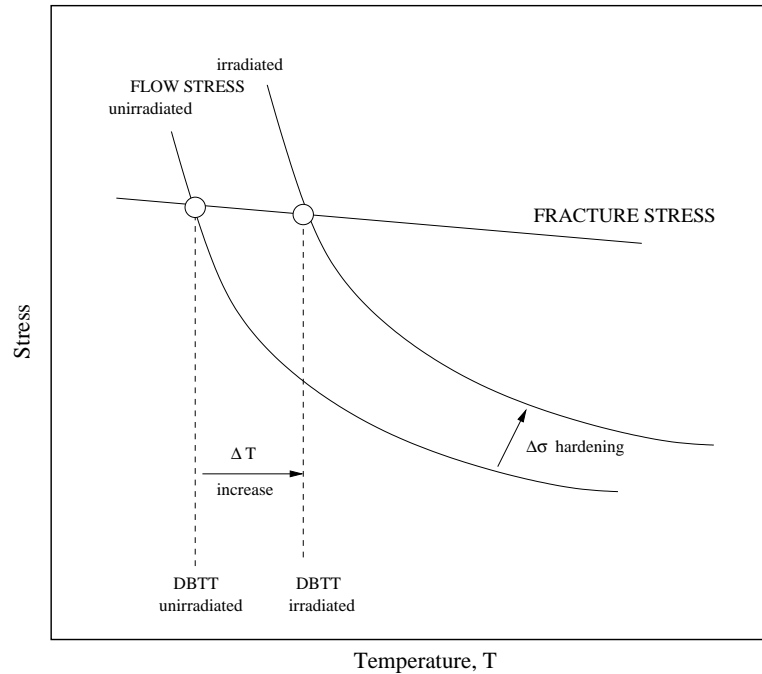


Figure 6.2: Schematic diagram illustrating how irradiation hardening results in a change in the ductile-to-brittle transition temperature.

a material. If it is assumed that the fracture stress is only weakly affected by radiation and that the intersection of the fracture stress curve and the flow stress curve defines the ductile-to-brittle transition temperature, a shift in flow stress results in a corresponding shift in DBTT, as shown in Figure 6.2.

Figure 6.2 also illustrates how the oft-quoted relation $\Delta\text{DBTT} = a\Delta\sigma_y$ applies, as in this construction the shift in DBTT is directly related to that in the yield stress. However, the parameter a varies widely (from ~ 0.33 to ~ 0.7) from material to material and is also dependent on irradiation conditions (Yamamoto et al., 2003). As hardening saturates, so does embrittlement (Murakami et al., 2000).

Irradiation damage also has an effect on the strain-hardening exponent, n . A change in n affects the volume of material which can deform ahead of a growing crack tip. To some extent, if the radiation-induced Δn is negative, this can counteract the adverse hardening effect, resulting in a lower ΔDBTT . These effects have been modelled using finite element (FE) approaches and are reasonably well understood. However, irradiation can also result in localisation of flow. Localisation of deformation in slip

bands is not well understood, but appears only to play a secondary role in cleavage fracture (Odette et al., 2003).

On a microstructural scale, cleavage occurs by the propagation of microcracks starting in brittle particles (such as carbides) that are exposed to high stresses near the tip of a blunting crack. Much of the time, these microcracks arrest on reaching the tougher ferritic matrix surrounding the particle. Under critical conditions, however, the microcrack can continue into the matrix and combine with other microcracks, allowing the crack to undergo fast, unstable growth (Ritchie et al., 1973).

Microstructural changes in a steel that increase the probability of microcracking, and hence cleavage fracture, include precipitation (*e.g.* Laves phase) or coarsening of brittle particles (*e.g.* carbides); segregation of impurity elements known to have an embrittling effect (*e.g.* P) to grain boundaries and dissolved hydrogen. Non-hardening embrittlement can occur under thermal aging in the absence of irradiation, but irradiation displacement damage can dramatically enhance it. For example, radiation-enhanced diffusion can accelerate segregation of impurities or precipitation of brittle phases.

In addition, the formation of small, high-pressure bubbles of He formed in the material under irradiation is postulated to affect fracture properties. In the worst case, these bubbles accumulate at grain boundaries and cause intergranular fracture and unacceptably large DBTT shifts. However, there is a shortage of experimental data on both helium embrittlement effects in combination with irradiation, and non-hardening irradiation embrittlement generally (Odette et al., 2003).

6.2 Previous models

One of the most common treatments of embrittlement is the master curve (MC) approach, which assumes that there is a universal temperature-toughness curve shape (or small family of shapes) characterising cleavage fracture, that can be indexed by a reference temperature (T_0) and toughness. Embrittlement can then be regarded as a shifting of this curve with respect to temperature (ΔT_0). For irradiation specimens, this shift has been measured and modelled, but the master curve does not represent the data well, with a high degree of scatter (Odette et al., 2004). In addition, T_0 and ΔT_0 must be

6.3 Neural network models of Charpy fracture properties

experimentally determined for a material – the method does not allow straightforward prediction of the properties of new materials.

This high degree of scatter with respect to empirical models is also noted by Yamamoto et al. (2003). The scatter could be due to experimental noise, or to uncontrolled factors in the models for calculating ΔT_0 . A description of such a model, based on irradiation hardening, is given by Odette et al. (2002).

Rieth et al. (1998), by contrast, attempted to link embrittlement directly to helium content by correlating boron content to the shift in DBTT during irradiation. This work, although promising, is still in its early stages.

A comprehensive review of irradiation embrittlement mechanisms and multiscale modelling approaches can be found in Odette et al. (2003).

6.3 Neural network models of Charpy fracture properties

These models use the Bayesian neural network structure described in Chapter 3.

6.3.1 Fracture database

A database of the fracture properties of RAFM steels was compiled from the published literature by Yamamoto and co-workers. The full list of references used in the compilation is given in Yamamoto et al. (2003).

The database included a wide range of RAFM steels (8-12Cr) as well as several 2.25Cr bainitic steels and some iron. In total, there were 461 datapoints available for modelling ΔDBTT and 445 datapoints for modelling ΔUSE . The datasets essentially overlapped, although there were some gaps – leading to the different population in each set. Displacement damage levels ranged from 0-100 dpa, within a range of irradiation temperatures from 60-550°C. Figure 6.3 illustrates the range of the input variables against ΔDBTT , and Figure 6.4 illustrates the range of the input variables against ΔUSE .

The input variables are listed in Tables 6.1 (ΔDBTT model) and 6.2 (ΔUSE model), and include most of the parameters thought to influence the fracture properties of steel: chemical composition and cold-working; pre-irradiation heat treatment information;

6.3 Neural network models of Charpy fracture properties

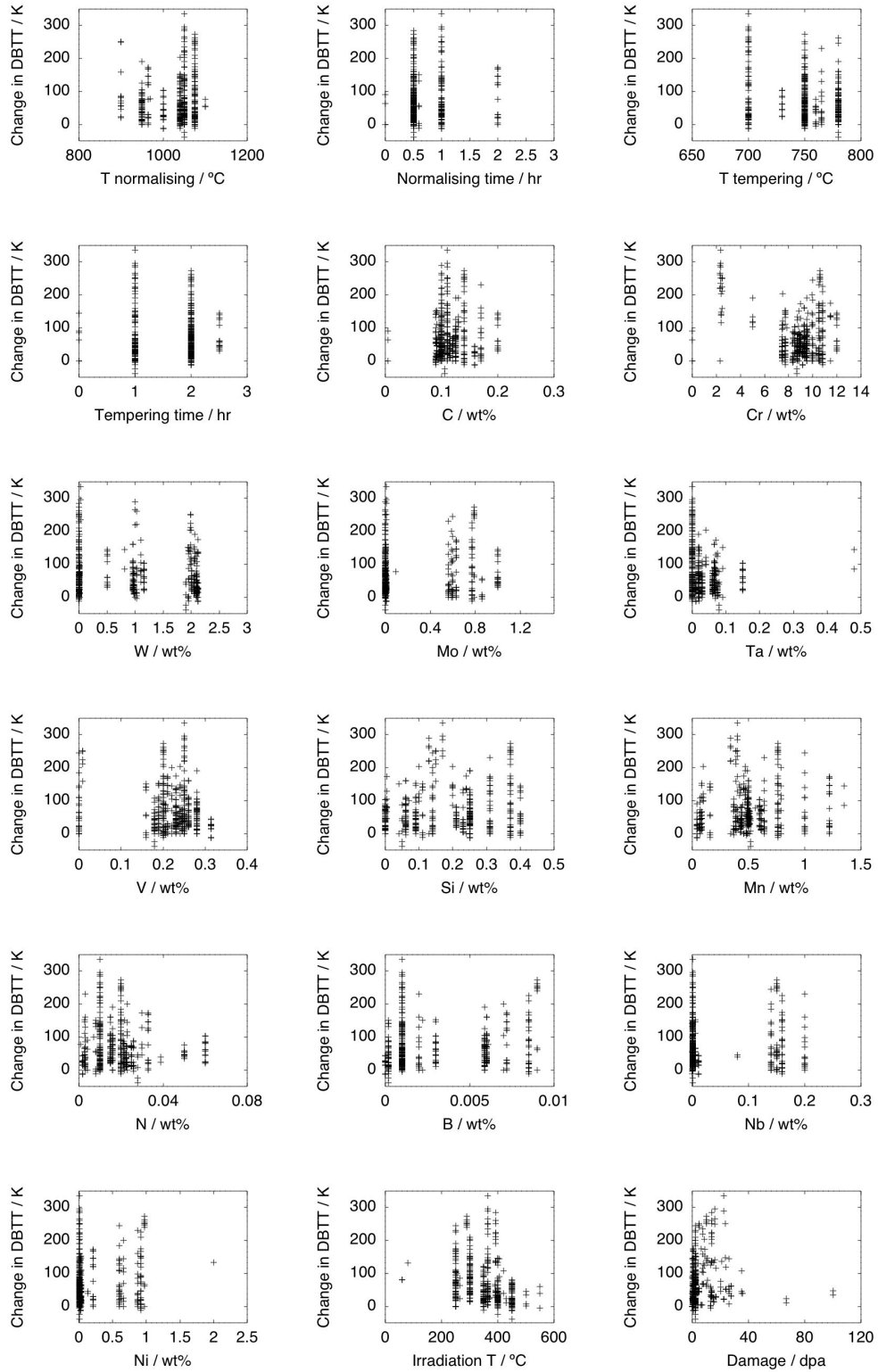


Figure 6.3: Distribution of selected database variables against Δ DBTT.

6.3 Neural network models of Charpy fracture properties

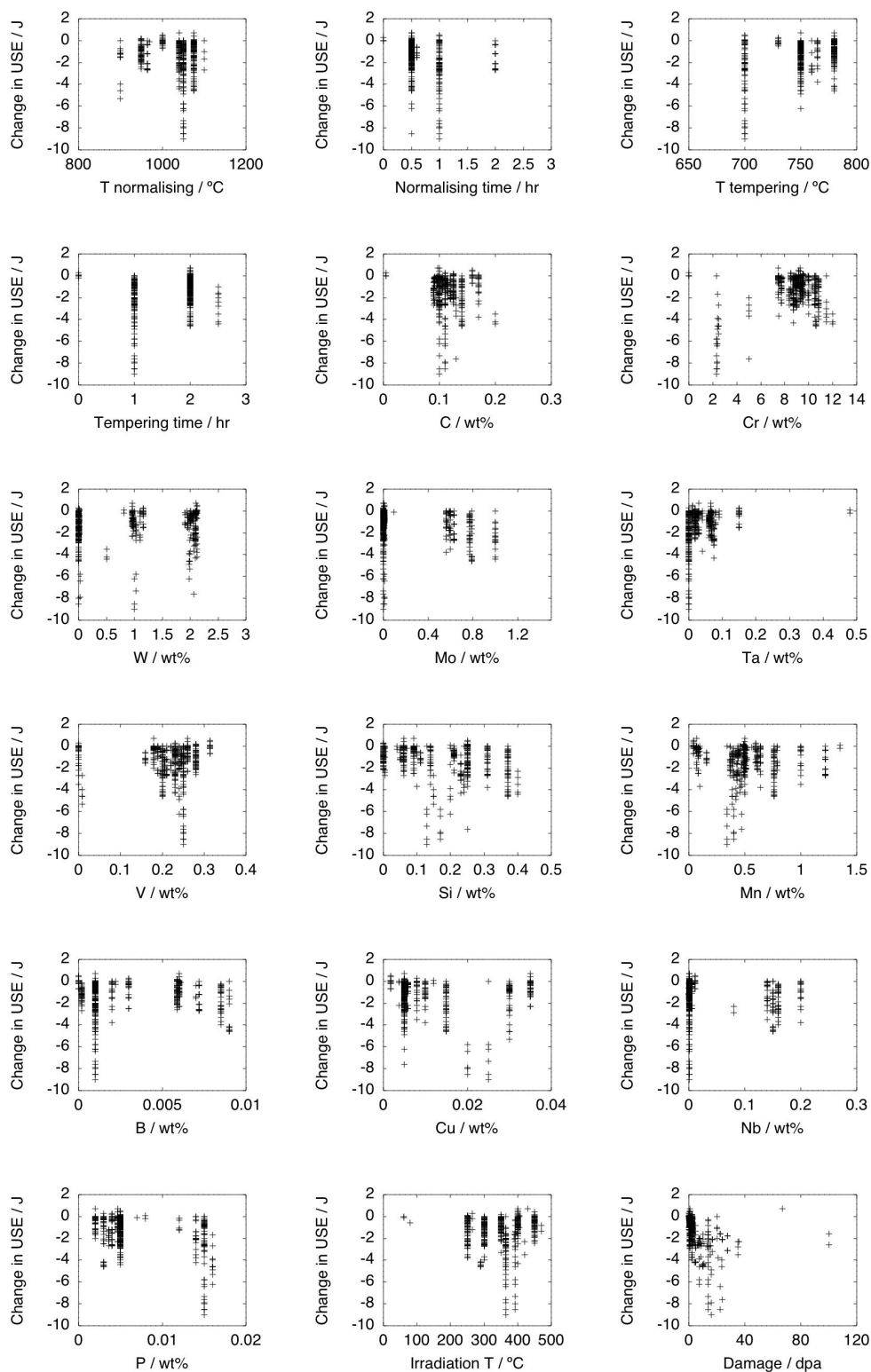


Figure 6.4: Distribution of selected database variables against ΔUSE .

6.3 Neural network models of Charpy fracture properties

irradiation temperature; and total displacement damage. There were very few data available which were associated with high helium levels, and many of these could not be included because they were obtained from different test geometries (small punch tests or different Charpy specimen sizes), and so the decision was made to exclude helium as an input. This may have added to the perceived noise on the dataset, although it is possible that the effects of helium are encompassed by the dpa measurement. In the cases that full compositional data were not available, the concentrations of deliberately added alloying elements were set to zero, and the concentrations of impurities, which are inevitably present, were set to be equal to the average of the available data.

The data were also missing comprehensive information on yield stress and fracture mode. The data were also restricted to sub-sized Charpy specimens with cross-sections ranging from 3.3×3.3 mm to 3×4 mm to avoid problems associated with the scaling of specimens (Abe and Kayano, 1996).

As in the yield stress model, the data lacked information on the irradiation damage rate or time.

The targets for the models were ΔDBTT and ΔUSE . In addition to the raw inputs, the following functional forms were included:

1. “Kinetic time” terms for the heat treatments, and for the heat treatment effect of the irradiation. These are terms that combine time and chemical rate effects, and have the form $t \exp\left(\frac{-Q}{kT}\right)$ where t is the time elapsed at a temperature T , Q is an activation energy, and k is Boltzmann’s constant. In the case of irradiation, where irradiation time was absent, the damage was substituted on the assumption that damage rates K did not depend on the irradiation method.
2. A term $\frac{1}{C}$ where C is degree of cold working.
3. A term \sqrt{Kt} , where K is the irradiation damage rate and t the irradiation time (making Kt the total damage).

Prior to training, both sets of data were randomly divided into two equal groups designated the training and test databases, and normalised.

6.3 Neural network models of Charpy fracture properties

Input variable	Min.	Max.	Mean	Standard deviation
Normalising temperature, T_{norm} , K	273.	1373.	1297.6	95.7
Normalising time, t_{norm} , hours	0.	2.0	0.67	0.33
Tempering temperature, T_{temp} , K	273.	1023.	1013.2	83.0
Tempering time, t_{temp} , hours	0.	2.5	1.71	0.50
Irradiation temperature, T_{irr} , K	333.	823.	625.7	71.0
Dose, dpa	0.	100.	5.42	10.21
Cold work, %	0.	27.	0.94	4.95
Composition, wt%				
C	0.005	0.2	0.115	0.025
Cr	0.	12.0	8.854	1.951
W	0.	2.12	1.009	0.889
Mo	0.	1.0	0.207	0.340
Ta	0.	0.48	0.033	0.046
V	0.	0.314	0.218	0.064
Si	0.	0.4	0.173	0.123
Mn	0.04	1.35	0.496	0.269
N	0.0007	0.06	0.018	0.012
Al	0.001	0.054	0.015	0.015
B	0.	0.009	0.003	0.003
Co	0.0024	0.02	0.006	0.004
Cu	0.0017	0.035	0.012	0.011
Nb	0.0001	0.2	0.035	0.065
Ni	0.005	2.0	0.181	0.332
P	0.002	0.016	0.007	0.005
S	0.0002	0.008	0.004	0.002
Ti	0.001	0.02	0.006	0.003
Zr	0.	0.059	0.007	0.017

Table 6.1: Various inputs in the Δ DBTT data set, their ranges, means and standard deviations.

6.3 Neural network models of Charpy fracture properties

Input variable	Min.	Max.	Mean	Standard deviation
Normalising temperature, T_{norm} , K	273.	1373.	1297.6	95.4
Normalising time, t_{norm} , hours	0.	2.0	0.66	0.33
Tempering temperature, T_{temp} , K	273.	1023.	1012.2	84.4
Tempering time, t_{temp} , hours	0.	2.5	1.71	0.50
Irradiation temperature, T_{irr} , K	333.	743.	622.2	68.6
Dose, dpa	0.	100.	4.85	9.60
Cold work, %	0.	27.	0.97	5.04
Composition, wt%				
C	0.005	0.2	0.113	0.023
Cr	0.	12.0	8.815	1.939
W	0.	2.12	1.015	0.892
Mo	0.	1.0	0.190	0.324
Ta	0.	0.48	0.034	0.047
V	0.	0.314	0.217	0.064
Si	0.	0.4	0.167	0.119
Mn	0.04	1.35	0.501	0.271
N	0.0007	0.06	0.018	0.012
Al	0.001	0.054	0.015	0.015
B	0.	0.009	0.003	0.003
Ce	0.	0.13	0.001	0.009
Co	0.0024	0.02	0.006	0.004
Cu	0.0017	0.035	0.012	0.011
Nb	0.0001	0.2	0.035	0.065
Ni	0.005	0.97	0.176	0.324
P	0.002	0.016	0.007	0.005
S	0.0002	0.008	0.004	0.002
Ti	0.001	0.02	0.006	0.003
Zr	0.	0.059	0.008	0.018

Table 6.2: Various inputs in the Δ USE data set, their ranges, means and standard deviations.

6.3.2 Model training

6.3.2.1 Δ DBTT model

A total of 105 networks were successfully trained with from 1 to 20 hidden units, and from 6 different seeds. As expected, the perceived noise on the training data decreased with increasing complexity (Figure 6.5(a)). However, the test error – the ability of the models to generalise – is scattered and there are (comparatively) low scores for both low and high complexities of models (Figure 6.5(b)). The LPE also displays a high degree of scatter, although the general trend is increasing with increasing complexity, with a rough peak in the region of 12-14 hidden units (Figure 6.5(c)). As this error metric combines the accuracy of the nominal model prediction and the uncertainty associated with that prediction, this demonstrates that performance varies widely between models of similar complexities but different seeds, implying that there are many local minima in the neural network “weight space”.

More reliable results were obtained by combining models into a committee. In this case, the optimum committee was found to have 16 members (Figure 6.5(d)). Committee members possessed between 3 and 16 hidden units. The predictions for the committee, on the dataset, are shown in Figure 6.6. The committee average perceived noise in the dataset was 0.040, with a standard deviation of 0.007.

The network perceived significances, σ_w for each input are shown in Figure 6.7. Of particular note are committee opinions on the significance of phosphorus and sulphur, which are known to have an influence on embrittlement through segregation to the grain boundaries and crack tips; the agreement on the significance of chromium; the strong correlation with irradiation temperature (T_{irr}); and the preference for functions of the damage level such as \sqrt{dpa} rather than dpa alone. These are discussed in more detail later.

6.3.2.2 Δ USE model

A total of 127 networks were successfully trained with from 1 to 25 hidden units, and from 6 different seeds. The perceived noise on the training data decreased with increasing complexity as expected (Figure 6.8(a)), although, as with the Δ DBTT model the test error is very scattered and there are again comparatively low scores for both

6.3 Neural network models of Charpy fracture properties

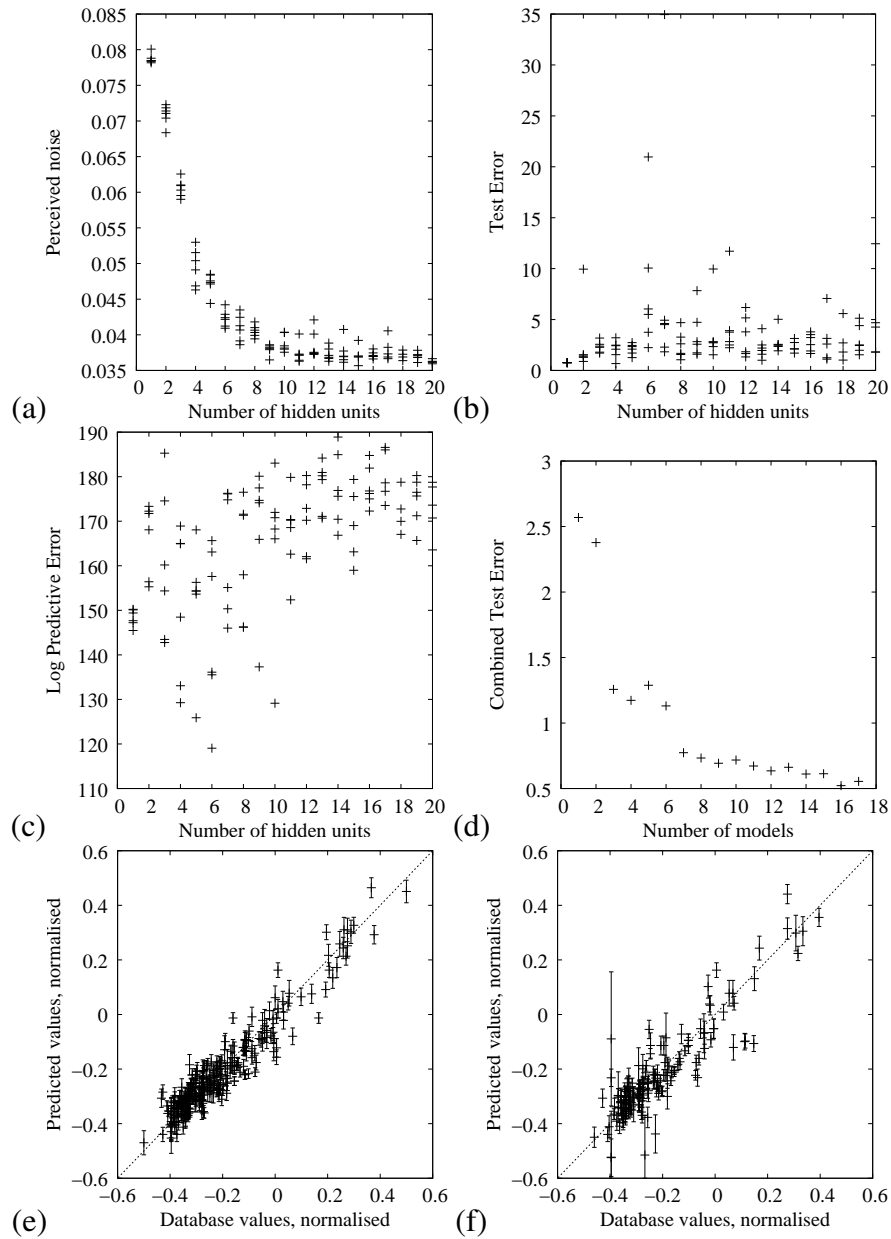


Figure 6.5: Δ DBTT model training reports: (a) perceived level of noise for the training data, (b) the error between the models and the test data, (c) log predictive error for increasing model complexity, (d) combined test error for different sizes of committee, (e) best single model performance on (normalised) training data and (f) test data.

6.3 Neural network models of Charpy fracture properties

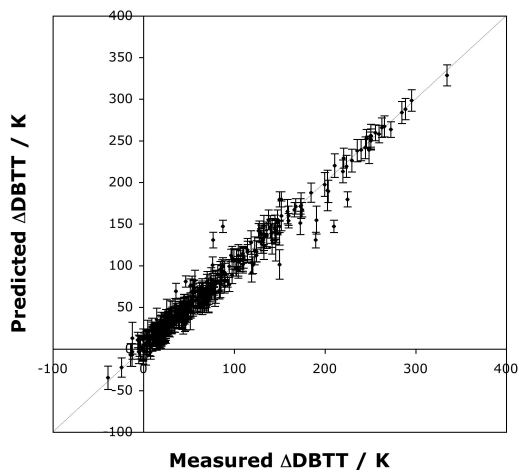


Figure 6.6: Committee model predicted irradiation-induced Δ DBTT plotted against the measured values for all points in the training database.

low and high complexities of models (Figure 6.8(b)). Also as for the Δ DBTT model, the LPE in this case displays a very high degree of scatter (Figure 6.8(c)).

More reliable results were obtained by combining models into a committee. In this case, the optimum committee was found to have 26 members (Figure 6.8(d)). Committee members possessed between 1 and 13 hidden units. The predictions for the committee, on the dataset, are shown in Figure 6.9. The committee average perceived noise in the dataset was 0.054, with a standard deviation of 0.013.

The network perceived significances, σ_w for each input are shown in Figure 6.10. In this case, the tempering time is found to be significant, as are carbon and chromium content. Irradiation temperature, on the other hand, is not found to correlate strongly with changes in USE. Once again, however, functions of dpa are found to be more significant than dpa alone.

6.3.3 Model predictions

6.3.3.1 Predictions for existing steels

The input compositions for all the predictions made below are shown in Table 6.3. Estimates were not made for all alloys in the database.

6.3 Neural network models of Charpy fracture properties

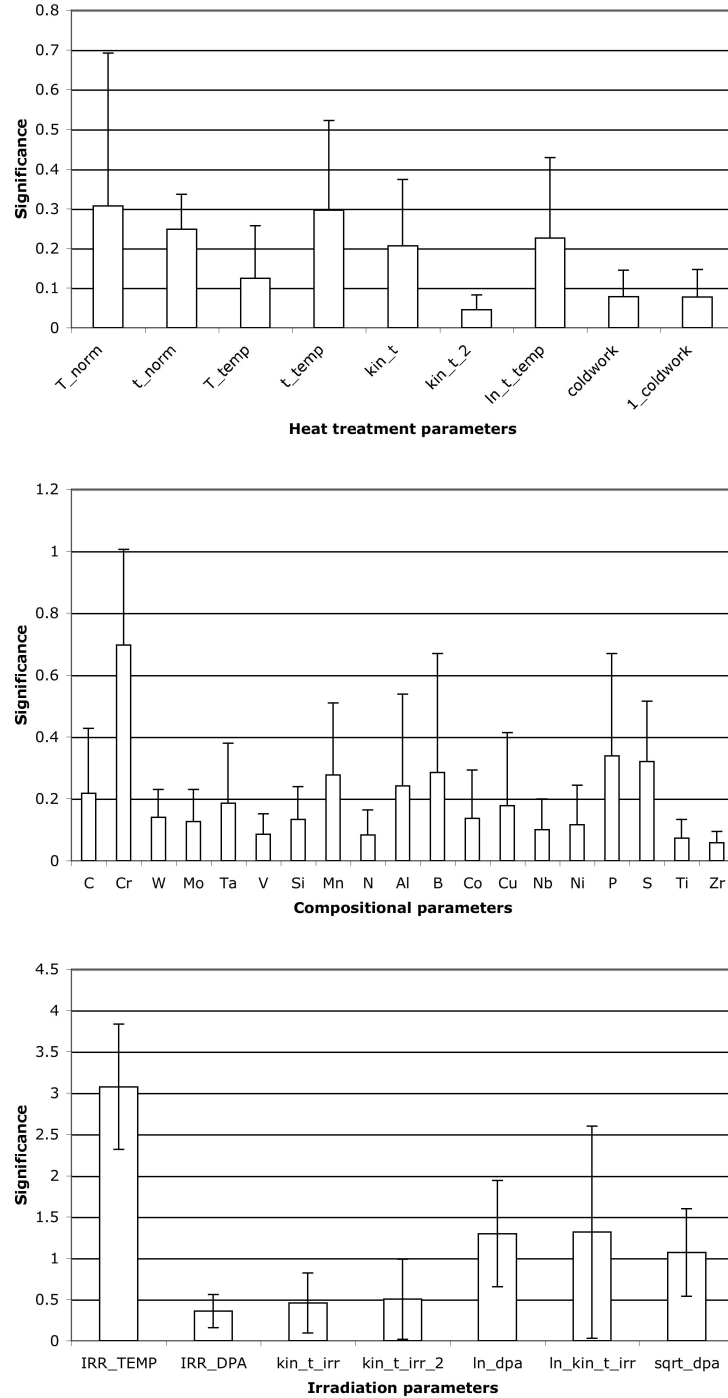


Figure 6.7: Average perceived significances (and standard deviation) σ_w for the committee members of the Δ DBTT model for pre-irradiation treatment (top), chemical composition (middle), and irradiation parameters (bottom).

6.3 Neural network models of Charpy fracture properties

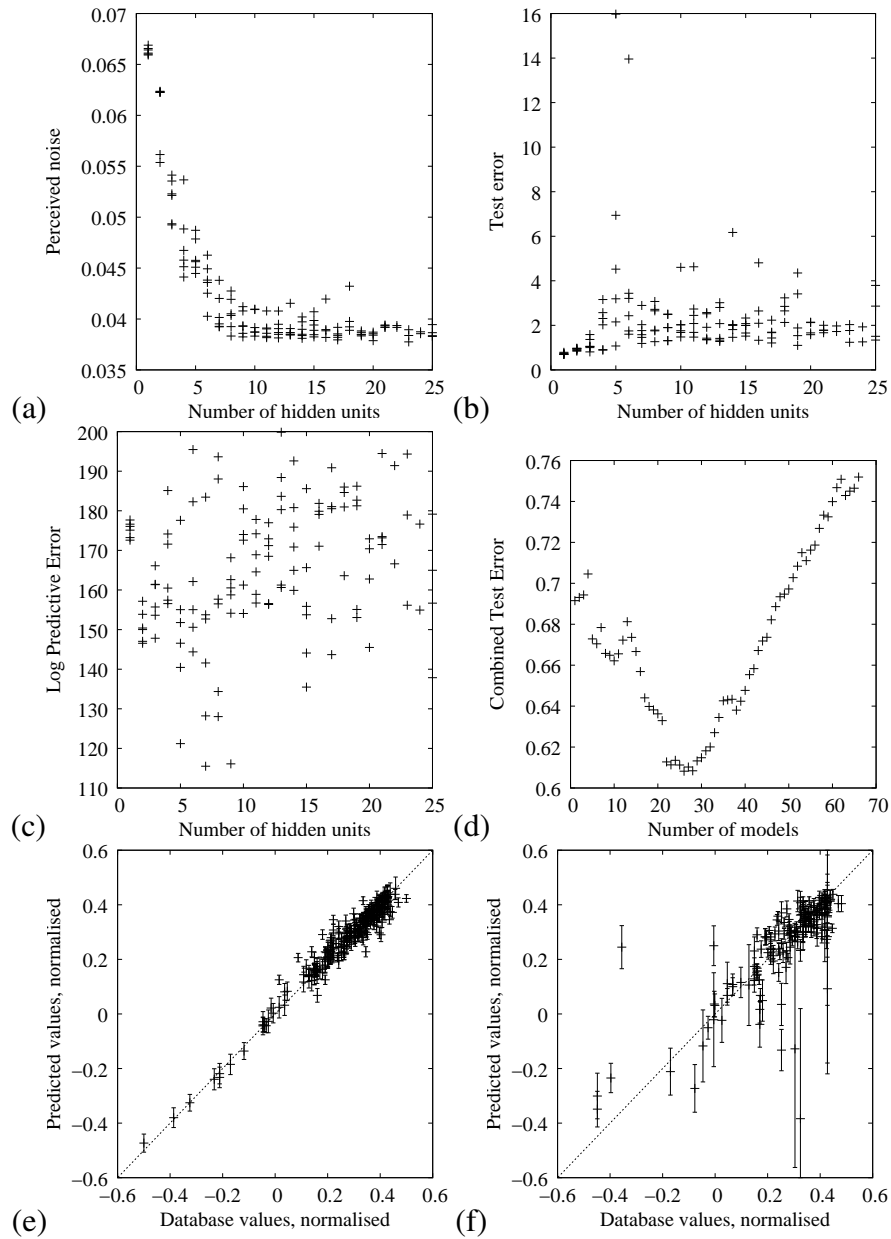


Figure 6.8: Δ USE model training reports: (a) perceived level of noise for the training data, (b) the error between the models and the test data, (c) log predictive error for increasing model complexity, (d) combined test error for different sizes of committee, (e) best single model performance on (normalised) training data and (f) test data.

6.3 Neural network models of Charpy fracture properties

Input	Alloy	
	F82H	Eurofer97
$T_{\text{Norm}} / \text{K}$	1040.	1050.
$t_{\text{Norm}} / \text{h}$	0.5	1.0
$T_{\text{Temp}} / \text{K}$	750.	750.
$t_{\text{Temp}} / \text{hr}$	2.0	2.0
Cold work / %	0.	0.
Composition		
C	0.1	0.1
Cr	7.5	9.0
W	2.0	1.1
Mo	0.01	0.01
Ta	0.03	0.07
V	0.2	0.2
Si	0.1	0.005
Mn	0.07	0.4
N	0.01	0.03
Al	0.005	0.005
B	0.001	0.001
Co	0.005	0.005
Cu	0.005	0.005
Nb	0.001	0.001
Ni	0.03	0.0075
P	0.002	0.005
S	0.003	0.003
Ti	0.004	0.004
Zr	0.0	0.0

Table 6.3: Model inputs (composition in wt%).

6.3 Neural network models of Charpy fracture properties

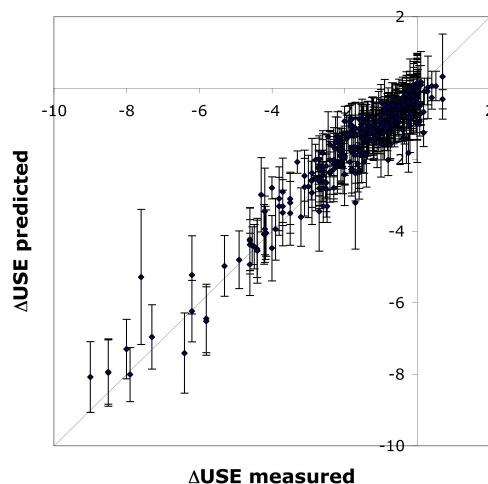


Figure 6.9: Committee model predicted irradiation-induced Δ USE plotted against the measured values for all points in the training database.

Irradiation temperature and dose

The model predictions for the effects of irradiation temperature and dose on Δ DBTT for Eurofer97 are shown in Figure 6.11. The overall trend is decreasing Δ DBTT with increasing T_{irr} . This is expected, as recovery processes operate more readily at high temperature. There also appears to be a general trend towards saturation at high dose consistent with an equilibrium between defect creation and recovery.

It is interesting that the predicted embrittlement at the highest T_{irr} , 450°C, is greater than that at 350°C. This may correspond to the onset of non-hardening embrittlement mechanisms, such as grain boundary helium bubble formation.

The Δ USE trends, as predicted by the model, are generally similar to the Δ DBTT trends – large shifts in DBTT tend to correspond to drops in USE (Figures 6.11 and 6.12). This occurred consistently across all behaviours explored.

Chemical influence

The effect of chromium content on radiation embrittlement is shown in Figure 6.12. There is a clear minimum at ~ 9 wt% Cr. This relationship has been commented on previously by Klueh and Harris (2001, p. 151), and is important as it suggests that there

6.3 Neural network models of Charpy fracture properties

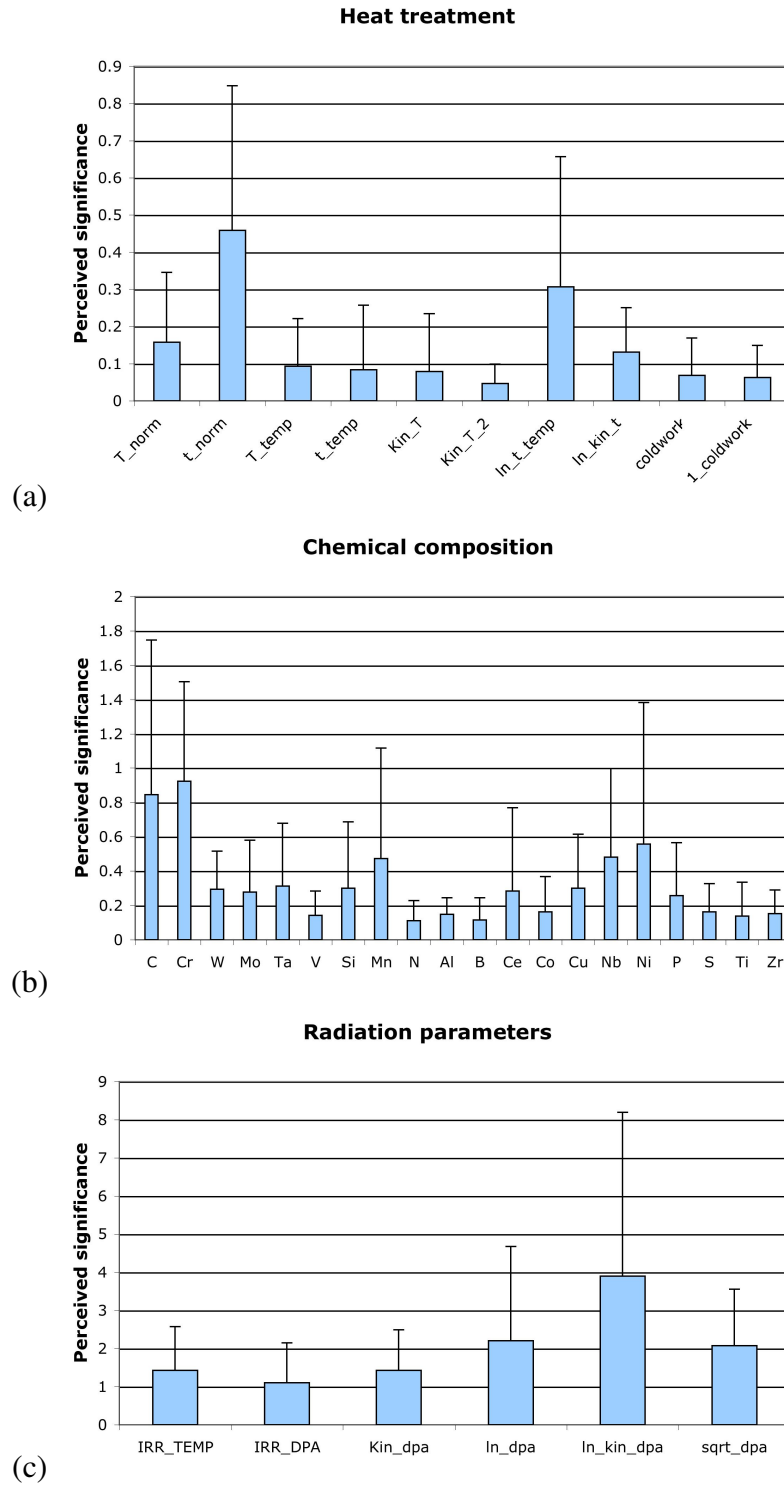


Figure 6.10: Perceived significances σ_w for the committee members of the Δ USE model for heat treatment and cold work (top), alloying elements (middle) and irradiation parameters (bottom).

6.3 Neural network models of Charpy fracture properties

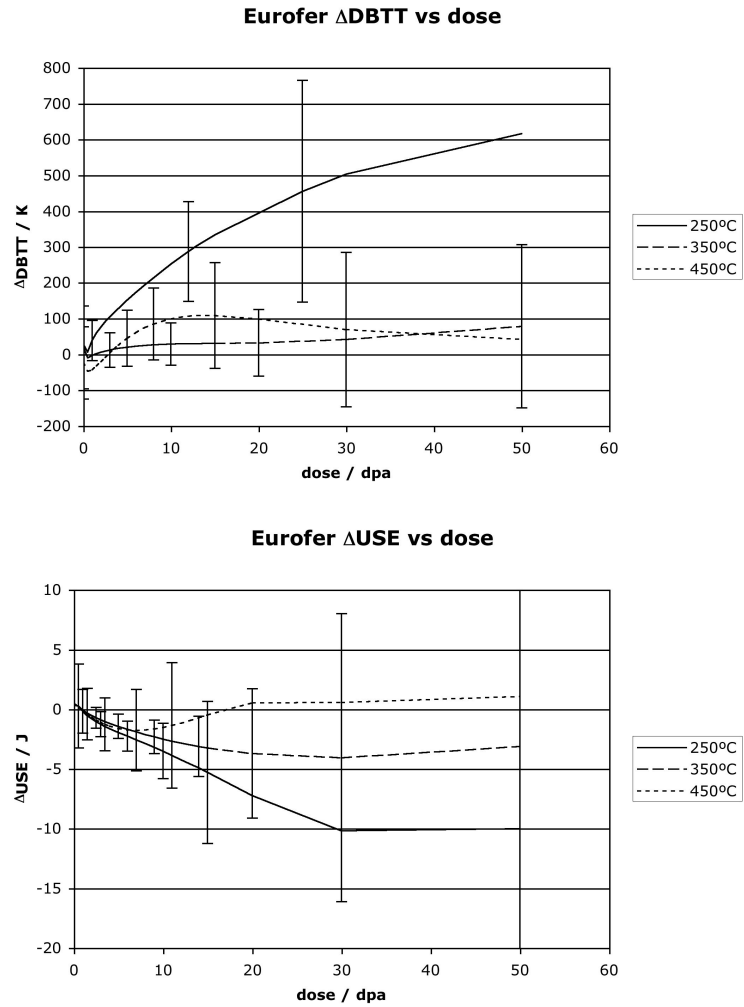


Figure 6.11: Model predictions for Δ DBTT (top) and Δ USE (bottom) variation with damage level for three different irradiation temperatures, for Eurofer97.

6.3 Neural network models of Charpy fracture properties

is an optimum chromium concentration that minimises in-service embrittlement. There is evidence that embrittlement occurs, at higher Cr concentrations, through formation of brittle Cr-rich α' -phase (Suganuma and Kayano, 1983). The mechanisms for low-Cr embrittlement are currently unknown. There was no correlation in the database between unirradiated DBTT and Δ DBTT.

Although there was no strong committee consensus on the significance of Ta concentration (Figure 6.7), predictions were made for different concentrations of Ta, as shown in Figure 6.13. Tantalum was originally intended to replace niobium as a strong carbide former, to strengthen the steel. However, 75-90% of Ta remains in solution after normalising, although it does produce austenite grain refinement and is expected to improve fracture toughness (Klueh, 2005). Although there are large modelling uncertainties, the trend in the model is indeed towards lower Δ DBTT at higher concentrations of Ta for all T_{irr} .

Temper embrittlement is caused by the segregation of phosphorus to grain boundaries at temperatures around 600°C (Shen et al., 2005). Behaviour typical of this sort of high-temperature embrittlement was detected in the model (Figure 6.14). Although this occurs above the general design operating temperatures for RAFM steels, this phenomenon has the potential to cause high-temperature embrittlement in future, high-temperature variants unless controlled for.

Into the fusion regime

Figure 6.15 (Eurofer97) and Figure 6.16 (F82H) show the neural network predictions of Δ DBTT and corresponding uncertainty estimates over a range of temperatures (300-900 K) and damage levels (0-200 dpa).

Figure 6.17 (Eurofer97) and Figure 6.18 (F82H) show the neural network predictions of Δ USE and corresponding uncertainty estimates over the same range of temperatures and damage levels.

The regions well outside the training database have uncertainties of the same order of magnitude, or greater than, the values of the predictions. These uncertainties provide an indication that predictions in these areas should be regarded sceptically, and that experiments in these regions would provide valuable information.

6.3 Neural network models of Charpy fracture properties

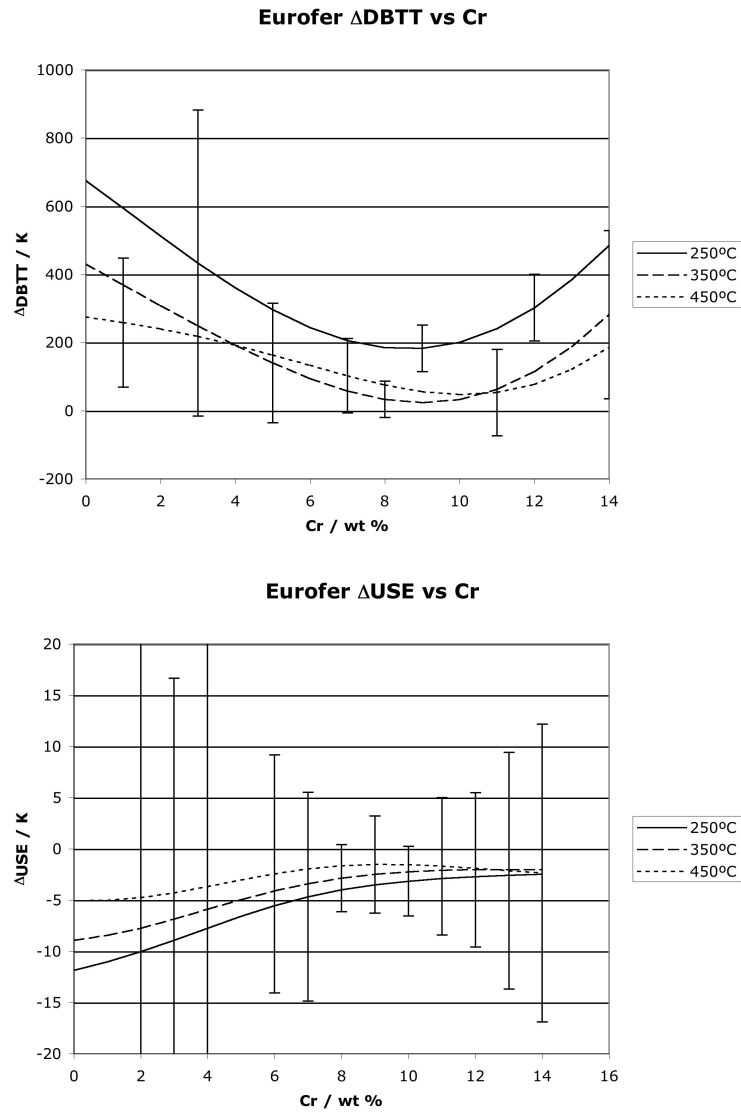


Figure 6.12: Model predictions for Δ DBTT (top) and Δ USE (bottom) variation with Cr content for three different irradiation temperatures. The basic alloy composition, except for Cr, was that of Eurofer97 and the damage level was 10 dpa.

6.3 Neural network models of Charpy fracture properties

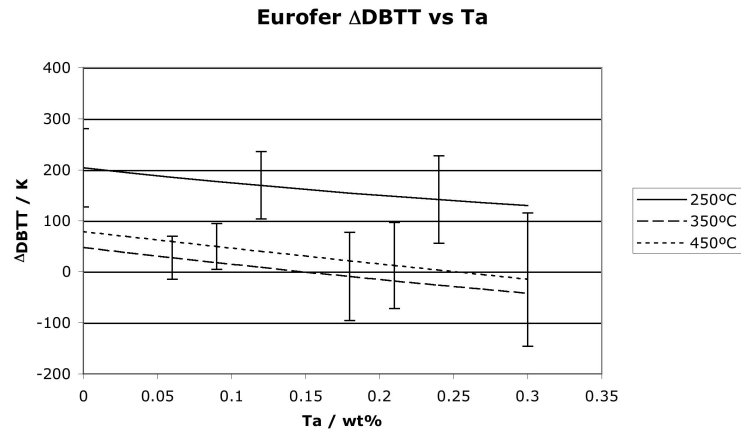


Figure 6.13: Model predictions for Δ DBTT variation with Ta content for three different irradiation temperatures. The basic alloy composition, except for Ta, was that of Eurofer97 and the damage level was 10 dpa.

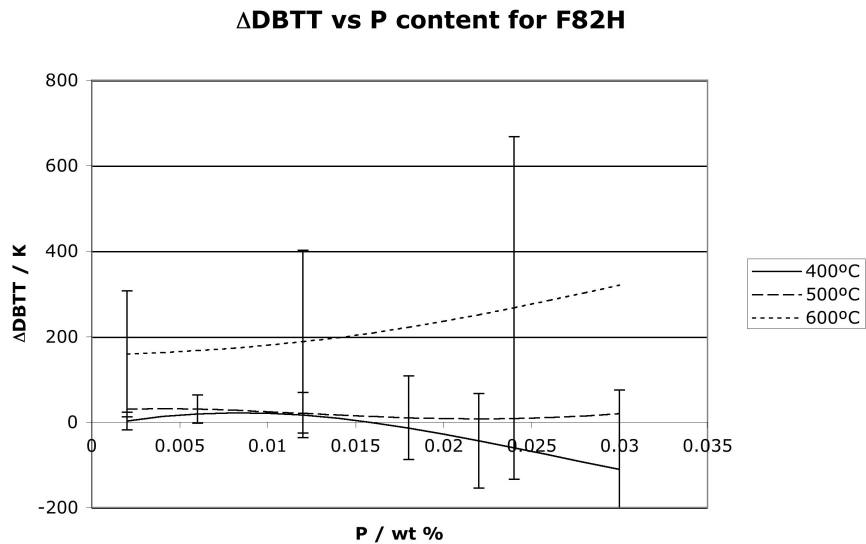


Figure 6.14: Model predictions for Δ DBTT variation with P content for three different irradiation temperatures. The basic alloy composition, except for P, was that of F82H and the damage level was 2.5 dpa. The markedly different behaviour at 600°C is characteristic of temper embrittlement.

6.3 Neural network models of Charpy fracture properties

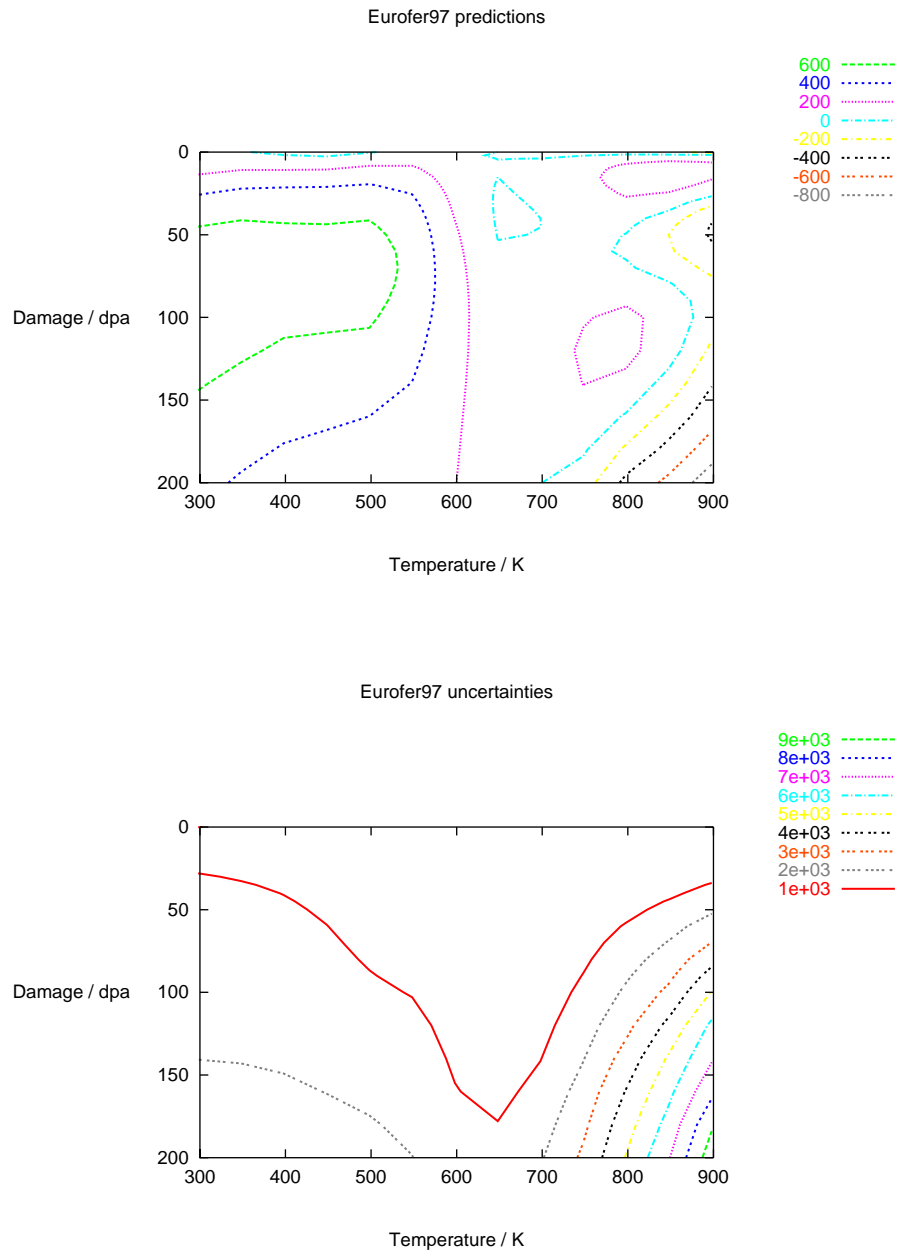


Figure 6.15: Model predictions (and modelling uncertainties) for Δ DBTT for Eurofer97 as a function of irradiation temperature and damage level. The contour scales are in Kelvin.

6.3 Neural network models of Charpy fracture properties

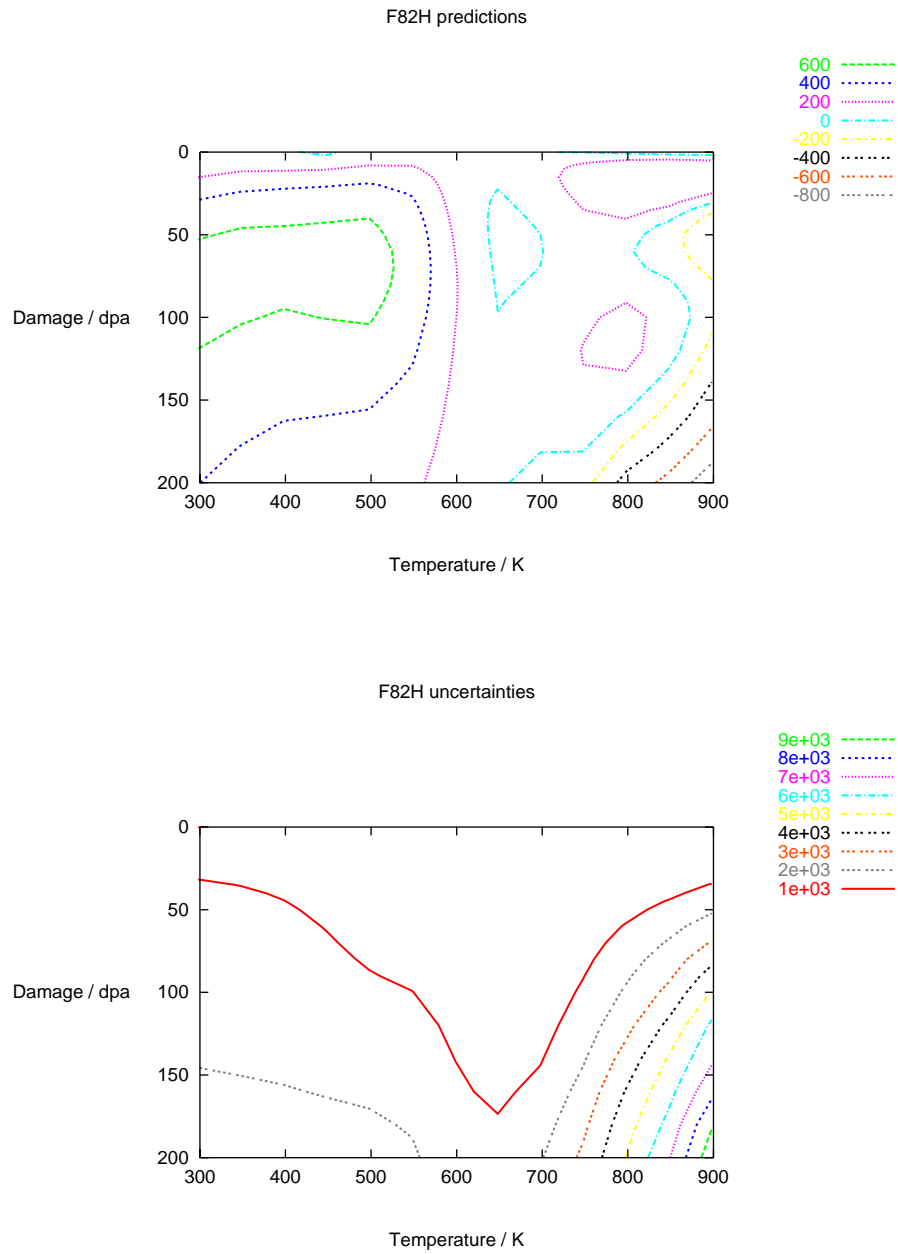


Figure 6.16: Model predictions (and modelling uncertainties) for Δ DBTT for F82H as a function of irradiation temperature and damage level. The contour scales are in Kelvin.

6.3 Neural network models of Charpy fracture properties

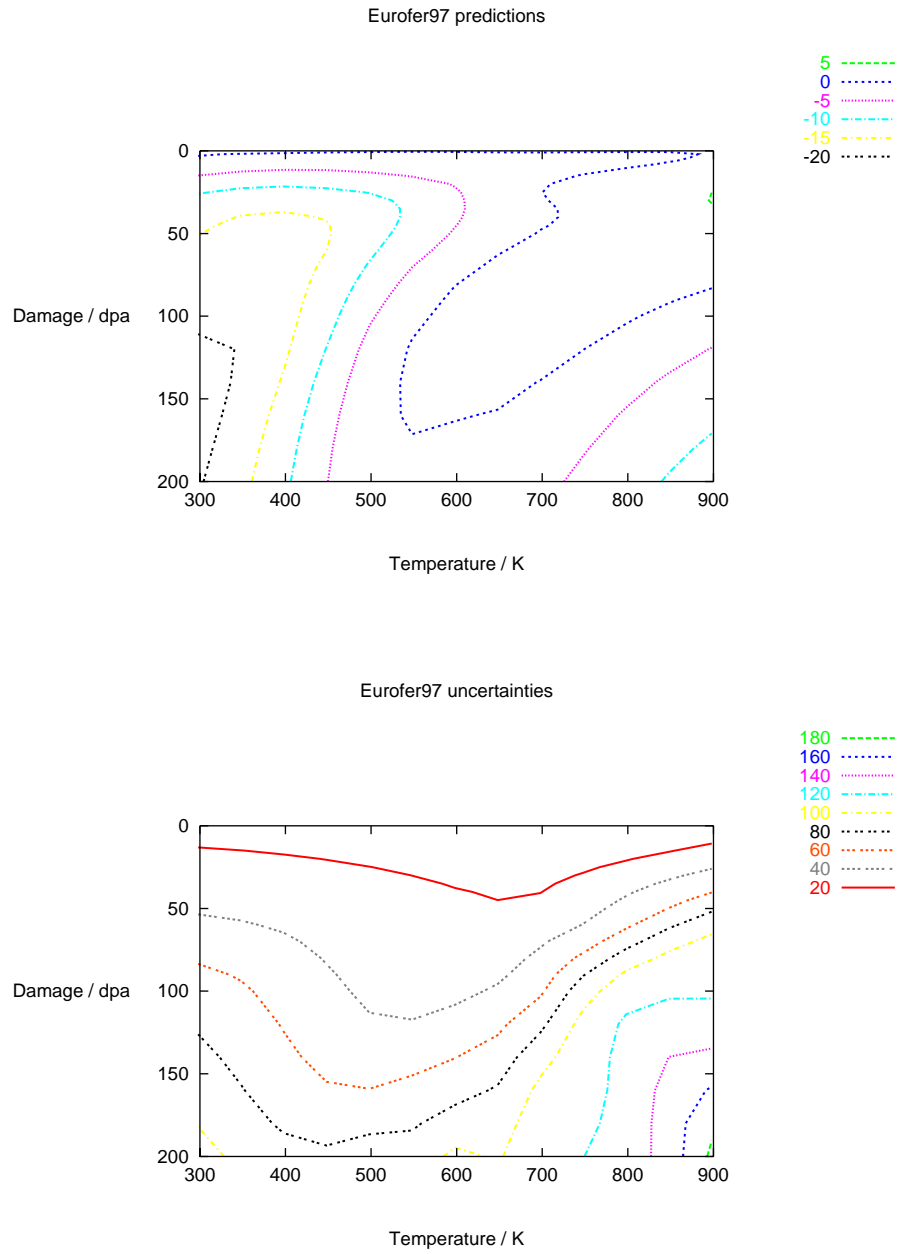


Figure 6.17: Model predictions (and modelling uncertainties) for Δ USE for Eurofer97 as a function of irradiation temperature and damage level. The contour scales are in joules.

6.3 Neural network models of Charpy fracture properties

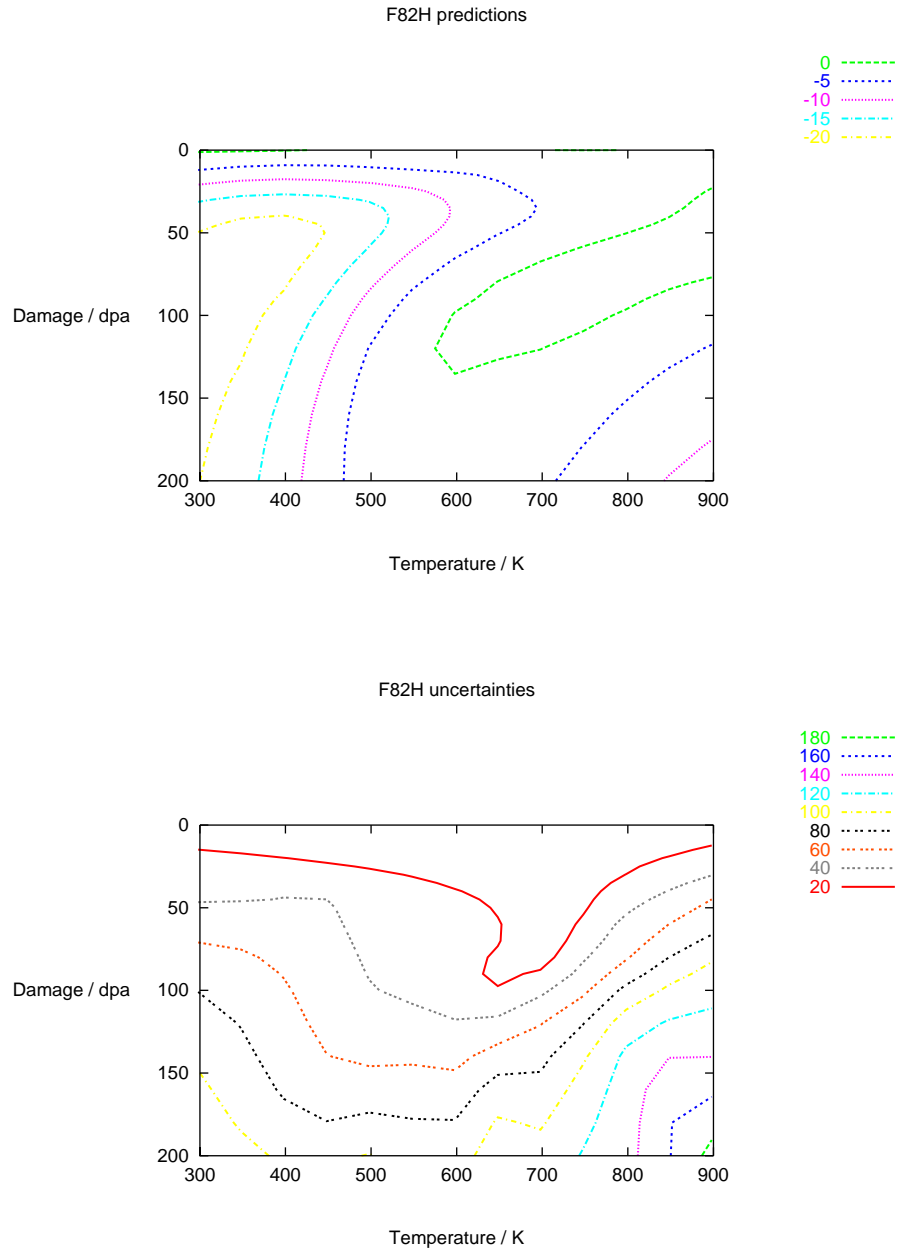


Figure 6.18: Model predictions (and modelling uncertainties) for Δ USE for F82H as a function of irradiation temperature and damage level. The contour scales are in joules.

6.3 Neural network models of Charpy fracture properties

Input	Eurofer97	Values		
Irradiation Temperature /K	600.	600.	700.	800.
C	0.1	0.22	0.13	0.0
Cr	9.	9.69	9.49	8.61
W	1.1	1.43	2.32	1.32
Mo	0.	0.50	0.50	0.50
Ta	0.15	0.24	0.24	0.24
V	0.2	0.42	0.24	0.16
Si	0.	0.48	0.51	0.20
Mn	0.	0.07	0.13	0.55
Damage /dpa	5.	5.	5.	5.
Target / K	--	0.	0.	0.
Prediction / K	-92.	-111.	-42.	-49.
Uncertainty / K	116.	279.	203.	220.

Table 6.4: Δ DBTT genetic algorithm best results for irradiation to 5 dpa under various conditions, compared to Eurofer97 (chemical compositions in wt%).

However, for both materials, the models predict a maximum Δ DBTT of around 200 K at irradiation temperatures of 700-900 K, the design operating temperatures of RAFM steels. The prediction of saturation and/or recovery during irradiation at these temperatures is promising, as it offers the possibility of identifying alloy compositions which have a reduced peak Δ DBTT.

6.3.4 Optimisation of steel composition

The genetic algorithm procedure described in Chapter 4 was carried out on the ANN models described above. The target was to identify steel compositions with minimal shifts in DBTT. In this case, three irradiation temperatures (600, 700 and 800 K) and two damage levels (5 and 20 dpa) were explored. The concentrations of the major RAFM alloying elements (C, Cr, W, Mo, Ta, V, Si, and Mn) were allowed to vary. The concentrations of all other elements were fixed at the ‘‘impurity levels’’ used for the training database, as described above. Heat treatments were fixed at one hour normalising at 1050°C and two hours tempering at 750°C with no cold working, as per Eurofer97.

The conditions, targets, and results for the genetic algorithm optimisation procedure are summarised in Tables 6.4 and 6.5.

6.3 Neural network models of Charpy fracture properties

Input	Eurofer97	Values		
Irradiation Temperature /K	600.	600.	700.	800.
C	0.1	0.11	0.11	0.15
Cr	9.	9.96	9.66	9.79
W	1.1	1.54	1.06	1.06
Mo	0.	0.50	0.65	0.99
Ta	0.15	0.24	0.24	0.24
V	0.2	0.23	0.23	0.24
Si	0.	0.20	0.20	0.27
Mn	0.	0.0	0.04	0.12
Damage /dpa	20.	20.	20.	20.
Target / K	--	0.	0.	0.
Prediction / K	90.	33.	-11.	3.
Uncertainty / K	193.	274.	228.	265.

Table 6.5: Δ DBTT genetic algorithm best results for irradiation to 20 dpa under various conditions, compared to Eurofer97 (chemical compositions in wt%).

The predictions for low dose (5 dpa) demonstrate some inaccuracy in the model in this region, predicting negative nominal Δ DBTT shifts (although the modelling uncertainties certainly extend into the positive region). However, for fusion use, the higher-dose (20 dpa) results will be used to recommend a steel composition.

It is interesting that, although there is a general minimum in Δ DBTT at around 9 wt% Cr (Figure 6.12), the optimised compositions are slightly closer to 10 wt% Cr. This is a consequence of non-linear effects, in the model, of other alloying elements. The model also recommended additional Ta (Figure 6.13).

6.3.4.1 Predictions for optimised steel

A steel with the composition 0.11C-9.8Cr-1W-0.5Mo-0.24Ta-0.2V-0.2Si-0.1Mn is suggested by the results above. This differs from the recommendation for limited irradiation hardening, demonstrating the problems with optimising single properties individually.

Figure 6.19 shows predictions for embrittlement of a steel of this composition at three irradiation temperatures. The predictions indicate a steel which undergoes only moderate embrittlement. The modelling uncertainties are large at high doses, but this is

6.3 Neural network models of Charpy fracture properties

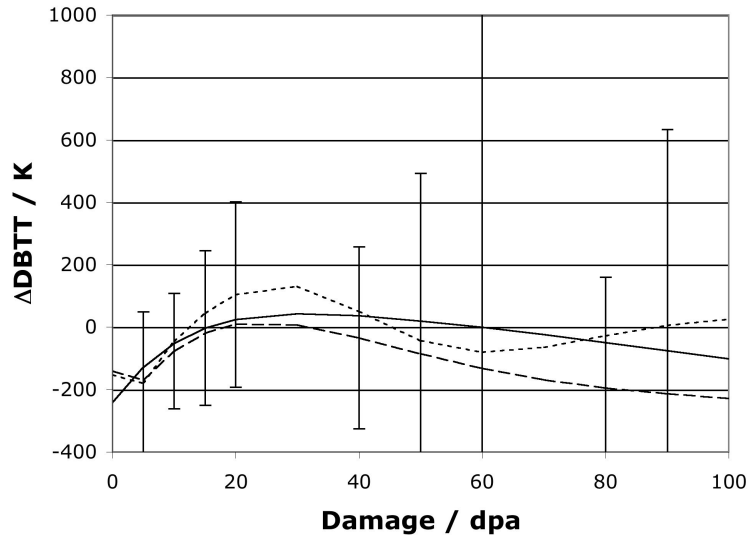


Figure 6.19: Δ DBTT predictions (and modelling uncertainties) for the GA optimised steel composition for three different irradiation temperatures.

because the composition represents a novel proposal, and because of the limited extent of the training dataset.

As mentioned above, this alloy composition differs from that offered in Chapter 5, which optimised for limited radiation hardening. In addition to the problem of optimising for multiple goals, this is compounded by the reduced inputs for the hardening dataset (particularly the exclusion of heat treatments) resulting in additional noise in that model, and the reduced dataset for the embrittlement model, resulting in increased modelling uncertainty. Additionally, allowing the heat treatment parameters to vary may result in further improvements, but it is doubtful that such improvements would be particularly dramatic.

6.3.5 The need for more data

Although it has been stated before, it bears repeating that the available data are sparse and noise levels in the dataset are high. It is important that experimental data are reported as fully as possible. In particular, the conclusion is unavoidable that the extent of radiation damage cannot be characterised by a single parameter. The dpa number,

6.3 Neural network models of Charpy fracture properties

regardless of how well it is computed, is a measure of the number of defects remaining shortly after a cascade has cooled down to ambient temperature, but only a fraction of these contribute to the final macroscopic property changes observed. The effects depend not only on the material, the recoil energy, and the temperature, but also on the property change being considered (hardening, swelling, irradiation creep, embrittlement *etc.*). Nevertheless, the dpa number remains a useful first tool for correlating results obtained by different particles, energies, and fluxes (Ullmaier and Carsughi, 1995).

Further work includes the incorporation of new data into the training database, and the incorporation of further physically significant inputs to test their significance. As the models become more refined, their ability to identify optimised alloys and hence their useful application in engineering a fusion power plant improves. This work will also include development of the genetic algorithm code to allow optimisation of an alloy for multiple selection criteria, as described in Chapter 5.

Chapter 7

Void nucleation in irradiated materials

The formation of cavities¹ in irradiated materials is a long-standing problem. Cavities grow by accumulation of vacancies – created in radiation cascades – and can grow to be hundreds of nanometres across. This results in macroscopic swelling of the material, up to tens of percent (Figure 7.1). The consequences for plant components can be severe. For structural components of a power plant, dimensional changes of less than 1% are tolerable, but still undesirable.

7.1 The origin of cavities

It has long been known that the cavities formed under irradiation are not purely helium-supported, at least once they are readily visible. Cawthorne and Fulton (1967) demonstrated that there were too few helium atoms produced by the (n,α) reactions in a fast reactor to fill all the cavities observed to equilibrium pressure. However, although it is possible for voids to form through classical nucleation mechanisms of vacancy accumulation, driven by the supersaturation of vacancies in the material, this cannot account for the numbers of voids observed in irradiated metals (Stoller and Odette, 1987).

It is now generally accepted that cavities are formed when gas bubbles nucleate and slowly grow by accumulation of vacancies and more helium atoms until they become

¹In this chapter, I have tried to consistently use *cavity* to denote any hollow inclusion in a material, *bubble* to denote a cavity which is primarily stabilised by internal gas pressure, and *void* to denote a cavity which is not gas-stabilised ($P \ll \frac{2\gamma}{r}$). Only radiation-induced cavities are of interest here.

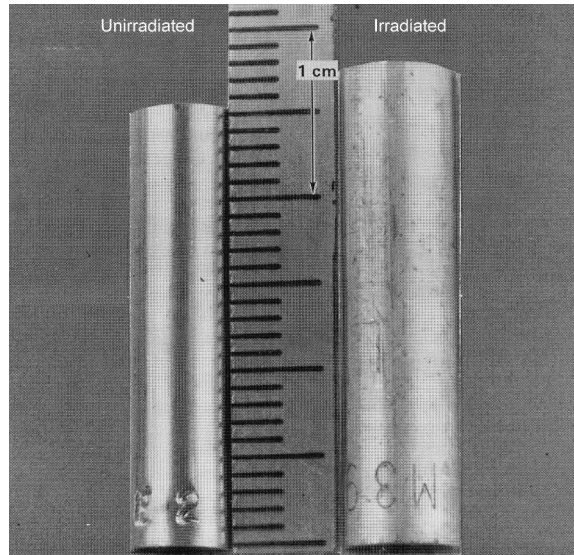


Figure 7.1: Photograph of 20% cold-worked 316 stainless steel rods before (left) and after (right) irradiation at 533°C to a fluence of 1.5×10^{23} neutrons m^{-2} in the EBR-11 reactor (Mansur, 1994).

large enough to act independently as microstructural sinks and undergo further growth by vacancy accumulation alone.

The sink strength for a distribution of spherical cavities, demonstrating the dependence on cavity radius, is given by:

$$k^2 = 4\pi rC \quad (7.1)$$

in which k^2 is the sink strength, r is the average cavity radius and C is the average number density of cavities (Brailsford and Bullough, 1972).

The driving supersaturation of vacancies arises due to preferential absorption of self-interstitials at microstructural sinks such as dislocations (*dislocation bias*) (Brailsford and Bullough, 1972), and by preferential production of mobile vacancies in cascades, during which interstitials can cluster into immobile structures such as loops (*production bias*). Production bias models have been successful in predicting swelling rates at low temperatures where dislocation bias models underestimate these rates (Woo and Singh, 1990). However, the production bias model also predicts cessation of void growth (and therefore macroscopic swelling) at high doses, which is not always

observed experimentally (Hudson et al., 2002).

After formation, growth of the void and the further evolution of the microstructure can be tracked using rate theory (for example, Bullough et al. (1977)). The problem is how bubbles of this size form initially, and there are currently no reliable and tested models for void creation (Okita and Wolfer, 2004). Russell (1978) derived a rate theory-based description of helium-catalysed void nucleation, and extended this work to include destruction of sub-critical bubbles in radiation cascades (Russell, 1996). Although Russell's derivation is based on the ideal gas law (Russell, 1972), rather than a high-pressure corrected equation of state such as Van der Waals (which also does not adequately describe helium (Trinkaus and Singh, 2003)), it shares features with more recent variations on this approach with similar properties (for example, Mansur (1987b) and Stoller and Odette (1985)). Therefore, Russell's approach is described in Section 7.3 to illustrate the properties of this model.

7.2 Description of dissolved helium

In this section the interstitial solid solution model of McLellan and Dunn (1969) is applied to helium in iron. This model has been successfully applied to previous problems, particularly regarding the properties of carbon in iron (Bhadeshia, 1982). It is known that helium will cluster and self-trap in metals under certain conditions (Lucas, 1984), and it is therefore assumed that helium atoms in solution have an attractive pairwise interaction energy. A calculation assessing the importance of this interaction on the nucleation of helium bubbles can then be carried out.

7.2.1 The quasi-chemical model

7.2.1.1 Gas potential in a void

The chemical potential per atom, $\mu_g(T, P)$, of a real gas is given by

$$\mu_g = \mu^\circ(T) + kT \ln f \quad (7.2)$$

where $\mu^\circ(T)$ is the chemical potential in the standard state, f is the fugacity of the gas, k is Boltzmann's constant, and T is the absolute temperature.

The fugacity is given by

$$f = P + \frac{B_{i,2}P^2}{RT} + \frac{1}{2} \frac{(B_{i,2}^2 + B_{i,3})P^3}{RT} + \dots \quad (7.3)$$

where P is pressure, R is the molar gas constant and $B_{i,n}$ are the virial coefficients for the gas (described, for helium, in Beck (1968)).

7.2.1.2 Gas potential in solution

Helium, when dissolved in ferritic iron, sits at the octahedral interstices. The chemical potential per atom for an interstitial solid solution is

$$\mu_s = \bar{E}_u - T\bar{S}_u^v + kT \ln \frac{\frac{\theta}{\beta}}{1 - \frac{\theta}{\beta}} - \frac{zkT}{2} \ln \left[\left(\frac{\frac{\theta}{\beta}}{1 - \frac{\theta}{\beta}} \right)^2 \left(\frac{1 - \frac{\theta}{\beta} - \phi}{\frac{\theta}{\beta} - \phi} \right) e^{\left(\frac{-\omega}{kT}\right)} \right] \quad (7.4)$$

in which \bar{E}_u is the partial energy of the solute atoms in the infinitely dilute solution, \bar{S}_u^v is the partial excess (non-configurational) entropy, θ is the atom fraction of the solute, β (=3) is the number of relevant interstitial sites per solvent atom, z (=4) is the nearest-neighbour coordination number for the interstitial sites and ω is the pairwise interaction energy between nearest-neighbour solute atoms (McLellan and Dunn, 1969). A more rigorous form of this equation is given by Bhadeshia (1998), but the solubility of helium in iron is so low that the additional correction is unimportant in this work.

ϕ is given by

$$\phi = \frac{1 - \left(1 - 4 \left[1 - e^{\left(\frac{-\omega}{kT}\right)} \right] \frac{\theta}{\beta} \left[1 - \frac{\theta}{\beta} \right] \right)^{\frac{1}{2}}}{2 \left[1 - e^{\left(\frac{-\omega}{kT}\right)} \right]} \quad (7.5)$$

The deviation from Henrian behaviour is all contained in the last term of Eq. 7.4, so

$$\mu_s = \mu^\infty - \frac{zkT}{2} \ln \left[\left(\frac{\frac{\theta}{\beta}}{1 - \frac{\theta}{\beta}} \right)^2 \left(\frac{1 - \frac{\theta}{\beta} - \phi}{\frac{\theta}{\beta} - \phi} \right) e^{\left(\frac{-\omega}{kT}\right)} \right] \quad (7.6)$$

in which μ^∞ is the chemical potential of an infinitely dilute interstitial solution. It

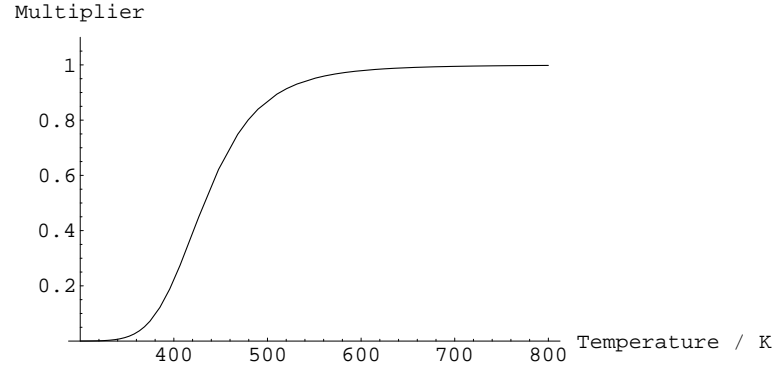


Figure 7.2: Value of the quasi-chemical term for deviation from ideal behaviour with temperature in body centred cubic (bcc) iron ($\theta = 1 \times 10^{-6}$ mole fraction, $\beta = 3$, $z = 4$).

should be noted that as $\omega \rightarrow 0$ or $\theta \rightarrow 0$, $\mu_s \rightarrow \mu^\infty$ as expected.

At equilibrium, the chemical potential in the gas phase must be the same as in solution. Equating the potentials therefore gives

$$f = e^{\left(\frac{\mu^\infty - \mu^\circ(T)}{kT}\right)} \left(\frac{\frac{\theta}{\beta}}{1 - \frac{\theta}{\beta}}\right)^{-z} \left(\frac{1 - \frac{\theta}{\beta} - \phi}{\frac{\theta}{\beta} - \phi}\right)^{\frac{-z}{2}} e^{\left(\frac{-z\omega}{kT}\right)} \quad (7.7)$$

For an ideal gas, $f = P$ and so this equation directly provides the pressure, P_e , in equilibrium with the dissolved gas atoms. For a non-ideal gas, Equation 7.3 must be solved to find P_e .

The latter part of Eq. 7.7 describes the deviation from ideal solution behaviour. Interstitial helium in bcc iron has a helium-helium binding energy of ~ 0.5 eV, meaning that the atoms are attracted to one another in solution (Morishita et al., 2001). This has the effect of increasing the solubility of helium in iron at low temperature (and hence, decreasing P_e), as shown in Figure 7.2.

7.2.1.3 Steady-state helium concentration under irradiation

Helium is highly insoluble in iron with an enthalpy of solution, for interstitial sites, of 5.25 eV atom⁻¹ (Morishita et al., 2001). As the migration energy is also very low, 0.078 eV (Morishita et al., 2001), this means that helium migrates very rapidly to microstructural traps such as dislocations and vacancies, and once in these traps, the atoms can no longer be regarded as being in solution.

It will therefore be necessary to estimate the helium concentration in solution in steady-state with these traps. Ghoniem et al. (1983) provide a framework for a complete treatment of this problem, but here we will concentrate on just two detrapping mechanisms – radiation re-solution from extended traps such as dislocations, and thermal detrapping from vacancies.

Equating the detrapping rate with the rate of impingement on sinks gives the rate equation

$$C_{\text{He}}^T b + C_{\text{He}}^V \nu \exp\left(\frac{-E_d}{kT}\right) = D_{\text{He}} C_{\text{He}} k_{\text{He}}^2 + R C_v C_{\text{He}} \quad (7.8)$$

in which C_{He}^T is the concentration of helium (per iron atom) in non-vacancy traps, C_{He}^V is the concentration of helium trapped at vacancies, b is the radiation re-solution rate (Ghoniem and Takata, 1982), ν is the vibration frequency of a trapped atom, E_d is the helium detrapping energy from a vacancy, D_{He} is the helium diffusion coefficient in solution, k_{He}^2 is the microstructural sink strength for helium, R is a reaction rate coefficient (described in Ghoniem et al. (1983)), C_v is the vacancy concentration and C_{He} is the concentration of helium in solution. Additionally, to conserve helium

$$C_{\text{He}}^T + C_{\text{He}}^V + C_{\text{He}} = C_{\text{He}}^0 \quad (7.9)$$

where C_{He}^0 is the total helium concentration in the material. Assuming most of the helium is trapped at any one time (*i.e.* $C_{\text{He}}^T, C_{\text{He}}^V \gg C_{\text{He}}$) allows an estimate of dissolved helium concentration (Figure 7.3).

7.2.2 Discussion

It is clear that the estimated steady-state concentration of helium atoms in solution is too low, under a wide range of conditions, for the quasi-chemical correction to be

7.2 Description of dissolved helium

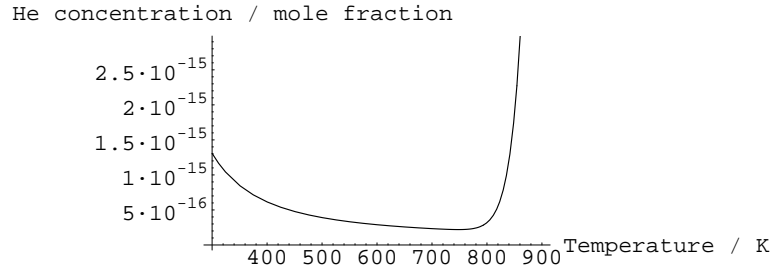


Figure 7.3: Estimate of dissolved He concentration in bcc iron under fusion conditions. At low temperatures radiation re-solution dominates; at high temperatures vacancy detrapping dominates. $b=10^{-5} \text{ s}^{-1}$, $k_{\text{He}}^2=10^{12} \text{ m}^{-2}$, $C_{\text{He}}^0=100 \text{ appm}$, $C_v=10^{-9}$.

significant. The correction affects equilibrium pressures, at low temperatures (below $\sim 400 \text{ K}$), at concentrations of 10^{-9} mole fraction and above.

The steady-state helium concentration calculated here, of around 10^{-15} mole fraction, is however still associated with an equilibrium fugacity of some $2 \times 10^{36} \text{ Pa}$ (an unphysically high pressure, from Eq. 7.3, of around $3 \times 10^{22} \text{ Pa}$ in helium). On the other hand, a bubble with a radius of 1 nm in which the gas pressure is balanced by the surface energy ($P = \frac{2\gamma}{r} = 4 \text{ GPa}$) would theoretically be in equilibrium, at 800 K, with a bulk helium concentration of around 10^{-24} mole fraction or, at 1000 K, 10^{-17} mole fraction.

During irradiation, therefore, any dissolved helium will always be at a huge supersaturation. Under such conditions, the critical radius for nucleation is extremely small (bubbles that would be in equilibrium with anything approaching the supersaturation conditions would be less than one atom across), meaning that the nucleation barrier is very small. In such circumstances, all available nucleation sites would be activated rapidly, leading to site saturation. This justifies a common assumption made in helium bubble studies, that the process simply involves the growth of a fixed number density of bubbles defined by the availability of helium and nucleation sites.

The calculations show that it is reasonable to neglect the nucleation stage of bubbles

in the steel irradiated in the fusion reactor. It is the number density of nucleation sites that determines the number density of bubbles. The evolution of the bubbles from minute size then depends on the rate of impingement of helium atoms on the bubble surface.

However, it is also true that the number density of nucleation sites will change under irradiation, and this should be incorporated into future models for swelling.

Heterogeneous nucleation sites such as grain boundaries have a lower effective surface energy than homogeneous sites for bubble formation, due to the grain boundary surface already present. However, because the critical bubble size is so small, there is no particular energetic advantage for helium bubble nucleation at such sites, although it may be easier for a bubble to grow on the grain boundary due to an increased helium flux along the boundary (*pipe diffusion*, Christian (2002, p. 413)). It would be expected that a bubble-depleted zone close to the boundary would emerge, due to reduced vacancy super-saturation.

7.3 Void nucleation model

Russell's inert-gas-assisted nucleation¹ model is based on describing the behaviour of a (n, x) -mer on an (n, x) plane, where n and x are the number of vacancies and the number of gas atoms in a cavity. Plotting this behaviour allows the identification of several distinct regions in the plane, bounded by *nodal lines* (Figure 7.4). These are lines along which \dot{n} and \dot{x} (that is, $\frac{\partial n}{\partial t}$ and $\frac{\partial x}{\partial t}$) are equal to zero. n^* and x^* represent, respectively, the critical number of vacancies and helium atoms which must be accumulated by an (n, x) -mer if it is to grow further by vacancy accumulation alone.

The nodal lines in Figure 7.4 intersect twice. The first intersection is a stable node, which attracts (n, x) -mers from the surrounding area on the (n, x) plane and represents a helium bubble. The second intersection is a saddle point – attracting (n, x) -mers from two areas and repelling them in two others – and is equivalent to a nucleated void.

It is clear that there are three possible arrangements for the nodal lines. These are

¹In this section *nucleation* is used to denote the transition of a cavity from helium-stabilised bubble to vacancy-accumulating void, as indicated in Figure 7.4.

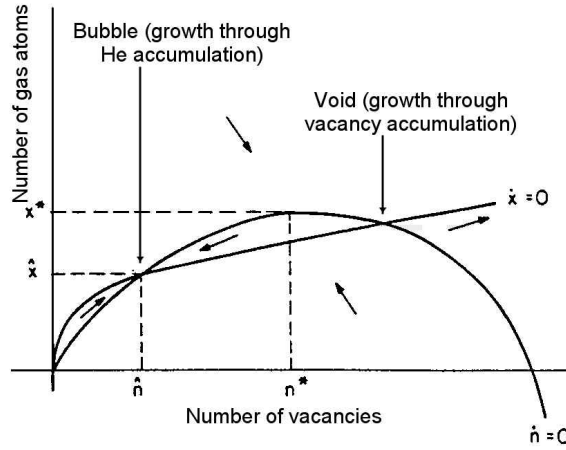


Figure 7.4: Schematic diagram of nodal lines in inert-gas aided void nucleation. Velocity vectors are indicated for the various regions (after Russell (1978)).

1. The situation in Figure 7.4, where the nodal lines cross twice. This is *gas-aided nucleation*. Small bubbles form, but develop only as far as the first, stable node. Further growth requires a stochastic fluctuation in gas or vacancy content.
2. If the $\dot{x} = 0$ line is raised, the nodal lines do not cross at all. This is *spontaneous nucleation*. In this situation, voids may form and grow from single vacancies or gas atoms, at a rate defined by the arrival rates of those species.
3. If the $\dot{x} = 0$ nodal line is depressed, it only crosses the $\dot{n} = 0$ line at one point (apart from the origin). In this case, any small bubbles which may form will tend to decay by thermal annealing, and therefore all nucleation must occur by large fluctuations in gas or vacancy content.

The nodal lines intersect at n values of

$$n^{\frac{1}{3}} = \frac{A}{3 \ln S_e} \pm \frac{A}{3 \ln S_e} (1 - \psi)^{\frac{1}{2}} \quad (7.10)$$

where

$$A = \frac{(36\pi\Omega^2)^{\frac{1}{3}} \gamma}{kT} \quad (7.11)$$

$$\psi = \frac{9\beta_x^0 \ln S_e}{A^2 K_x^c} \quad (7.12)$$

and S_e is the effective vacancy supersaturation, given by

$$S_e = S_v \left(1 - \frac{\beta_i^0}{\beta_v^0} \right) \quad (7.13)$$

Ω is the atomic volume, γ is the surface energy, S_v is the vacancy supersaturation ($= \frac{C_v}{C_v^e}$ where C_v is the vacancy concentration and C_v^e is the thermal equilibrium vacancy concentration), and k and T have their usual meanings. $\beta_{i,v,x}^0$ denote the arrival rates of self-interstitials, vacancies, and gas atoms respectively on a hypothetical void of one vacancy, and K_x^c is the probability, per gas atom, of radiation-forced re-resolution from the cavity.

The two nodal lines become tangent when $\psi = 1$, and do not intersect (spontaneous nucleation) when $\psi > 1$.

At the lower (\dot{n}, \dot{x}) intersection, $x = n \ln(S_e)$. In extreme cases, where S_e can equal 10^3 , this predicts 6-7 helium atoms per vacancy in the bubble – an unphysical result of the ideal gas law underpinnings. In fact, molecular dynamics calculations show that the lowest-energy configuration of an (n, x) -mer occurs when there is one helium atom per vacancy (Morishita et al., 2001).

Assuming that (prior to nucleation of voids) most of the mobile helium is provided by re-resolution from non-void traps (as in Section 7.2.1.3) then

$$\beta_x^0 = \frac{C_x^0 b}{a^2 k_x^2} \quad (7.14)$$

where C_x^0 is the total gas concentration, b is the probability, per gas atom, of radiation re-resolution from non-void traps, a is the material lattice spacing, and k_x^2 is the total microstructural sink strength for gas atoms.

Re-resolution parameters are complicated to calculate. Helium atoms can be re-inserted into the matrix either by a neutron directly colliding with the gas atom, or through the effects of a radiation cascade (Ghoniem and Takata, 1982). However, if we assume that purely gas-stabilized bubbles are small (and thus a gas atom does not have to be driven far into the matrix to be redissolved), then re-resolution probabilities

will be approximately the same for atoms in a bubble as they are in another trap.

Substituting Equation 7.14 into Equation 7.12 therefore gives

$$\psi = \frac{9C_x^0 \ln S_e}{A^2 a^2 k_x^2} \quad (7.15)$$

7.3.1 Properties of the void nucleation model

From Equation 7.15 it can immediately be seen that the dominant factor controlling the onset of spontaneous nucleation is the ratio $\frac{C_x^0}{k_x^2}$ – that is, the ratio of helium to helium sinks (Figure 7.5). Inserting typical values for S_e , A and a for a martensitic steel under irradiation and setting k_x^2 to a value of 10^{13} m^{-2} (representing a typical dislocation density, with dislocations as the dominant sink (Brailsford and Bullough, 1981)) produces spontaneous nucleation at He concentrations of around 5 appm. A typical oxide-dispersion strengthened (ODS) steel, on the other hand, might have 10^{24} m^{-3} oxide particles of 50 Å diameter or less (Miller et al., 2004), with the interface between particles and matrix representing a sink strength of 10^{15} - 10^{16} m^{-2} and allowing the absorption of 100-1000 times as much helium before spontaneous nucleation occurs. The qualitative use of increased sink concentrations has previously been discussed (Mansur et al., 1986). At this order of sink strength, however, cascade-induced fluctuations may become a dominating factor in void nucleation, destroying small voids and allowing larger voids to coarsen (Semenov and Woo, 2003).

Important evidence for a nucleation model of this form – the formation of stable bubbles which act as nucleation sites for the voids which result in macroscopic swelling – can be seen in Figure 7.6. The sharp, high peak of small cavities (formed from, at this size, roughly 5500 vacancies) and much broader distribution of larger, growing voids indicates that the smaller cavities are stable bubbles. This form of distribution has been widely reported in a variety of alloys after both ion and neutron irradiation (Mansur et al., 1986). Substitution of the experimental conditions (300 appm He, irradiation at 850 K) into Equation 7.10 and assuming an irradiation induced vacancy concentration of $\sim 10^{-8} \text{ atom}^{-1}$ and a sink strength of $\sim 4.2 \times 10^{12} \text{ m}^{-2}$ gives the lower nodal intersection at $n \approx 6000$ vacancies – equivalent to a spherical cavity of radius $\sim 2.6 \text{ nm}$.

7.3 Void nucleation model

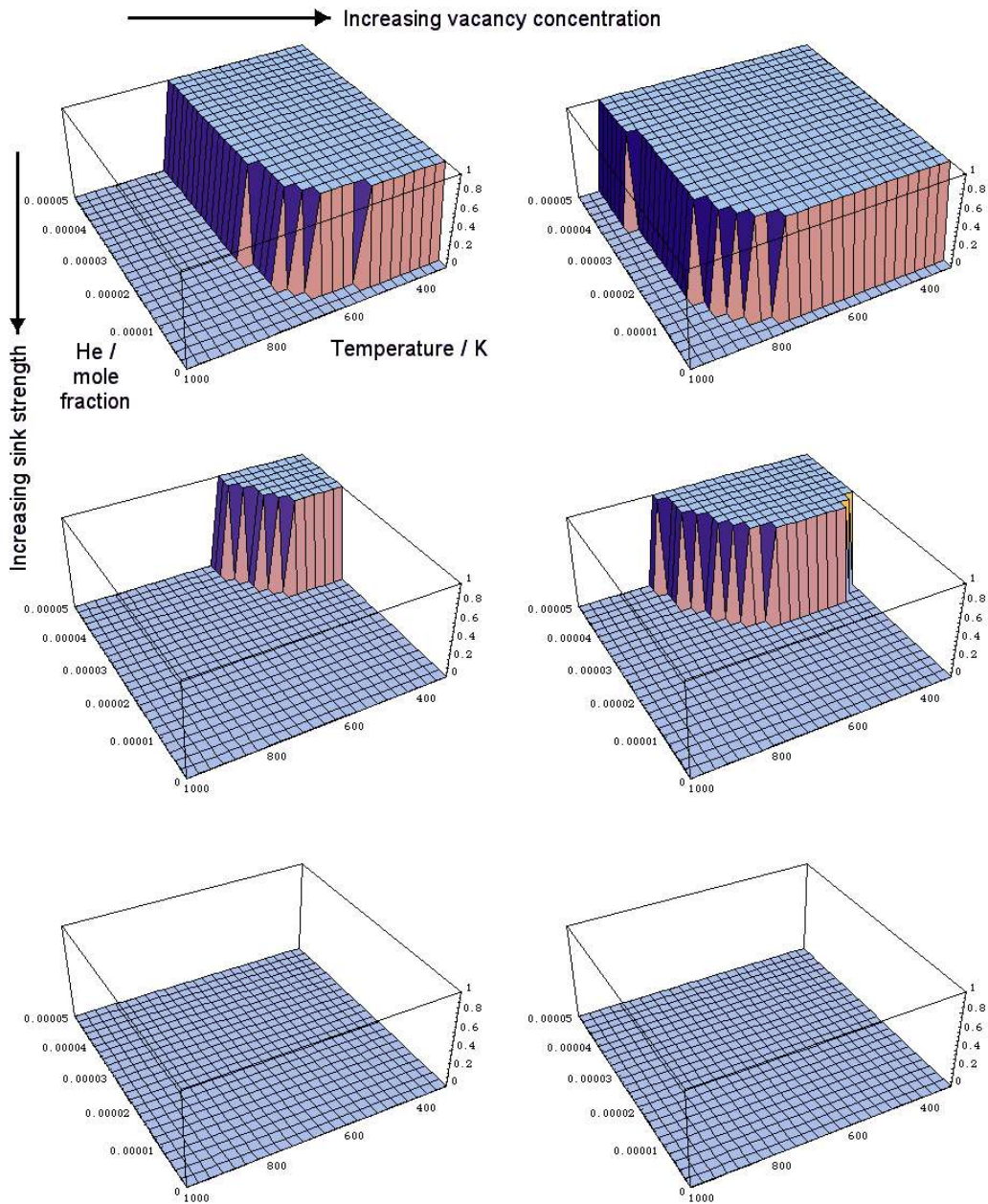


Figure 7.5: Areas of spontaneous nucleation of cavities in steel as a function of temperature, helium sink strength, helium content, and vacancy concentration in the Russell model.

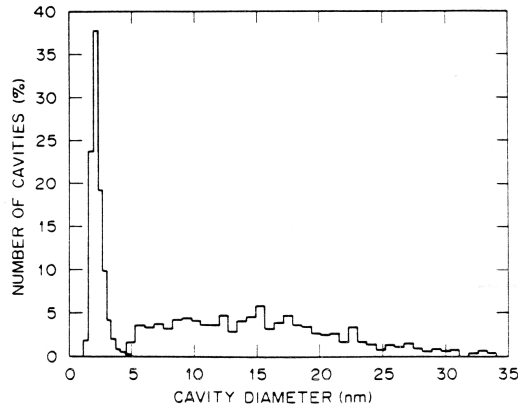


Figure 7.6: Histogram showing the bimodal cavity size distribution observed after irradiation of Fe-10Cr with 4 MeV Fe ions to 30 dpa at 850 K. The material was injected with 300 appm helium prior to irradiation (Mansur, 1987a).

It is therefore intuitive that the formation of voids (and hence the onset of macroscopic swelling) has two rate-controlling steps, and the overall swelling rate will be a function of both. The first is the rate of formation of stable bubbles (extremely rapid, due to the supersaturation of helium), and the second is the rate of transition of these bubbles into voids. Under irradiation, however, this situation is complicated by the high local densities of vacancies formed in cascades, and the subsequent potential increase in the rate of sub- or super-critical void formation (Stoller, 1997).

It is also clear that a model of this sort will exhibit both damage-rate dependent incubation effects, and incubation-period dependent transient effects. The former of these, that a lower damage-rate results in a lower incubation dose (the radiation dose received by the material before the onset of swelling (Surh et al., 2005)), arises from the increased time available for sub-critical bubbles to form (due, in part, to the greater helium concentration available to form bubbles after that increased time) before the onset of spontaneous nucleation, and hence greater number densities of growing voids at a lower dose. The latter effect, that a material with a higher incubation dose will achieve a maximum swelling rate more abruptly than a material with a lower incubation dose (Garner et al., 2000) can be explained in similar terms.

In all cases, after any transition period, all steels swell at a similar rate of $\sim 1\% \text{ dpa}^{-1}$,

and there appears to be no saturation (Garner et al., 2000). At this stage, the voids are the dominant sink for vacancies, and assuming a relatively uniform ratio of vacancy production/dpa over a variety of irradiation conditions, a relatively uniform swelling rate is expected. One reason that bcc (*e.g.* ferritic/martensitic) steels are preferred for fusion power use over fcc (*e.g.* stainless) steels is that bcc steels have longer incubation periods than fcc steels.

7.3.2 High pressure gas law models

Modifications of the theory have been carried out to apply high-pressure gas laws such as the Van der Waals or hard sphere equations of state (Mansur, 1987b; Stoller and Odette, 1985). These corrections somewhat modify the critical bubble size n^* (by a few percent) and gas content x^* (by up to 50%). However, since vacancies generally arrive at bubbles at a slower rate than helium atoms, it is vacancy arrivals which are the overall rate-controlling step in the transition from bubbles to voids, provided there are sufficient He atoms available to fill the bubble, and excluding the possibility of clusters of helium atoms displacing iron atoms from the matrix and creating additional Frenkel pairs. The critical gas content per bubble becomes important when there are more nucleation sites available than can be “filled” by the available helium.

7.4 Creating swelling-resistant steels

Swelling can be restricted in a number of ways:

1. by decreasing the quantity of helium produced in a material, through avoidance of alloying elements such as boron or nickel, or through shielding to absorb or decrease the energy of incident neutrons and reduce the chance of transmutation
2. by increasing the microstructural sink density, to reduce the rate at which helium reaches bubbles and to delay the onset of spontaneous nucleation
3. by increasing the number of potential nucleation sites in a material, to disperse the available helium among more bubbles and therefore decrease the number of helium atoms per bubble.

7.4 Creating swelling-resistant steels

The first of these requires careful control of impurities during alloy production – a requirement of satisfactory low-activation steels anyway – or unwarranted modification of first-wall design. The second can be accomplished through heat treatments or deformation, or simultaneously with the third through alloying with elements which result in a very fine precipitate dispersion during irradiation. Such a dispersion can also be introduced during steel manufacture by mechanical alloying. This microstructure has the added benefit that helium is held at these precipitates and kept away from grain boundaries, where the formation of cavities can cause high-temperature embrittlement (Schroeder et al., 1985).

Through combinations of these approaches, austenitic Fe-Cr-Ni base alloys – which otherwise exhibit very high swelling, can have swelling delayed to more than 100 dpa and several thousand appm helium (Mansur et al., 1986). It is therefore expected that such modifications would apply equally to ferritic alloys and other candidate fusion reactor materials.

Chapter 8

Designing optimised experiments for IFMIF

8.1 Introduction

There are various key unresolved issues in the modelling of irradiation effects on materials for use in future fusion power plants (Bloom et al., 2004). One of these is the extrapolation of models – based on observations of materials irradiated in current lower-energy facilities and fission reactors – to the high-energy, high-dose fusion-relevant regime. The proposed International Fusion Materials Irradiation Facility (IFMIF), when built, will provide suitable experimental facilities for testing the predictions of mechanistic models on candidate power plant materials by simulating a fusion irradiation spectrum (Möslang et al., 1998). However, the available experimental volume in the high-flux region in IFMIF is ~ 0.5 litres, and the highest-damage (150 atomic displacements per atom (dpa)) experiments will last 5 years or more, meaning that experiments must be carefully chosen to make the best use of this space.

The modelling of tensile and Charpy properties for irradiated reduced-activation ferritic/martensitic (RAFMs) steels using an artificial neural network (ANN) approach was described in Chapters 5 and 6. For the purposes of this chapter, it should be noted that these models are based on a Bayesian inference method which gives as outputs not only a numerical prediction, but also the important modelling uncertainty in that prediction which helps identify regions in the input domain where knowledge is sparse.

Additionally, the training algorithm provides an estimate of the importance of an input to the network in determining the output.

The chapter focusses on two of the most promising of the RAFM steels, Eurofer (9Cr) and F82H (8Cr).

8.2 Model predictions at low dose

It is clear from model predictions (Figure 8.1) that the most rapid period of variation in the properties of an irradiated RAFM steel is during an initial low-dose period, less than 5 dpa. The rate of change of these properties with dose also depends strongly on irradiation temperature. In addition, although modelling uncertainties are generally small in the low dose regime, it should be borne in mind that these predictions are based on data gathered from non-fusion spectrum sources.

Studying the relevance accorded by the ANN to various inputs, it is also clear that the property variations are more strongly correlated with functions such as the square root of dose, rather than with the dose itself (Figure 8.2).

In combination, these effects suggest that the sampling distribution of doses chosen for the proposed experimental matrix should be weighted towards lower dose experiments with a smaller number of high-dose specimens. This will have the two-fold benefit of providing more data at an early stage – allowing the validation of models – and maximising the effective spread of the data.

In addition, the temperature region from 250 - 550°C is the region where radiation effects on the yield stress and Charpy toughness are most marked, and one that encompasses the proposed blanket temperatures of fusion plant – although a comment should be made on the possible occurrence of temper embrittlement (caused by the segregation of phosphorus to grain boundaries at temperatures around 600°C) (Shen et al., 2005). Behaviour typical of this sort of high-temperature embrittlement has been detected in the ANN models (Figure 8.3).

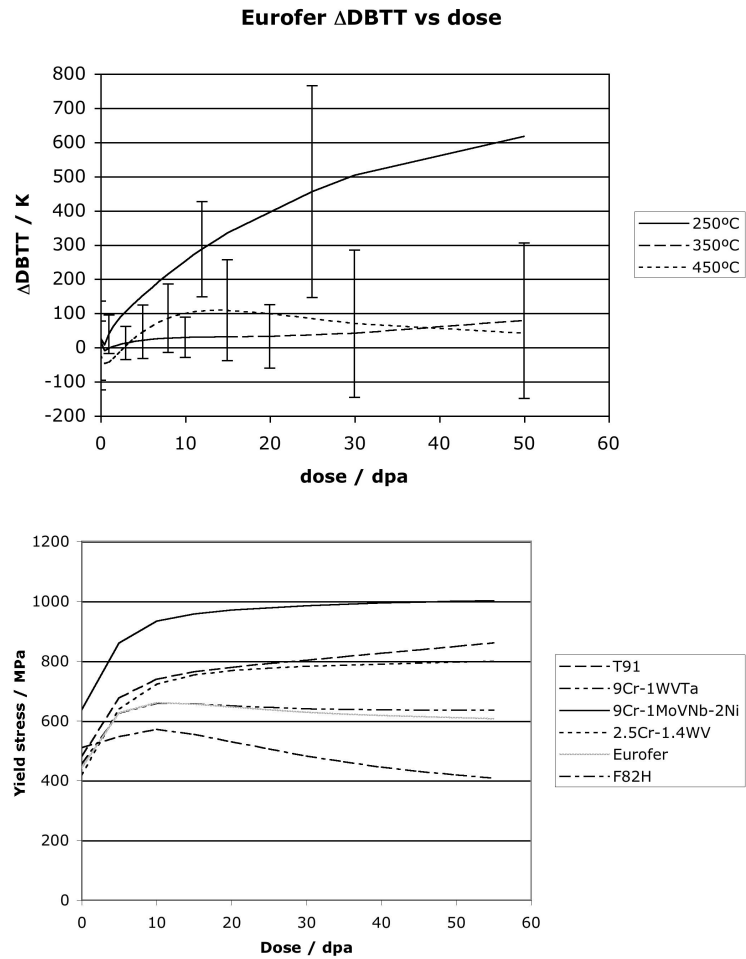


Figure 8.1: ANN model predictions for variation of (top) Δ DBTT (the change in the ductile-to-brittle-transition-temperature, Chapter 6) and (bottom) yield stress (Chapter 5) as a function of dose.

8.2 Model predictions at low dose

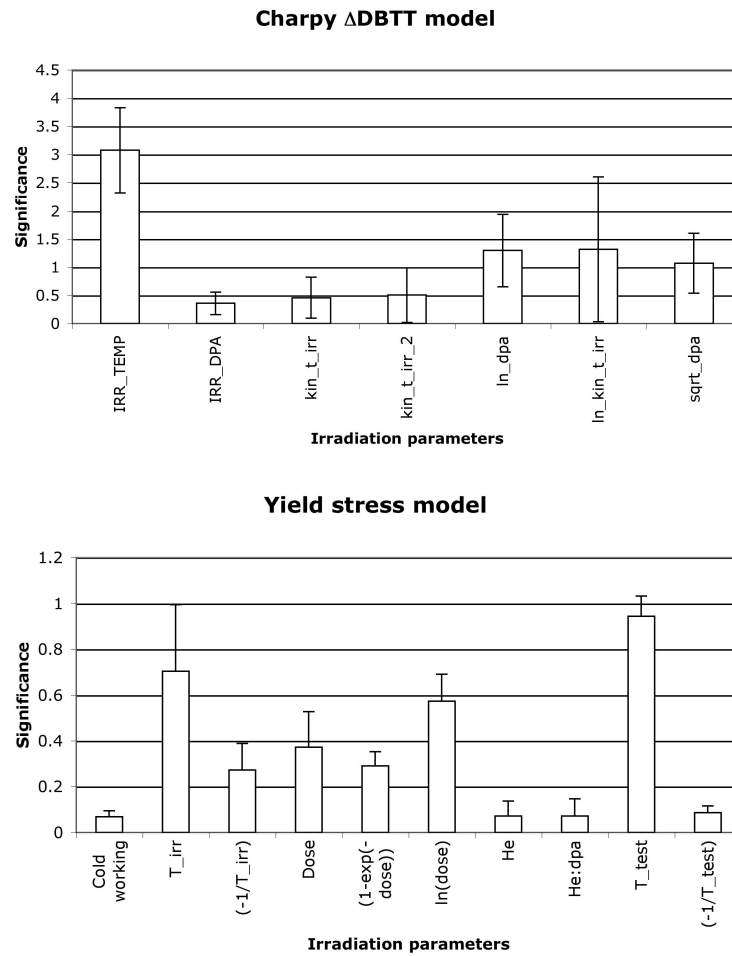


Figure 8.2: Neural network perceived significances for selected inputs to Charpy Δ DBTT (top) and yield stress (bottom) models. These significances are akin to partial correlation coefficients.

8.3 Model predictions for the fusion regime

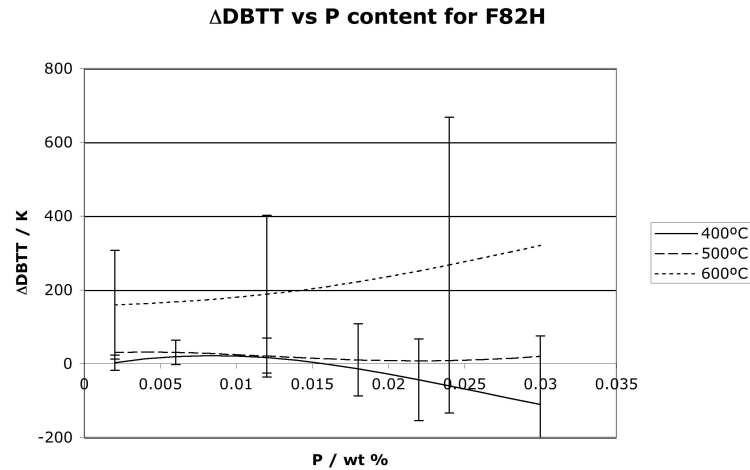


Figure 8.3: Model predictions for an F82H-based alloy with varying phosphorus content, irradiated to 2.5 dpa at different temperatures. The markedly different behaviour at 600°C is characteristic of temper embrittlement.

8.3 Model predictions for the fusion regime

It can be seen (Figures 8.1 and 8.4) that the ANN model predictions become increasingly uncertain at high dose (particularly above 50 dpa). This is accompanied by a range of predicted behaviours, including saturation and recovery, particularly at elevated (>500°C) irradiation temperatures. Both effects are physically justifiable (in terms of the formation and subsequent annealing of extended microstructural defects such as dislocation loops *etc.*), but the present data do not allow the two effects to be separated and so allow us to predict which will dominate under fusion-spectrum irradiation. It will therefore be useful to maintain a number of higher-dose experimental points to “pin” such ANN models and hence reduce the modelling uncertainties.

8.4 Summary and conclusions

Examination of the trends and associated outputs from the models described in previous chapters leads to the following conclusions:

1. Having demonstrated that higher temperature ($T > 550^\circ\text{C}$) effects such as temper

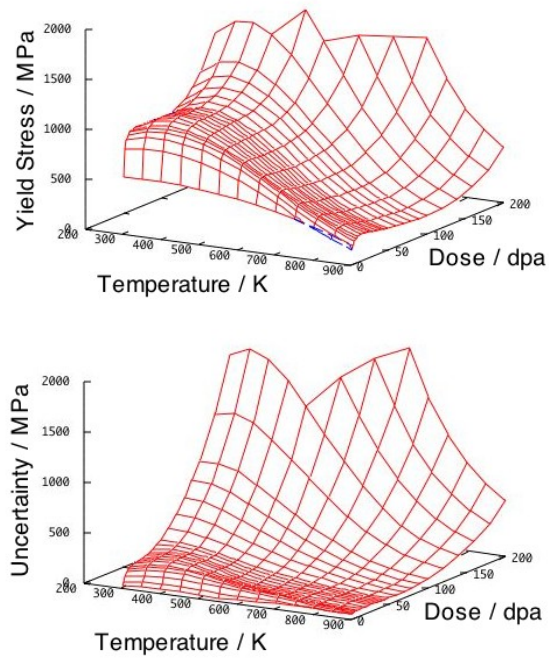


Figure 8.4: Hardening prediction (and associated modelling uncertainty) for Eurofer as a function of temperature ($T_i = T_{\text{test}}$) and dose.

8.4 Summary and conclusions

embrittlement are present in the data, the IFMIF experimental regime should extend to at least 600°C in order to cover these effects.

2. Target experimental doses should be chosen to reflect underlying physics, such as the expected dependence of material property changes on $\sqrt{\text{dpa}}$. In this case, picking eight equally spaced target experimental doses (for each temperature, as per Möslang (2005)) between 5 and 150 dpa gives 5, 13, 26, 43, 63, 88, 117, and 150 dpa.
3. The models show the sensitivity of DBTT and YS to all the inputs, highlighting the need to report experimental data as fully as possible.

These conclusions are only concerned with the optimisation of the experimental matrix – it is also of concern, as discussed previously, that the experimental materials are optimised.

Future work will include using these models to explore the significance of other physically significant inputs (such as the commonly used – for heat treatments such as tempering – kinetic time: $t \exp\left(\frac{-Q}{kT}\right)$). In the case of irradiation damage the substitute (dose) $\exp\left(\frac{-Q}{kT}\right)$ is suggested, where Q is a suitable activation energy for microstructural evolution) to further refine the experimental matrix with respect to dose/temperature interaction. Further work also includes the incorporation of what data there is available on helium effects into the models to quantify this important additional factor.

Chapter 9

Summary

9.1 Neural network models and radiation damage

Neural network models were created to estimate radiation damage effects on the yield stress, and Charpy ductile-to-brittle transition temperature and upper shelf energy for sub-size specimens in reduced activation ferritic/martensitic steels. These models successfully captured known relationships and revealed some further trends.

It is clear, therefore, that such models can be usefully applied to the complex problem of material property changes during irradiation damage. The models can then be interrogated to find trends in the data and to assess the contributions of a variety of input parameters. This feature, in particular, allows different physical hypotheses to be tested against the data.

This is the first time that properly qualified predictions (*i.e.* with uncertainty estimates) have been made of irradiated property changes based on the full range of available experimental parameters, rather than simplified models. The models also permit the relative importance of individual inputs to be assessed. The combination of this assessment with the estimated uncertainty allows optimally-informative experiments to be recommended, as well as allowing the testing of postulated physics.

A further application of neural network models is the optimisation of the input parameters to achieve a desired output. This has particular relevance to the engineering of fusion reactors, which will require novel alloys which must be designed using limited experimental data. The data are limited due to the existence of few suitable

experimental facilities – and currently none which are tailored to give a near-fusion irradiation spectrum.

In order to reduce noise in the available data, it is important that experimental data are reported as completely as possible, and that this information is incorporated into the training data for future neural network models. The heat treatment and chemical composition (including any impurities) are important factors in an alloy's response to irradiation, but crucially the dose, dose rate, irradiation time and irradiation energy are reported as a single dpa figure when they may have interacting effects which are too complex to summarise with one number.

9.2 Optimisation of steel compositions

Genetic algorithm methods were applied to the neural network models described above to optimise alloy composition for irradiation hardening and embrittlement resistance. The algorithm inputs are a target value and permitted uncertainty, which prevents the identification of “perfect” results which have a very large uncertainty.

Based on the results of the genetic algorithm, a composition of 0.11C-9.8Cr-1W-0.5Mo-0.24Ta-0.2V-0.2Si-0.1Mn (wt %) can tentatively be suggested. This is based on a heat treatment of one hour normalising at 1050°C and two hours tempering at 750°C, although further work may additionally identify an improved heat treatment as well. This composition is similar to the Optifer series alloys I and V, although with higher Mo (none in the Optifer alloys) and lower Mn (0.5 and 0.4 wt% in Optifer I and V respectively) (Schäfer, 2000). Such an alloy should, assuming the models are accurate, exhibit good hardening and embrittlement resistance and hence improved fusion first-wall properties.

9.3 Alloy design for a fusion power plant

It seems clear that, in steels at least, microstructure is the dominant controlling factor in swelling behaviour. In order to delay the onset of swelling as much as possible, a very high density of nucleation sites for helium bubbles is required. This can be introduced by alloying or cold-working. It is therefore suggested that an ODS-type steel,

of a matrix composition optimised as described earlier, would provide good swelling resistance, as well as improved high-temperature properties over a basic RAFM steel. This may require additional engineering to avoid or protect welds in the final plant design, as welding of ODS steels dramatically degrades the properties.

These recommendations comprise a novel alloy proposition, and experiments to validate the performance of such an alloy are required.

The maturity of RAFM steels provides a useful base from which to design optimised steels, as described in this work. However, it is not known how stable ODS microstructures will be at high damage levels, and it is difficult to weld these steels whilst preserving their microstructure. It seems certain that, while a RAFM-based material may be suitable for first-generation fusion power plants such as DEMO, more efficient plant designs will require different materials again. It is anticipated that the techniques described in this work can also be profitably applied to the problems of radiation damage effects in such materials and so will continue to provide guidance towards the engineering of future fusion materials.

9.4 Database issues

The databases of irradiated RAFM steel properties used in this work were assembled from published results, and are currently incomplete. The lack of consistent experimental reporting meant that a number of potentially important variables had to be excluded as network inputs (at the cost of increased noise in the output) in order to maintain a reasonable number of data on which to train the networks. This database now provides a platform on which to build a more extensive and complete set of data for future, more accurate models.

9.5 Further work

The current materials databases should be expanded as new experimental results become available. Irradiation parameters such as damage rate and irradiation time should be incorporated, and potential physics should also be included through suitable combinations of inputs. It is anticipated that these steps will markedly lower the noise

on the data. Further inclusion of high-damage-level data should improve predictions in the fusion-relevant regime. This will be ongoing, long-term work, as such well-populated databases are also required to satisfy licensing requirements to construct a fusion power plant.

In order to fully optimise a possible alloy for multiple material properties, it is intended that the genetic algorithm code be rewritten to allow multiple targets and use multiple predictive models. A steel which exhibits little hardening after irradiation to 150 dpa may have large intermediate hardening, and it would be of benefit to force the genetic algorithm to take behaviour at multiple damage levels into account. In addition, a steel optimised for resistance to embrittlement may exhibit poor hardening properties, or vice versa – with the best balance achieved somewhere in between. It will therefore also be necessary to define an overall merit index to be optimised once this work is done.

Finally, this work must be validated experimentally. Ideally, IFMIF will be available within a reasonable timescale to validate materials for use in DEMO. In the meantime, it is hoped experimental time can be found to fabricate and test alloys based on the recommendations made in this current work.

Appendix A

Probability of a coin toss

We toss a coin N times, obtaining a sequence of H heads and $(N - H)$ tails. We want to know the probability of obtaining a head (h) on the $(N + 1)$ th toss. The probability of getting a head on a toss is denoted u .

Thus

$$P((N + 1) = h|H, N) = \int_0^1 P((N + 1) = h|u, H, N) P(u|H, N) du \quad (\text{A.1})$$

by the sum rule. $P((N + 1) = h|u, H, N) = u$ by definition, so

$$P((N + 1) = h|H, N) = \int_0^1 u P(u|H, N) du \quad (\text{A.2})$$

$$= \int_0^1 u \frac{P(u)P(H|u, N)}{P(H|N)} du \quad (\text{A.3})$$

by the product rule. Assuming a uniform prior on u , $P(u) = 1$, so

$$P((N + 1) = h|H, N) = \int_0^1 u \frac{\binom{N}{H} u^H (1 - u)^{(N-H)}}{P(H|N)} du \quad (\text{A.4})$$

$$= \frac{\binom{N}{H}}{P(H|N)} \int_0^1 u^{(H+1)} (1 - u)^{(N-H)} du \quad (\text{A.5})$$

Using the beta integral

$$\int_0^1 p^{F_a} (1 - p)^{F_b} dp = \frac{F_a! F_b!}{(F_a + F_b + 1)!} \quad (\text{A.6})$$

we get

$$P((N + 1) = h|H, N) = \frac{\binom{N}{H}}{P(H|N)} \frac{(H + 1)!(N - H)!}{(N + 2)!} \quad (\text{A.7})$$

$P(H|N)$ is the normalising constant, the marginal probability of H .

$$P(H|N) = \int_0^1 P(H|u, N) du \quad (\text{A.8})$$

$$= \int_0^1 \binom{N}{H} u^H (1 - u)^{(N-H)} du \quad (\text{A.9})$$

$$= \binom{N}{H} \frac{H!(N - H)!}{(N + 1)!} \quad (\text{A.10})$$

Substituting back into Equation A.7 and cancelling $\binom{N}{H}$ gives

$$P((N + 1) = h|H, N) = \frac{(N + 1)!}{H!(N - H)!} \frac{(H + 1)!(N - H)!}{(N + 2)!} \quad (\text{A.11})$$

$$= \frac{H + 1}{N + 2} \quad (\text{A.12})$$

Appendix B

Sammon mapping code for *Mathematica*

This code takes in a dataset (“FileName.tsv” – this file is `tab` delimited and consists of input data in columns with the final column being the output variable; the first row is assumed to be labels and is discarded) using the `Import` function and calculates the minimum Sammon mapping error on progressively adding inputs to the output. The control parameter is `enddim`, which tells the code how many dimensions to add. The program will then normalise all the inputs, calculate the Sammon mapping error for mapping to the output alone, and then for 1 additional dimension, 2 additional dimensions, and so on.

While it is running, the reports consist of the number of dimensions currently being used and the calculation step for that dimensionality. Once the calculations have been done, an additional report line gives the dimensions with the smallest error, and the error using those dimensions.

Once finished, the program will plot a graph of dimensions vs. error.

The `Main program` section should be run initially. If additional numbers of dimensions are desired, the extra code below can be run with an appropriate value for `enddim`.

```

<< Graphics`Graphics3D`
<< DiscreteMath`Combinatorica`

- Collect data from file
- notes:
    input columns with zero variation (all the same
    values) will cause infinities during normalisation
    duplicate points in the dataset will cause infinities
    during calculations these should be detected, but
    this will waste time
    CHECK INPUT DATABASE

data=Delete[Import["FileName.tsv","TSV"],1];
len=Length[data]
width=Length[data[[1]]]

- Normalise data and calculate vector spacings in
  N-space (this only has to be done the first time)

maximum[x_]:=Max[data[[All,x]]]
minimum[x_]:=Min[data[[All,x]]]
checkrange=Table[0,{width}];
Do[checkrange[[i]]=Sqrt[maximum[i]-minimum[i]},{i,width}]
If[Min[checkrange]==0,
  "Error! Check ranges of inputs!",
  data2=Table[(data[[i]][[j]]-minimum[j])/(maximum[j]-
    minimum[j])-0.5,{i,1,len},{j,1,width}];
  dataorigdist=Table[Sqrt[Sum[(data2[[i]][[j]]-
    data2[[k]][[j]])^2,{j,1,width}]],{i,1,(len-1)},
    {k,i+1,len}];
  origdist=Sum[Apply[Plus,dataorigdist[[i]]],
    {i,1,(len-1)}];
]
If[Min[dataorigdist][Equal]0,

```

```

    "You have duplicate points! Please remove them!",
    "Okay!"]

- Main programme - calculate minimum errors and plot
  graph

startdim = 1;
enddim = 8;
Clear[sammonmin]; Clear[sammonmin2];
totry = Range[width];
sammon = Table[0, {Length[totry]}];
positiony = Length[totry];
Print[positiony];
Clear[data3]; Clear[datanewdist];
data3 = Table[Part[data2[[i]], totry[[positiony]]],
  {i, 1, len}];
datanewdist = Table[Sqrt[(data3[[i]] - data3[[k]])^2],
  {i, 1, (len - 1)}, {k, i + 1, len}];
distdiff = (1/origdist)((dataorigdist - datanewdist)^2/
  dataorigdist);
sammon[[positiony]] = Sum[Apply[Plus, distdiff[[i]]],
  {i, 1, (len - 1)}];
sammonmin = {{Length[totry]}};
sammonmin2 = {sammon[[Length[totry]]]};
Print[sammonmin, "    ", sammonmin2];
pointx = 2;
While[pointx < enddim,
  totry = Complement[Range[width], Last[sammonmin]];
  sammon = Table[0, {Length[totry]}];
  positiony = 1;
  Do[
    Print[pointx, "    ", positiony];
    Clear[data3]; Clear[datanewdist];
    data3 = Table[Part[data2[[i]],

```

```

Sort[Append[Last[sammonmin],
totry[[positiony]]]], {i, 1, len}};
datanewdist = Table[Sqrt[Sum[(data3[[i]][[j]] -
data3[[k]][[j]])^2, {j, 1, Length[
data3[[1]]}]], {i, 1, (len - 1)},
{k, i + 1, len}];
distdiff = (1/origdist)((dataorigdist -
datanewdist)^2/dataorigdist);
sammon[[positiony]] = Sum[Apply[Plus, distdiff[[i]]],
{i, 1, (len - 1)}];
positiony = positiony + 1,
{Length[totry]}}];
sammonorder = Ordering[sammon];
choice = Sort[Append[Last[sammonmin],
Part[totry, sammonorder[[1]]]]];
sammonmin = Append[sammonmin, choice];
sammonmin2 = Append[sammonmin2, Min[sammon]];
Print[sammonmin, " ", sammonmin2];
pointx = pointx + 1
]
ListPlot[sammonmin2, PlotJoined -> True]
sammonmin
sammonmin2

```

- To calculate additional dimensions

```

enddim = 12;
While[pointx < enddim,
totry = Complement[Range[width], Last[sammonmin]];
sammon = Table[0, {Length[totry]};
positiony = 1;
Do[
Print[pointx, " ", positiony];
Clear[data3]; Clear[datanewdist];

```

```

data3 = Table[Part[data2[[i]],
  Sort[Append[Last[sammonmin],
  tottry[[positiony]]]], {i, 1, len}];
datanewdist = Table[Sqrt[Sum[(data3[[i]][[j]] -
  data3[[k]][[j]])^2, {j, 1, Length[data3[[1]]}]],
  {i, 1, (len - 1)}, {k, i + 1, len}];
distdiff = (1/origdist)((dataorigdist -
  datanewdist)^2/dataorigdist);
sammon[[positiony]] = Sum[Apply[Plus, distdiff[[i]],
  {i, 1, (len - 1)}];
positiony = positiony + 1,
{Length[tottry]};
sammonorder = Ordering[sammon];
choice = Sort[Append[Last[sammonmin], Part[tottry,
  sammonorder[[1]]]]];
sammonmin = Append[sammonmin, choice];
sammonmin2 = Append[sammonmin2, Min[sammon]];
Print[sammonmin, " ", sammonmin2];
pointx = pointx + 1
]

```

- Report optimum dimensions and Sammon mapping errors and replot graph

```

sammonmin
sammonmin2
ListPlot[sammonmin2, PlotJoined\ [Rule] True,
  AxesOrigin\ [Rule] {0, 0}]

```

Appendix C

Yield stress model database references

This is a complete list of the references used to construct the database for the irradiation hardening model described in Chapter 5.

F Abe, T Noda, H Araki, and M Okada, Development of reduced-activation martensitic 9Cr steels for fusion reactor. *Journal of Nuclear Science and Technology*, 31(4): 279 - 292, 1994.

A Alamo, M Horsten, X Averty, E I Materna-Morris, M Rieth, and J C Brachet, Mechanical behavior of reduced-activation and conventional martensitic steels after neutron irradiation in the range 250-450 degrees C. *Journal of Nuclear Materials*, 283: 353 - 357, 2000.

N Baluc, R Schaublin, C Bailat, F Paschoud, and M Victoria, The mechanical properties and microstructure of the OPTIMAX series of low-activation ferritic-martensitic steels. *Journal of Nuclear Materials*, 283: 731 - 735, 2000.

I Belianov and P Marmy, The effect of low dose irradiation on the impact fracture energy and tensile properties of pure iron and two ferritic martensitic steels. *Journal of Nuclear Materials*, 263: 1259 - 1263, 1998.

Y Dai, X J Jia, and K Farrell, Mechanical properties of modified 9Cr-1Mo (T91) irradiated at ≤ 300 degrees C in SINQ Target-3. *Journal of Nuclear Materials*, 318: 192 - 199, 2003.

Y Dai, S A Maloy, G S Bauer, and W F Sommer, Mechanical properties and microstructure in low-activation martensitic steels F82H and Optimax after 800-MeV proton irradiation. *Journal of Nuclear Materials*, 283: 513 - 517, 2000.

K Farrell and T S Byun, Tensile properties of candidate SNS target container materials after proton and neutron irradiation in the LANSCE accelerator. *Journal of Nuclear Materials*, 296: 129 - 138, 2001.

K Farrell and T S Byun, Tensile properties of ferritic/martensitic steels irradiated in HFIR, and comparison with spallation irradiation data. *Journal of Nuclear Materials*, 318: 274 - 282, 2003.

P Fernandez, A M Lancha, J Lapena, and M Hernandez-Mayoral, Metallurgical characterization of the reduced activation ferritic/martensitic steel Eurofer97 on as-received condition. *Fusion Engineering and Design*, 58 - 59: 787 - 792, 2001.

I V Gorynin, V V Rybin, I P Kursevich, A N Lapin, E V Nesterova, and E Y Klepikov, Effect of heat treatment and irradiation temperature on mechanical properties and structure of reduced-activation Cr-W-V steels of bainitic, martensitic, and martensitic-ferritic classes. *Journal of Nuclear Materials*, 283: 465 - 469, 2000.

J Henry, X Averty, Y Dai, P Lamagnere, J P Pizzanelli, J J Espinas, and P Wident, Tensile properties of 9Cr-1Mo martensitic steel irradiated with high energy protons and neutrons. *Journal of Nuclear Materials*, 318: 215 - 227, 2003.

J Henry, M H Mathon, and P Jung, Microstructural analysis of 9% Cr martensitic steels containing 0.5% at.% helium. *Journal of Nuclear Materials*, 318: 249 - 259, 2003

P Jung, J Henry, J Chen, and J C Brachet, Effect of implanted helium on tensile properties and hardness of 9% Cr martensitic stainless steels. *Journal of Nuclear Materials*, 318: 241 - 248, 2003.

R Kasada, A Kimura, H Matsui, M Hasegawa, and M Narui, Effects of varying temperature irradiation on the neutron irradiation hardening of reduced-activation 9Cr-2W martensitic steels. *Journal of Nuclear Materials*, 272: 360 - 364, 1999.

R Kasada, A Kimura, H Matsui, and M Narui, Enhancement of irradiation hardening by nickel addition in the reduced-activation 9Cr-2W martensitic steel. *Journal of Nuclear Materials*, 263: 1199 - 1203, 1998.

A Kimura, T Morimura, M Narui, and H Matsui, Irradiation hardening of reduced activation martensitic steels. *Journal of Nuclear Materials*, 237: 319 - 325, 1996.

R L Klueh, Irradiation effects of ferritic steels; effect of composition. *Journal of Nuclear Materials*, 179: 728 - 732, 1991.

R L Klueh and D J Alexander. Tensile and charpy impact properties of irradiated reduced-activation ferritic steels. In *Effects of radiation on materials: 18th international symposium*, ASTM, 1999.

R L Klueh, D J Alexander, and M Rieth, The effect of tantalum on the mechanical properties of a 9Cr-2W-0.25V-0.07Ta-0.1C steel. *Journal of Nuclear Materials* 273(2): 146 - 154, 1999.

R L Klueh, D J Alexander, and M A Sokolov, Effect of chromium, tungsten, tantalum, and boron on mechanical properties of 59CrWVTaB steels. *Journal of Nuclear Materials*, 304(2-3): 139 - 152, 2002.

R L Klueh, J J Kai, and D J Alexander, Microstructure mechanical-properties correlation of irradiated conventional and reduced-activation martensitic steels. *Journal of Nuclear Materials*, 225: 175 - 186, 1995.

R L Klueh and P J Maziasz, Effect of irradiation in HFIR on tensile properties of Cr-Mo steels. *Journal of Nuclear Materials*, 187: 43 - 54, 1992.

R L Klueh, M Sokolov, K Shiba, Y Miwa, and J P Robertson, Embrittlement of reduced-activation ferritic/martensitic steels irradiated in HFIR at 300 degrees C and 400 degrees C. *Journal of Nuclear Materials*, 283: 478 - 482, 2000.

R L Klueh and J M Vitek, Elevated-temperature tensile properties of irradiated 9Cr-1MoVNb steel. *Journal of Nuclear Materials*, 132: 27 - 31, 1985.

R L Klueh and J M Vitek, Fluence and Helium effects on the tensile properties of ferritic steels at low temperatures. *Journal of Nuclear Materials*, 161: 13 - 23, 1989.

Y Kohno, A Kohyama, T Hirose, M L Hamilton, and M Narui, Mechanical property changes of low activation ferritic martensitic steels after neutron irradiation. *Journal of Nuclear Materials*, 272: 145 - 150, 1999.

A Kohyama, H Matsui, K Hamada, and H Simidzu, Material responses of ferritic steels by 14MeV neutron bombardments at 20K and 300K. *Journal of Nuclear Materials*, 155: 896 - 901, 1988.

H Kurishita, H Kayano, M Narui, A Kimura, M L Hamilton, and D S Gelles, Tensile properties of reduced-activation Fe-9Cr-2W steels after FFTF irradiation. *Journal of Nuclear Materials*, 215: 730 - 735, 1994.

R Lindau, A Möslang, D Preininger, M Rieth, and H D Rohrig, Influence of helium on impact properties of reduced-activation ferritic-martensitic Cr-steels. *Journal of Nuclear Materials*, 272: 450 - 454, 1999.

E Lucon, M Decreton, and E van Walle, Mechanical Characterisation of EUROFER97 irradiated (0.32 dpa, 300 degrees C). *Fusion Engineering and Design*, 69: 373 - 377, 2003.

S A Maloy, M R James, G Willcutt, W F Sommer, M Sokolov, L L Snead, M L Hamilton, and F Garner, The mechanical properties of 316L/304L stainless steels, Alloy718 and Mod 9Cr-1Mo after irradiation in a spallation environment. *Journal of Nuclear Materials*, 296: 119 - 128, 2001.

E I Materna-Morris, M Rieth, and K Ehrlich. Mechanical properties and microstructure of HFR-irradiated ferritic-martensitic low-activation alloys. In *Effects of radiation on materials: 19th international symposium*, ASTM, 2000.

J Rensman, J van Hoepen, J B M Bakker, R den Boef, F P van den Broek, and E D L van Essen, Tensile properties and transition behaviour of RAFM steel plate and welds irradiated up to 10 dpa at 300 degrees C. *Journal of Nuclear Materials*, 307: 245 - 249, 2002.

A F Rowcliffe, J P Robertson, R L Klueh, K Shiba, D J Alexander, M L Grossbeck, and S Jitsukawa, Fracture toughness and tensile behavior of ferritic-martensitic steels irradiated at low temperatures. *Journal of Nuclear Materials*, 263: 1275 - 1279, 1998.

J Russell Hawthorne, Fracture resistance of two ferritic stainless steels after intermediate temperature irradiation. In *Effects of radiation on materials*, 580 - 604, ASTM, 1985.

V V Rybin, I P Kursevich, and A N Lapin, Effect of neutron irradiation at low temperature on the embrittlement of the reduced-activation steels. *Journal of Nuclear Materials*, 263: 1324 - 1328, 1998.

J L Séran, A Alamo, A Maillard, H Touron, J C Brachet, P Dubuisson, and O Rabouille, Preirradiation and postirradiation mechanical properties of ferritic-martensitic steels for fusion applications – EM10 base metal and EM10/EM10 welds. *Journal of Nuclear Materials*, 215: 588 - 593, 1994.

J L Séran, V Levy, P Dubuisson, D Gilbon, A Maillard, A Fissolo, H Touron, R Cauvin, A Chalony, and E Leboulbin, Behavior under neutron-irradiation of the 15-15Ti and EM10 steels used as standard materials of the Phenix fuel subassembly. In *Effects of Radiation on Materials: 15th International Symposium*, ASTM, 1992.

V K Shamardin, V N Golovanov, T M Bulanova, A Povstyanko, A E Fedoseev, Z E Ostrovsky, and Y D Goncharenko, Evolution of the mechanical properties and microstructure of ferritic-martensitic steels irradiated in the BOR-60 reactor. *Journal of Nuclear Materials*, 307: 229 - 235, 2003.

K Shiba, A Hishinuma, A Toyama, and K Masamura, Properties of the reduced activation ferritic steels F82H IEA heat. *JAERI-Tech 97-038*, JAERI, 1997.

T Shibayama, A Kimura, and H Kayano, The effect of small additional elements on the precipitation of reduced activation Fe-9Cr-2W steels. *Journal of Nuclear Materials*, 237: 270 - 275, 1996.

P Spatig, R Schaublin, S Gyger, and M Victoria, Evolution of the mechanical properties of the F82H ferritic/martensitic steel after 590 MeV proton irradiation. *Journal of Nuclear Materials*, 263: 1345 - 1349, 1998.

E van Osch, M Horsten, G E Lucas, and G R Odette, Mechanical properties of four 7-9% Cr reduced activation martensitic steels after 2.5 dpa, 300 degrees C irradiation. In *Effects of radiation on materials: 19th international symposium*, ASTM, 2000.

E van Osch, J B M Bakker, R den Boef, and J Rensman, Tensile properties of 2.5 dpa 300°C neutron irradiated RAFM plate, powder HIP and EB and TIG weld. *NRG-Petten-20023/99.26704/P* NRG-Petten, 2002.

References

- F Abe. Strength and toughness of tungsten-stabilized ferritic/martensitic steels for fusion reactor. In A Kohyama, H Matsui, S Tanaka, and H Takahashi, editors, *Materials for Advanced Energy Systems & Fission and Fusion Engineering '94*, pages 319 – 324, 1994. 55, 57
- F Abe and H Kayano. Effect of specimen size on ductile to brittle transition behaviour of martensitic 9Cr steels after various heat treatments. *Journal of Nuclear Materials*, 232:44 – 51, 1996. 60, 66
- F Abe, Noda Tetsuji, Araki Hiroshi, and Okada Masatoshi. Development of reduced-activation martensitic 9Cr steels for fusion reactor. *Journal of Nuclear Science And Technology*, 4(31):279 – 292, 1994. 7, 57
- A Alamo, J C Brachet, A Castaing, C Lepoittevin, and F Barcelo. Physical metallurgy and mechanical behaviour of FeCrWTaV low activation martensitic steels: Effects of chemical composition. *Journal of Nuclear Materials*, 258 - 263:1228 – 1235, 1998. 57
- A Alamo, V Lambard, X Averty, and M H Mathon. Assessment of ODS-14%Cr ferritic alloy for high temperature applications. *Journal of Nuclear Materials*, 329 - 333:333 – 337, 2004. 13
- D J Bacon, F Gao, and Yu N Osetsky. The primary damage state in fcc, bcc and hcp metals as seen in molecular dynamics simulations. *Journal of Nuclear Materials*, 276:1 – 12, 2000. 9
- V Barabash. Role and contribution of ITER in research of materials and reactor components. *Journal of Nuclear Materials*, 329 - 333:156 – 160, 2004. 6, 14

REFERENCES

- D E Beck. A new interatomic potential function for helium. *Molecular Physics*, 14(4): 311 – 315, 1968. 92
- A L Bement. Fundamental materials problems in nuclear reactors. In *2nd International Conference on the Strength of Metals and Alloys*, volume 2, pages 693 – 728, 1970. 35, 36
- H K D H Bhadeshia. Application of first-order quasichemical theory to transformations in steels. *Metal Science*, 16:167 – 169, 1982. 91
- H K D H Bhadeshia. Quasichemical model for interstitial solutions. *Materials Science And Technology*, 14:273 – 276, 1998. 92
- H K D H Bhadeshia. Neural networks in materials science. *ISIJ International*, 39(10): 966 – 979, 1999. 18, 38
- C M Bishop. Neural networks and their applications. *Review of Scientific Instruments*, 65(6):1803 – 1832, 1994. 25
- C M Bishop. *Neural Networks For Pattern Recognition*. Clarendon Press, Oxford, 1 edition, 1995. 18
- E E Bloom. The challenge of developing structural materials for fusion power systems. *Journal of Nuclear Materials*, 258 - 263:7 – 17, 1998. 8
- E E Bloom, S J Zinkle, and F W Wiffen. Materials to deliver the promise of fusion power - progress and challenges. *Journal of Nuclear Materials*, 329 - 333:12 – 19, 2004. 4, 11, 14, 104
- L V Boccaccini, L Giancarli, G Janeschitz, S Hermsmeyer, Y Poitevin, A Cardella, and E Diegele. Materials and design of the European DEMO blankets. *Journal of Nuclear Materials*, 329 - 333:148 – 155, 2004. 13
- H Bolt, V Barabash, G Federici, J Linke, A Loarte, J Roth, and K Sato. Plasma facing and high heat flux materials - needs for ITER and beyond. *Journal of Nuclear Materials*, 307 - 311:43 – 52, 2002. 6

REFERENCES

- A D Brailsford. Vacancy dislocation loop microstructure formed during heavy-particle bombardment. *Journal of Nuclear Materials*, 84:245 – 268, 1979. 37
- A D Brailsford and R Bullough. The rate theory of swelling due to void growth in irradiated metals. *Journal of Nuclear Materials*, 44:121 – 135, 1972. 90
- A D Brailsford and R Bullough. The theory of sink strengths. *Philosophical Transactions of the Royal Society: A*, 302(1465):87 – 137, 1981. 99
- R Bullough and T M Quigley. Dislocation sink strengths for the rate theory of irradiation damage. *Journal of Nuclear Materials*, 103 - 104:1397 – 1402, 1981. 36
- R Bullough, B L Eyre, and G L Kulcinski. A systematic approach to the radiation damage problem. *Journal of Nuclear Materials*, 68:168 – 178, 1977. 91
- G J Butterworth and L Giancarli. Some radiological limitations on the compositions of low-activation materials for power reactors. *Journal of Nuclear Materials*, 155 - 157:575 – 580, 1988. 8, 57
- T S Byun and K Farrell. Irradiation hardening behavior of polycrystalline metals after low temperature irradiation. *Journal of Nuclear Materials*, 326:86 – 96, 2004. 38
- M Á Carreira-Perpiñán. A review of dimensional reduction techniques. Technical Report CS-96-09, University of Sheffield, December 2002. 25
- R G Carter and N Soneda. In *EPRI-CRIEPI Workshop on dose rate effects in RPV materials*, EPRI 1006981, 2002. 39
- M J Caturla, N Soneda, E Alonso, B D Wirth, T Díaz de la Rubia, and J M Perlado. Comparative study of radiation damage accumulation in Cu and Fe. *Journal of Nuclear Materials*, 276:13 – 21, 2000. 9, 10
- C Cawthorne and E J Fulton. Voids in irradiated stainless steel. *Nature*, 216:575 – 576, 1967. 89
- R Chaouadi and R Gérard. Copper precipitate hardening of irradiated RPV materials and implications on the superposition law and re-irradiation kinetics. *Journal of Nuclear Materials*, 345:65 – 74, 2005. 35

REFERENCES

- J M Chen, T Muroga, S Y Qiu, T Nagasaka, W G Huang, M J Tu, Y Chen, Y Xu, and Z Y Xu. The development of advanced vanadium alloys for fusion applications. *Journal of Nuclear Materials*, 329 - 333:401 – 405, 2004. 11
- H S Cho, A Kimura, S Ukai, and M Fujiwara. Corrosion properties of oxide dispersion strengthened steels in super-critical water environment. *Journal of Nuclear Materials*, 329 - 333:387 – 391, 2004. 13
- J W Christian. *The theory of transformations in metals and alloys: Part I*. Pergamon, 3 edition, 2002. 96
- C W Corti, P Cotterill, and G A Fitzpatrick. The evaluation of the interparticle spacing in dispersion alloys. *International Metallurgical Reviews*, 19:77, 1974. 35
- A Cottrell. Annealing a nuclear reactor: an adventure in solid-state engineering. *Journal of Nuclear Materials*, 100:64 – 66, 1981. 37
- A Delorme. Genetic algorithm for optimization of mechanical properties. Technical report, University of Cambridge, June 2003. 33
- K Ehrlich, E E Bloom, and T Kondo. International strategy for fusion materials development. *Journal of Nuclear Materials*, 283 - 287:79 – 88, 2000. 5
- K Farrell, T S Byun, and N Hashimoto. Deformation mode maps for tensile deformation of neutron-irradiated structural alloys. *Journal of Nuclear Materials*, 335:471 – 486, 2004. 38
- R A Forrest. The European Activation System: EASY-2001 overview. Technical report, UKAEA, 2001. 8
- F A Garner, M B Toloczko, and B H Sencer. Comparison of swelling and irradiation creep behaviour of FCC-austenitic and BCC-ferritic/martensitic alloys at high neutron exposure. *Journal of Nuclear Materials*, 276:123 – 142, 2000. 12, 101, 102
- N M Ghoniem. Theory of microstructure evolution under fusion neutron irradiation. *Journal of Nuclear Materials*, 179 - 181:99 – 104, 1991. 36

REFERENCES

- N M Ghoniem and M L Takata. A rate theory of swelling induced by helium and displacement damage in fusion reactor structural materials. *Journal of Nuclear Materials*, 105:276 – 292, 1982. 94, 98
- N M Ghoniem, S Sharafat, J M Williams, and L K Mansur. Theory of helium transport and clustering in materials under irradiation. *Journal of Nuclear Materials*, 117(96 - 105), 1983. 94
- D E Goldberg. *Genetic algorithms in search, optimisation, and machine learning*. Addison Wesley, 1989. 33
- John Price Hirth and Jens Lothe. *Theory Of Dislocations*. John Wiley & Sons, 2 edition, 1982. 35
- A Hishinuma, A Kohyama, R L Klueh, D S Gelles, W Dietz, and K Ehrlich. Current status and future R&D for reduced-activation ferritic/martensitic steels. *Journal of Nuclear Materials*, 258 - 263:193 – 204, 1998. 51
- T S Hudson, S L Dudarev, and A P Sutton. Absence of saturation of void growth in rate theory with anisotropic diffusion. *Journal of Nuclear Materials*, 307 - 311:976 – 981, 2002. 91
- R A Jameson, R Ferdinand, H Klien, J Rathke, J Sredniawski, and M Sugimoto. IFMIF accelerator facility. *Journal of Nuclear Materials*, 329 - 333:193 – 197, 2004. 14
- S Jitsukawa, A Kimura, A Kohyama, R L Klueh, A A Tavassoli, B van der Schaaf, G R Odette, J W Rensman, M Victoria, and C Petersen. Recent results of the reduced activation ferritic/martensitic steel development. *Journal of Nuclear Materials*, 329 - 333:39 – 46, 2004. 13
- R L Klueh. Irradiation hardening of ferritic steels: effect of composition. *Journal of Nuclear Materials*, 179 - 181:728 – 732, 1991. 57
- R L Klueh. Elevated temperature ferritic and martensitic steels and their application to future nuclear reactors. *International Materials Reviews*, 50(5):287 – 310, 2005. 78
- R L Klueh and D R Harris. *High-Cr ferritic and martensitic steels for nuclear applications*. ASTM, 2001. 60, 75

REFERENCES

- R L Klueh and J M Vitek. Postirradiation tensile behavior of nickel-doped ferritic steels. *Journal of Nuclear Materials*, 150:272 – 280, 1987. 37, 52
- R L Klueh, E T Cheng, M L Grossbeck, and E E Bloom. Impurity effects on reduced-activation ferritic steels developed for fusion applications. *Journal of Nuclear Materials*, 280:353 – 359, 2000. 8
- A Kohyama, A Hishinuma, D S Gelles, R L Klueh, W Dietz, and K Ehrlich. Low-activation ferritic and martensitic steels for fusion application. *Journal of Nuclear Materials*, 233 - 237:138 – 147, 1996. 51
- S Konishi. Discussion on fast track and impact on materials R&D strategy - fusion material issues for the energy systems in future. *Journal of Nuclear Materials*, 329 - 333:161 – 165, 2004. 4
- H Kurishita, T Yamamoto, M Harui, H Suwarno, T Yoshitake, Y Yano, M Yamazaki, and H Matsui. Specimen size effects on ductile-brittle transition temperature in Charpy impact testing. *Journal of Nuclear Materials*, 329 - 333:1107 – 1112, 2004. 60
- R J Kurtz, K Abe, V M Chernov, D T Hoelzer, H Matsui, T Muroga, and G R Odette. Recent progress on development of vanadium alloys for fusion. *Journal of Nuclear Materials*, 329 - 333:47 – 55, 2004. 11
- P Lako, J R Ybema, and A J Seebregts. The long term potential of fusion power in Western Europe. Technical Report ECN-C-98-071, ECN Petten, December 1998. 3
- A A Lucas. Helium in metals. *Physica B*, 127:225 – 239, 1984. 91
- D J C MacKay. *Information Theory, Inference, and Learning Algorithms*. Cambridge University Press, 1 edition, 2003. 18, 19, 21
- S Majumdar and P Smith. Treatment of irradiation effects in structural design criteria for fusion reactors. *Fusion Engineering and Design*, 41:25 – 30, 1998. 6
- M J Makin and F J Minter. Irradiation hardening in copper and nickel. *Acta Metallurgica*, 8:691 – 699, 1960. 37, 38, 51

REFERENCES

- L K Mansur. Mechanisms and kinetics of radiation effects in metals and alloys. In G R Freeman, editor, *Kinetics of Nonhomogeneous Processes*, pages 377 – 463. John Wiley & Sons, 1987a. 5, 9, 101
- L K Mansur. On accurate expressions for the critical quantities for cavity swelling. *Journal of Nuclear Materials*, 150:105 – 107, 1987b. 91, 102
- L K Mansur. Theory and experimental background on dimensional changes in irradiated alloys. *Journal of Nuclear Materials*, 216:97 – 123, 1994. 9, 36, 90
- L K Mansur and K Farrell. Mechanisms of radiation-induced degradation of reactor vessel materials. *Journal of Nuclear Materials*, 244:212 – 218, 1997. 37
- L K Mansur, E H Lee, P J Maziasz, and A P Rowcliffe. Control of helium effects in irradiated materials based on theory and experiment. *Journal of Nuclear Materials*, 141 - 143:633 – 646, 1986. 99, 103
- J W Martin. *Micromechanisms in particle-hardened alloys*. Cambridge Solid State Science Series. Cambridge University Press, Cambridge, 1 edition, 1980. 35
- R B McLellan and W W Dunn. A quasi-chemical treatment of interstitial solid solutions: its application to carbon austenite. *Journal of Physics and Chemistry of Solids*, 30:2631 – 2637, 1969. 91, 92
- M K Miller, D T Hoelzer, E A Kenik, and K F Russell. Nanometer scale precipitation in ferritic MA/ODS alloy MA957. *Journal of Nuclear Materials*, 329 - 333:338 – 341, 2004. 13, 99
- I Monnet, P Dubuisson, Y Serruys, M O Ruault, O Kaïtasov, and B Jouffrey. Microstructural investigation of the stability under irradiation of oxide dispersion strengthened ferritic steels. *Journal of Nuclear Materials*, 335(3):311 – 321, 2004. 13
- K Morishita, B D Wirth, T Díaz de la Rubia, and A Kimura. Effects of helium on radiation damage processes in iron. In *4th Pacific Rim International Conference on Advanced Materials and Processing*, pages 1383 – 1386, 2001. 93, 94, 98

REFERENCES

- A Möslang. Development of IFMIF test matrix. Technical report, Institut für Materialforschung, 2005. 14, 60, 110
- A Möslang, C Antonucci, E Daum, J R Haines, I Jitsukawa, K Noda, and S Zinkle. Overview of the IFMIF test facility. *Journal of Nuclear Materials*, 258 - 263:427 – 432, 1998. 14, 104
- S Murakami, A Miyazaki, and M Mizuno. Modeling of irradiation embrittlement of reactor pressure vessel steels. *Journal of Engineering Materials and Technology*, 122(1):60 – 66, 2000. 37, 61
- G R Odette, H J Rathbun, J W Rensman, and F P van den Broek. On the transition toughness of two RA martensitic steels in the irradiation hardening regime: a mechanism-based evaluation. *Journal of Nuclear Materials*, 307 - 311:1011 – 1015, 2002. 63
- G R Odette, T Yamamoto, H J Rathbun, M Y He, M L Hribernik, and J W Rensman. Cleavage fracture and irradiation embrittlement of fusion reactor alloys: mechanisms, multiscale models, toughness measurements and implications to structural integrity assessment. *Journal of Nuclear Materials*, 323:313 – 340, 2003. 59, 62, 63
- G R Odette, T Yamamoto, H Kishimoto, M Sokolov, P Spätig, W J Yang, J W Rensman, and G E Lucas. A master curve analysis of F82H using statistical and constraint loss size adjustments of small specimen data. *Journal of Nuclear Materials*, 329 - 333:1243 – 1247, 2004. 62
- G R Odette, T Yamamoto, and D Klingensmith. On the effect of dose rate on irradiation hardening of RPV steels. *Philosophical Magazine*, 85(4 - 7):779 – 797, 2005. 39
- T Okita and W G Wolfer. A critical test of the classical rate theory for void swelling. *Journal of Nuclear Materials*, 327:130 – 139, 2004. 91
- C Pokor, Y Brechet, P Dubuisson, J P Massoud, and A Barbu. Irradiation damage in 304 and 316 stainless steels: experimental investigation and modeling. Part I: Evolution of the microstructure. *Journal of Nuclear Materials*, 326:19– 29, 2004. 38

REFERENCES

- B Riccardi, L Giancarli, A Hasegawa, Y Katoh, A Kohyama, R H Jones, and L L Snead. Issues and advances in SiC_f/SiC composites development for fusion reactors. *Journal of Nuclear Materials*, 329 - 333:56 – 65, 2004. 14
- M Rieth, B Dafferner, and H D Röhrig. Embrittlement behaviour of different international low activation alloys after neutron irradiation. *Journal of Nuclear Materials*, 258 - 263:1147 – 1152, 1998. 63
- R O Ritchie, J F Knott, and J R Rice. On the relationship between critical tensile stress and fracture toughness in mild steel. *Journal of the Mechanics and Physics of Solids*, 21(6):395 – 410, 1973. 62
- K C Russell. Thermodynamics of gas-containing voids in metals. *Acta Metallurgica*, 20:899 – 907, 1972. 91
- K C Russell. The theory of void nucleation in metals. *Acta Metallurgica*, 26:1615 – 1630, 1978. 91, 97
- K C Russell. Theory of nucleation with cluster loss and injection: application to plastic deformation and irradiation. *Metallurgical and Materials Transactions A*, 27A:1441 – 1448, 1996. 91
- J W Sammon. A nonlinear mapping for data structure analysis. *IEEE Transactions on Computers*, C-18(5):401 – 409, 1969. 26
- R O Scattergood and D J Bacon. The strengthening effect of voids. *Acta Metallurgica*, 30:1665 – 1677, 1982. 35
- L Schäfer. Tensile and impact behavior of the reduced-activation steels OPTIFER and F82H mod. *Journal of Nuclear Materials*, 283 - 287:707 – 710, 2000. 112
- H Schroeder, W Kesternich, and H Ullmaier. Helium effects on the creep and fatigue resistance of austenitic stainless steels at high temperatures. *Nuclear Engineering and Design/Fusion*, 2:65 – 95, 1985. 103
- D N Seidman, M I Current, D Pramanik, and C Y Wei. Direct observation of the primary state of radiation damage of ion-irradiated tungsten and platinum. *Nuclear instruments and methods*, 182 - 183:477 – 481, 1981. 9

REFERENCES

- A A Semenov and C H Woo. Applicability of the conventional master equation for the description of microstructure evolution under cascade-producing irradiation. *Applied Physics A*, 69(4):445 – 451, 1999. 36
- A A Semenov and C H Woo. Classical nucleation theory of microstructure development under cascade-damage irradiation. *Journal of Nuclear Materials*, 323(2 - 3): 192 – 204, 2003. 36, 99
- D D Shen, S H Song, Z X Yuan, and L Q Weng. Effect of solute grain boundary segregation and hardness on the ductile-to-brittle transition for a Cr-Mo low-alloy. *Materials Science and Engineering A*, 394(1 - 2):53 – 59, 2005. 78, 105
- K Shiba, M Enoeda, and S Jitsukawa. Reduced activation martensitic steels as a structural material for ITER test blanket. *Journal of Nuclear Materials*, 329 - 333:243 – 247, 2004. 12
- D L Smith, R F Mattas, and M C Billone. Fusion reactor materials. In B R T Frost, editor, *Materials science and technology, a comprehensive treatment, Volume 10B, Nuclear materials part II*, volume 10B, pages 243 – 340. Wiley-VCH, 1994. 5, 7
- P Spätig, E N Campitelli, R Bonadé, and N Baluc. Assessment of plastic flow and fracture properties with small specimen test techniques for IFMIF-designed specimens. *Nuclear Fusion*, 45:635 – 641, 2005. 60
- R E Stoller. Modeling the influence of irradiation temperature and displacement rate on radiation-induced hardening in ferritic steels. Technical Report NUREG/CR-5859 and ORNL/TM-12073, Oak Ridge National Laboratory, July 1992. 37
- R E Stoller. Non-steady-state conditions and incascade clustering in radiation damage modeling. *Journal of Nuclear Materials*, 244:195 – 204, 1997. 101
- R E Stoller and G R Odette. Analytical solutions for helium bubble and critical radius parameters using a hard sphere equation of state. *Journal of Nuclear Materials*, 131: 118 – 125, 1985. 91, 102

REFERENCES

- R E Stoller and G R Odette. A comparison of the relative importance of helium and vacancy accumulation in void nucleation. In *13th International Symposium on Radiation-Induced Changes in Microstructure*, ASTM-STP 955, pages 358 – 370, 1987. 89
- K Sukanuma and H Kayano. Irradiation hardening of Fe-Cr alloys. *Journal of Nuclear Materials*, 118:234 – 241, 1983. 78
- M P Surh, J B Sturgeon, and W G Wolfer. Radiation swelling behavior and its dependence on temperature, dose rate, and dislocation structure evolution. *Journal of Nuclear Materials*, 336:217 – 224, 2005. 101
- G I Taylor. Plastic strain in metals. *Journal of the Institute of Metals*, 62:307 – 324, 1938. 35
- R Toschi, P Barabaschi, D Campbell, F Elio, D Maisonnier, and D Ward. How far is a fusion power reactor from an experimental reactor? *Fusion Engineering and Design*, 56 - 57:163 – 172, 2001. 4
- H Trinkaus and B N Singh. Helium accumulation in metals during irradiation – where do we stand? *Journal of Nuclear Materials*, 323:229 – 242, 2003. 91
- H Ullmaier and F Carsughi. Radiation damage problems in high power spallation neutron sources. *Nuclear Instruments and Methods in Physics Research B*, 101:406 – 421, 1995. 88
- H Ullmaier and H Trinkaus. Radiation damage in metallic structural materials. In *Physical Processes of the Interaction of Fusion Plasmas with Solids*. Academic Press, Inc., 1996. 9
- B van der Schaaf, D S Gelles, S Jitsukawa, A Kimura, R L Klueh, A Möslang, and G R Odette. Progress and critical issues of reduced activation ferritic/martensitic steel development. *Journal of Nuclear Materials*, 283 - 287:52 – 59, 2000. 12
- J A Wang and N S Rao. A new technique for the prediction of non-linear behaviour. *Journal of Nuclear Materials*, 301:193 – 202, 2002. 38

REFERENCES

- C Y Wei, M I Current, and D N Seidman. Direct observation of the primary state of damage of ion-irradiated tungsten I: Three-dimensional spatial distribution of vacancies. *Philosophical magazine A*, 44(2):459 – 491, 1981. 9, 11
- C H Woo and B N Singh. The concept of production bias and its possible role in defect accumulation under cascade damage conditions. *Physica Status Solidi B*, 159(2): 609 – 616, 1990. 90
- T Yamamoto, G R Odette, H Kishimoto, and J W Rensman. Compilation and preliminary analysis of a irradiation hardening and embrittlement database for 8Cr martensitic steels. Technical Report DOE/ER-0313/35, ORNL, 2003. 38, 43, 50, 54, 60, 61, 63
- M A Yescas-González. *Modelling the microstructure and mechanical properties of austempered ductile irons*. PhD thesis, University of Cambridge, November 2001. 30